Phase-Field Simulations of Multicomponent Lipid Membranes Coupling Composition with Deformation

by

Chloe M. Funkhouser

A dissertation submitted in partial fulfillment
of the requirements for the degree of
Doctor of Philosophy
(Biomedical Engineering)
in The University of Michigan
2011

Doctoral Committee:

Associate Professor Katsuyo S. Thornton, Co-Chair
Associate Professor Michael Mayer, Co-Chair
Professor Alan J. Hunt
Professor Ronald G. Larson

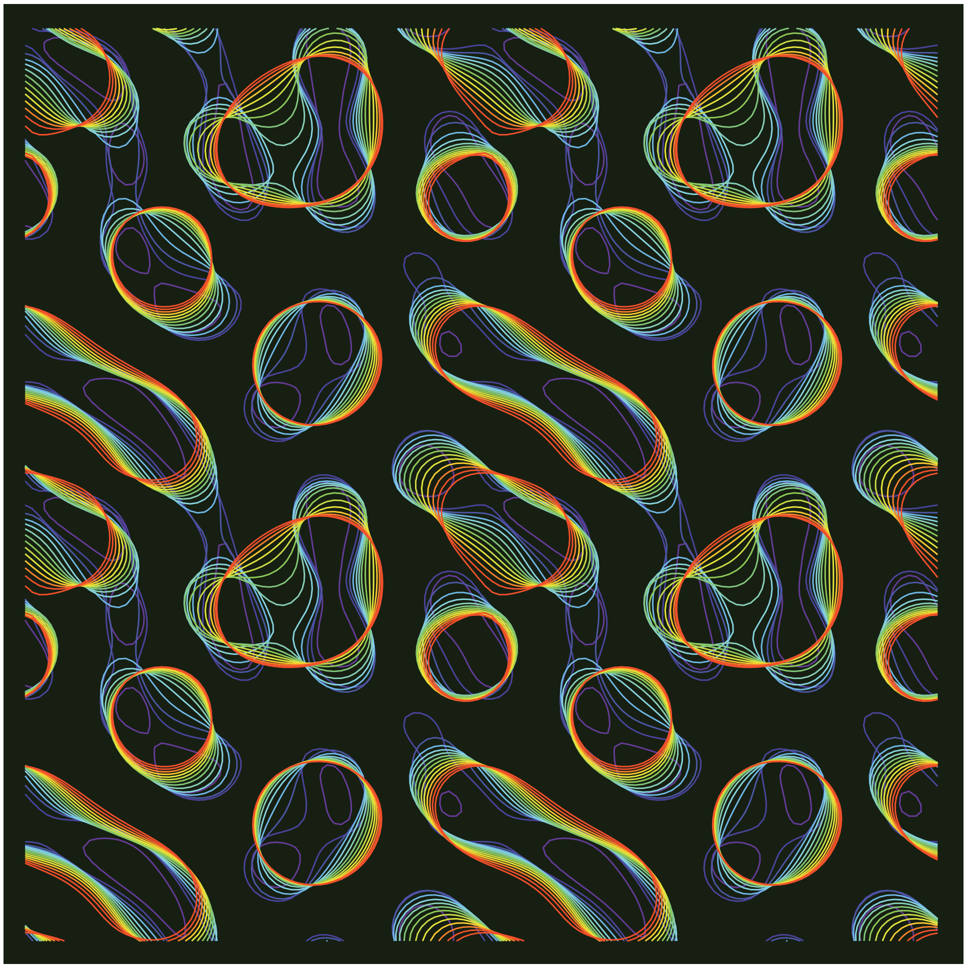

To my family,
and to the many teachers whom
I have had the pleasure of learning from
during the 22 years of my education.

ACKNOWLEDGEMENTS

I first would like to acknowledge my advisor, Prof. Katsuyo Thornton, who has been an inspiring mentor, teacher, and friend to me over the past six years that I have worked in her lab. Without her advice (and a small amount of pushing), I likely would not have even applied to graduate school. I would like to thank my co-advisor Prof. Michael Mayer for accepting me into his lab as a transient experimentalist, always being supportive, understanding, and insightful. I thank the remaining members of my committee, Profs. Ron Larson and Alan Hunt, for their guidance, encouragement, and among other things, for asking me questions to make sure I kept the bigger picture of my research in mind. I would also like to acknowledge my collaborator, Prof. Francisco Solis, who has also been a wonderful mentor and teacher for me, and I would like to thank him for his patience and great contributions to my work and education.

My interactions with lab mates in both the Thornton and Mayer Research Groups have been a huge part of my learning experience in many aspects. I would like to acknowledge the following past and present Thornton Group members: Dr. Hui-Chia Yu, Dr. Hsun-Yi Chen, Nirand Pisutha-Arnond, Victor Chan, Chal Park, Nick Patterson, Steve DeWitt, Bernardo Orvañanos, Andrea Jokisaari, Tapiwa Mushove, Dr. Larry Aagesen, Britta Lundberg, Dr. Roberto Mendoza, Dr. Dong-Hee Yeon, and Dr. Ben Torralva. Each of them have contributed to my graduate experience in their own positive way, whether it was by introducing me to LaTeX or Fortran, offering suggestions during my presentations, or just being there when I needed them. I

have been fortunate enough to feel like a part of two research groups during my graduate studies, and would also like to acknowledge the following past and present Mayer Group members: Kim Horger, Dr. Dan Estes, Dr. Sheereen Majd, Panchika Prangkio, Erik Yusko, Dr. Divya Rao, Yazan Billeh, Brandon Bruhn, Jay Johnson, Dr. Haiyan Liu, Marian Adamson, Stefan Schuhladen, Dr. Ricardo Capone, and Dr. Jeff Uram. They have always been welcoming and have continually offered a fresh perspective on my work from a point of view outside of the simulation world.

The majority of the results presented in this work were produced by simulations performed using cluster resources provided by the Center for Advanced Computing in the College of Engineering, and I would like to thank the staff there for not only making my research possible, but also for assisting me individually to improve the performance of my codes. I additionally utilized computational resources on the NSF TeraGrid, and would like to acknowledge this program as well.

I would like to acknowledge my funding sources, the NSF Graduate Research Fellowship Program and Department of Education Graduate Assistance in Areas of National Need (GAANN) Fellowship awarded through the UM Biomedical Engineering Department. Both of these fellowships have enabled me to complete this work and grow as a researcher, and the GAANN Fellowship additionally provided valuable teaching experience for me that I am appreciative of.

Finally I absolutely must acknowledge my friends and family, without whom I could have never made it to the end of this long road. I thank my parents for their unfaltering support and encouragement, and my brother Dillon for keeping me grounded through this adventure that has been graduate school.

TABLE OF CONTENTS

CHAPTER

LIST OF FIGURES

Figure

LIST OF TABLES

Table

LIST OF ABBREVIATIONS

GUV giant unilamellar vesicle

DRM detergent resistant membrane

SM sphingomyelin

PC phosphatidylcholine

DOPC dioleoylphosphatidylcholine

DPPC dipalmitoylphosphatidylcholine

Chol cholesterol

AFM atomic force microscopy

FCS fluorescence correlation spectroscopy

PS phosphatidylserine

PE phosphatidylethanolamine

MGDG monogalactosyldiacylglycerol

DGDG digalactosyldiacylglycerol

GM1 ganglioside

LPC lysophosphatidylcholine

DNPC dinervonoylphosphatidylcholine

DPhPC diphytanoylphosphatidylcholine

DOG dioleoylglycerol

L_d liquid-disordered

L_o liquid-ordered

MD molecular dynamics

CG coarse-grained (model)

MC Monte Carlo method

KMC kinetic Monte Carlo method

SPAM smooth particle applied mechanics

GPMV giant plasma membrane vesicle

TNT tunneling nanotube

SOPC stearoyloleoylphosphatidylcholine

ABSTRACT

Phase-Field Simulations of Multicomponent Lipid Membranes Coupling Composition with Deformation

by

Chloe M. Funkhouser

Co-Chairs: Katsuyo S. Thornton and Michael Mayer

In this work, we have developed a model and simulation method to study the thermodynamics and kinetics of phase-separating multicomponent lipid bilayer membranes. A continuum-level phase-field method is applied to model the phase separation, and a Helfrich free energy is used to couple the composition with the mechanical properties of the two separated phases, accounting for their bending rigidities and spontaneous curvatures. Four specific models are presented: a planar background model for nearly planar portions of membranes, a spherical background model for vesicles, a cylindrical background model for tubules, and an extension of the planar background model that additionally accounts for interactions between the two leaflets of the bilayer.

The planar background model is used to investigate what types of initial compositional and geometric configurations lead to a stripe phase morphology. We observe that, while patterned rigid supports are able to reliably induce such a morphology, perturbations in composition produce stripes less reliably. With the vesicle model, we investigate the effects of initial vesicle shapes, phase fractions, spontaneous curvatures, and bending rigidities on vesicle dynamics. We find that (i) a phase with spontaneous curvature closer to the vesicle surface curvature is favored to form continuous domain morphologies, even when present at or slightly less than 50%; and (ii) mixtures with small amounts of a phase with extreme spontaneous curvature, as well as vesicles with elongated shapes, can have enhanced stability in configurations with multiple minority phase domains as a result of the bending energy. The tubule model is applied to investigate whether bending energy can stabilize the pearling instability observed experimentally. We find that appropriate spontaneous curvature and bending rigidity can indeed stabilize the tubule. Lastly, we use the planar bilayer model to investigate the effects of the interleaflet coupling strength, finding that strong coupling can cause phase compositions to shift, such that the effective phase fraction becomes closer to 50% and the stripe morphology is more favored. Overall, we find that composition and shape are closely related, where compositional morphologies can alter the membrane shape and vice versa.

CHAPTER I

Introduction

1.1 Membrane Composition, Structure, and Function

Biological membranes are ubiquitous structures at the cellular level of life. While they can be composed of lipids, proteins, and carbohydrate residues, the common component in many different forms of cellular membranes is the lipid. The most common membrane lipid molecules are glycerophospholipids, which typically have one or two hydrocarbon chains (lipid "tailgroups," or acyl chains) with an even number of carbon atoms ranging between 14 and 24 atoms. These tailgroups are attached via a glycerol group to a polar phosphate-containing group (lipid "headgroup"). The structures of some common lipids are presented in Fig. 1.1.

A lipid bilayer is the most common structure formed by *in vivo* membranes, composed of two opposing leaflets, defined as oriented planes of approximately aligned lipids. A schematic of a lipid bilayer is presented in Fig. 1.2. In a lipid bilayer, the lipids orient themselves such that the polar headgroups interface the aqueous environment of the intra or extracellular space while the nonpolar tailgroups in the leaflets face each other to avoid interacting with the surrounding water. The thermodynamic driving force for the formation of a lipid bilayer is the hydrophobic force, which can be explained with the following entropic argument.

Following Ref. 1, consider two configurational scenarios: one where a handful of

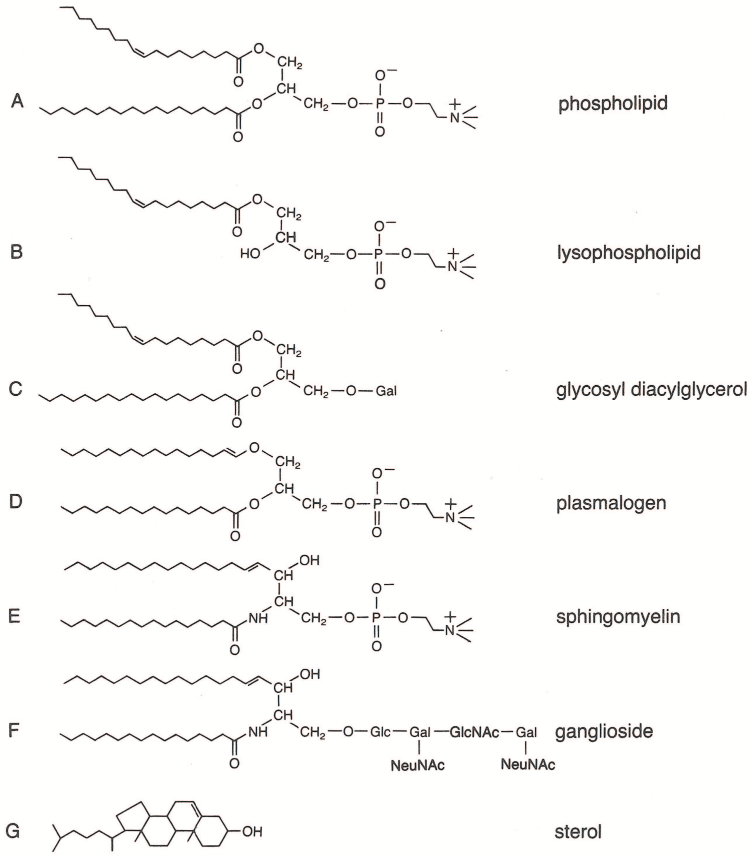

Figure 1.1: Chemical structures of lipids commonly found in mammalian membranes. Reproduced from Ref. 1.

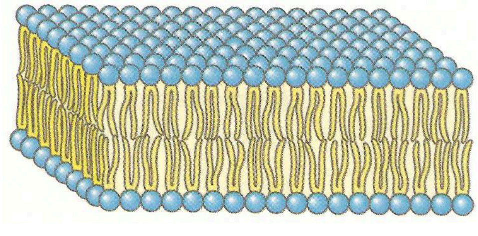

Figure 1.2: A schematic of a lipid bilayer membrane, composed of lipids with polar headgroups (blue) and nonpolar tailgroups (yellow). Reproduced from Ref. 2.

lipid molecules are individually surrounded by water, and a second where the lipid molecules form a cluster so that no water separates them. In the first scenario, a "cage" of water molecules encases each lipid, including the tailgroups. Each water molecule has a particular orientation to maximize its hydrogen bonds with neighboring water molecules, but the water molecules in contact with the lipid tailgroups have configurational constraints imposed upon them since they have fewer neighboring water molecules than those in the bulk. This constraint imparts an ordering in the water molecules forming the cages around each lipid, decreasing entropy. In the second scenario, the clustered lipids together have a single water cage, and overall the amount of ordering imposed on the water molecules in this single large cage is less than that of the combined ordering that would occur with the individual water cages, each containing an individual molecule, as described in the first scenario. This second scenario therefore has higher entropy (*i.e.*, less order) than the first, making it more energetically favorable. While the polar headgroups also impose some ordering of the water molecules in their cage, the favorable electrostatic interactions between the polar water and polar headgroups compensates for the decrease in entropy. Therefore, as a result of this hydrophobic force, the nonpolar tailgroups preferentially associate with other nonpolar tailgroups rather than water, and the polar headgroups are turned outward to interface with the water (1).

Since the lipid molecules in a bilayer membrane associate with each other only via hydrophobic interactions, which are relatively weak compared with chemical bonds, the lipids are free to move about laterally within the leaflet they reside in. The lipids have so much freedom to move about within the plane of the membrane that, at physiological temperatures, the membrane is considered to be in a liquid state. Thus, membranes constitute an intriguing system from a materials science perspective, where they are essentially a two-dimensional surface consisting of components with liquid-like mobility within that surface.

So far the discussion of biological membranes has focused on lipids, however, proteins are commonly incorporated into the lipid bilayer structure also. The classic model of a biological membrane is the Singer-Nicholson fluid mosaic model, where proteins “float” in a “sea” of lipids (3), as illustrated in Fig. 1.3. Membrane proteins are classified as either peripheral or integral, meaning they either associate with only the hydrophilic surface of the membrane (peripheral) or penetrate into the hydrophobic core of the membrane (integral). Many integral proteins are transmembrane, meaning they span the entire thickness of the membrane, often several times (*i.e.*, they have more than one membrane-spanning domain) (2). The degree to which a protein is incorporated into the membrane depends on how hydrophobic or hydrophilic the outer-facing segments of the protein are. For example, for a protein to have an integral configuration, it must have hydrophobic segments in the portion that contacts the tailgroups of the lipids in the bilayer; if it does not have exposed hydrophobic segments, it will more likely be a peripheral protein. Some peripheral proteins have a lipid anchor which incorporates into the lipid bilayer. Lastly, carbohydrate residues can be associated with membranes by their attachment to either a lipid (*e.g.*, a glycolipid) or a membrane protein (*e.g.*, the oligosaccharide chains of a glycoprotein). These carbohydrate residues would typically be found on the extracellular face of the plasma membrane of a mammalian cell.

Membranes are found in a variety of contexts in cells. A lipid bilayer membrane known as the plasma membrane surrounds cells to form a barrier between intracellular (cytoplasmic) and extracellular space, isolating the cellular components and serving as a gate for material entering and leaving the cell. Membrane proteins perform a large variety of tasks, and the plasma membrane serves as a structural platform for them, in addition to actively sorting and directing their behavior. The interactions between membrane lipids and proteins will be discussed further in Sec. 1.2. The plasma membrane also links to the cytoskeleton, which is a mesh of fibers that sup-

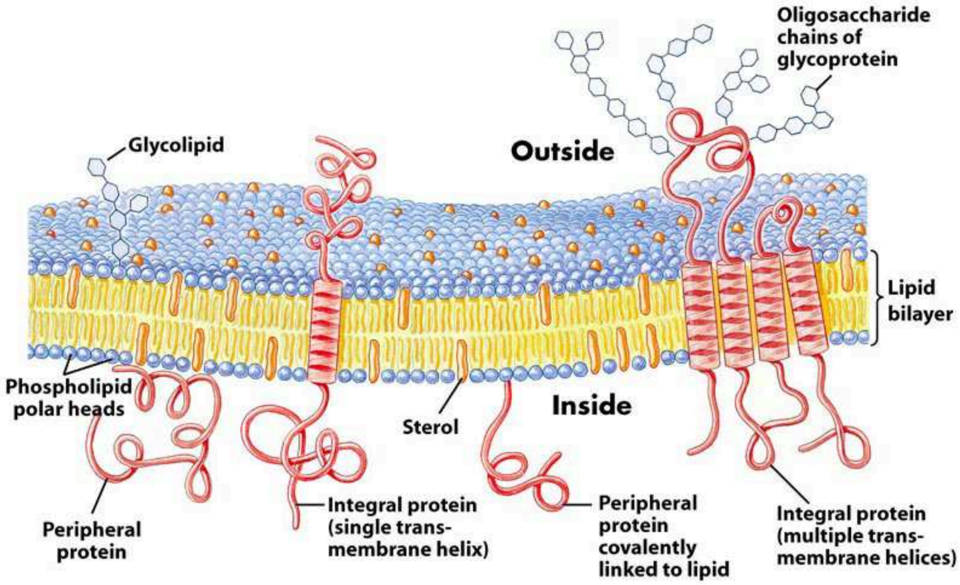

Figure 1.3: Fluid mosaic model representation of a cell plasma membrane, consisting of a lipid bilayer with proteins and carbohydrate moieties. Reproduced from Ref. 2.

ports the cell mechanically. In addition to the plasma membrane, some organelles have lipid membranes encasing them, including mitochondria and chloroplasts, the nucleus, the endoplasmic reticulum, Golgi apparatus, lysosomes, and peroxisomes (1). Additionally, transport vesicles are simple lipid bilayer capsules typically containing water, allowing them to bud off from or fuse with the plasma membrane to allow material to enter or leave the cell.

1.2 Membrane Heterogeneity

Several different varieties of lipid molecules are commonly found in membranes, varying by the cell type, although a single cell will have multiple kinds of lipids in all of its various membranes. These lipid mixtures forming the membranes are not necessarily homogeneous mixtures, and there is much experimental evidence that membrane lipids are distributed heterogeneously (4–8). This heterogeneity manifests as patches termed lipid rafts, defined as membrane structures of 10-200 nm in size, highly dynamic, and enriched in sphingolipids and sterols (9). Sphingolipids, as opposed to the majority of other membrane lipids, have long, largely saturated acyl chains, causing them to pack together differently than other lipids. Cholesterol, with a small polar group and a rigid ringed structure, fits into the voids between sphingolipids to function as a spacer. This molecular packing of sphingolipids and cholesterol, differing from how lipids with polyunsaturated acyl chains pack, is the basis for phase separation into raft and non-raft phases (10, 11). The presence of cholesterol in lipid membranes is known to broaden the thermal phase transition from the (solid) gel phase observed at low temperature to the liquid-disordered phase (L_d) observed at higher temperatures, introducing an intermediate phase, the liquid-ordered phase (L_o). The L_o phase has a molecular order characterized by tightly packed acyl chains similar to the (solid) gel phase, but lateral mobility similar to the L_d phase (12–15). It is this L_o phase that rafts exist in. Schematics of these three phases are shown in Fig. 1.4 to illustrate the difference in the packing and ordering.

A variety of experimental methods have been used to study lipid rafts. In many mammalian cells, it has been found that certain portions of membrane are insoluble in detergents such as Triton X-100 when used at 4°C. The fragments of detergent-resistant membrane (DRM) have been found to be rich in sphingolipids and cholesterol compared with the rest of the membrane, making the connection between DRMs and lipid rafts (17, 18). When DRMs are isolated from cells, they contain lipid-anchored proteins and integral proteins, which would indicate that those proteins preferentially associate with lipid rafts (10, 14, 19). In addition to using detergents to study lipid rafts and associated proteins, techniques that deplete membranes of cholesterol can be used to show that protein function is altered in the absence of cholesterol, indicating the protein function is raft-related (20–22). Single-molecule techniques have been employed to study raft dynamics in living cells, finding that molecules thought to be associated with lipid rafts including saturated lipids, sphingolipids, and GPI-anchored

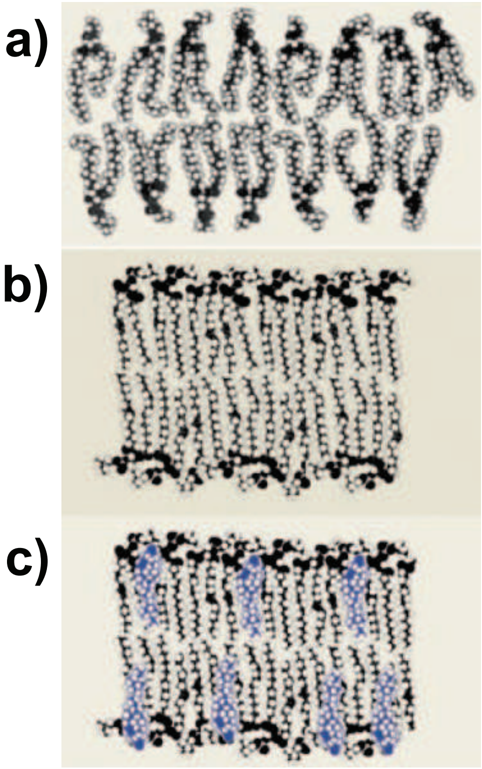

Figure 1.4: Schematics illustrating the molecular order of three lipid bilayer phases: (a) the liquid-disordered (L_d) phase, (b) the solid gel phase, and (c) the liquid-ordered (L_o) phase. The diffusion coefficients in the L_d and L_o phases are larger than in the gel phase, and the ordering of the acyl chains in the L_o and gel phases is higher than in the L_d phase. Reproduced from Ref. 16.

proteins, are transiently confined to raft-sized regions of the membrane (4, 23–27).

It has been shown that lipid rafts are involved in various cellular processes carried out by proteins associating with lipid rafts. The rafts can help to concentrate certain proteins spatially, or in some cases the lipids could directly alter protein function by affecting conformation (14). Rafts have been found to modulate protein-protein interactions in resting and activated immune cells, including T-cells, B-cells, and mast cells (11, 28–30). Other examples of raft-associated proteins are caveolin, a protein involved in caveolar endocytosis (31–33), integrin proteins and receptors (34–36), and the integral membrane protein LAT involved in signaling (37). Rafts have also been implicated in bacterial and viral invasion (38, 39).

1.2.1 Model Membrane Systems

The plasma membrane of mammalian cells can be composed of hundreds of lipid species in some cases, and therefore it can be desirable to study lipid phase dynamics in simpler membrane systems such as planar lipid bilayers and vesicles (similar to those used for transport in cells). Additionally, since lipid rafts are thought to be on the order of tens of nanometers in size, and are also highly dynamic, they have proven difficult to observe in intact cells. Planar bilayers and vesicles composed of ternary lipid mixtures (typically an unsaturated lipid, a sphingolipid, and cholesterol at physiologically relevant levels) have been studied by a number of groups to elucidate lipid phase behavior (6, 40–42) since these types of mixtures can separate into micron-scale L_d and L_o (raft-like) phases, analogous to membrane non-raft and raft domains. In these simple membranes, the phase-separated domains are on the order of tens of microns in size and therefore they can be observed using fluorescence microscopy, where a small amount of a fluorescent molecule that is known to partition into one of the phases is added (see Figs. 1.5 and 1.6). Other techniques have also demonstrated phase separation in ternary model membranes, including Atomic Force

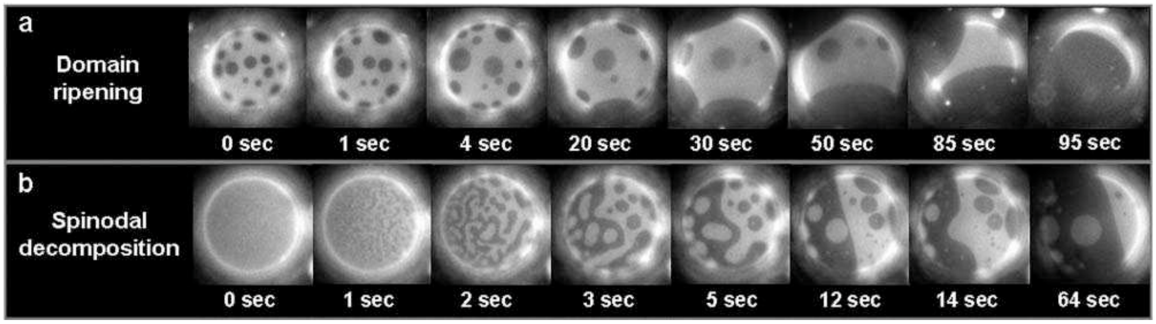

Figure 1.5: Fluorescence micrographs of ternary giant unilamellar vesicles (GUVs) approximately 30 microns in diameter imaged over time near the miscibility transition temperature. The L_o phase appears dark and the L_d phase appears bright. The GUV in (a) is a 1:1 mixture of dioleoylphosphatidylcholine (DOPC) and dipalmitoylphosphatidylcholine (DPPC), plus 25% cholesterol, and evolves from a configuration with many small L_o domains to a completely phase-separated state in order to decrease its line-tension energy. The GUV in (b) is a 1:1 mixture of DOPC and DPPC, plus 35% cholesterol, and separates into striped domains in a process resembling spinodal decomposition early in the evolution, eventually forming large round domains to reduce line-tension energy as in part (a). The system in (b) has approximately an equal mixture of the two phases. Reproduced from Ref. 5.

Microscopy (AFM) (43) and Fluorescence Correlation Spectroscopy (FCS) (44, 45). AFM has the benefit that it does not use light to probe the membrane surface, and can therefore access structures on the nanometer length scale (46). AFM studies have shown membrane regions with different heights but smooth edges indicating the presence of phase-separated L_o and L_d domains rather than solid gel domains, which would not form smooth edges (47). FCS is a tool that can be used to measure diffusion coefficients, and has been able to demonstrate that the separated phases in ternary vesicles have distinctly different diffusion coefficients, even though both are liquid phases (48–51). Specifically, the L_o phase has been found to have a diffusion coefficient approximately an order of magnitude larger than the solid gel phase but also an order of magnitude lower than in the L_d phase (48).

While these simple membrane systems do reproduce the essential lipid phase be-

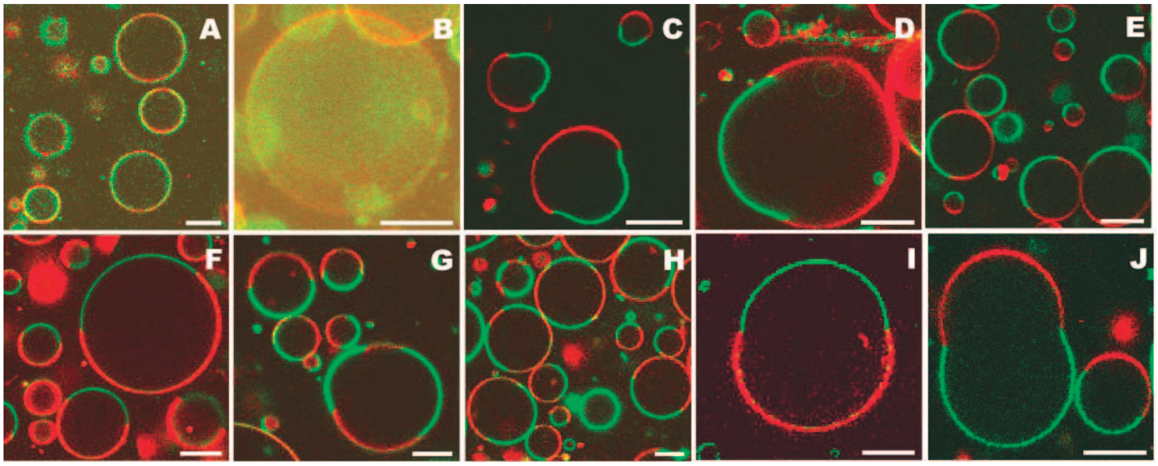

Figure 1.6: Confocal fluorescence micrographs of ternary GUVs composed of mixtures of sphingomyelin, cholesterol, and a phosphatidylcholine (PC) lipid where the acyl chain (tailgroup) length was varied. The red dye partitions into the L_d phase while the green dye partitions into the L_o phase. All images are sections of the GUVs, except (b), which is a three-dimensional projection; scale bars represent 10 microns. The GUVs in (a) and (b) have the longest-chain PC and do not exhibit phase separation since both dyes appear to be distributed uniformly throughout the membrane. The next longest acyl-chain PC was used for the system in (c) and (d), where negative curvatures appear at the interfaces, and a small budding vesicle appears in (d). The next longest acyl-chain PC was used for (e) and (f), and very little deviation from a spherical shape is observed, and finally, with the shortest acyl-chain PC in (g-j), the interfaces appear to have a positive curvature with budding structures. These illustrate that differences in thickness between the two phases (a function of acyl chain length) can induce discontinuous curvature at phase interfaces. Figure copied and modified from Ref. 52.

havior, they neglect the effects of membrane proteins and the underlying cytoskeleton. Both proteins and the cytoskeleton have been hypothesized to play a role in lipid raft dynamics, potentially acting to limit the size that lipid rafts can achieve (24, 53–55). This may account for the discrepancy between the nanometer-scale lipid rafts found in cells and the micron-scale lipid raft-like domains observed in model membrane systems.

In addition to planar bilayers and vesicles being simple membrane models of the cell plasma membrane, they also have great potential for application in biotechnology and biomedical engineering. Planar lipid bilayers have potential to be used as biosensors, where they could be engineered such that demixing and particular phase morphologies would be induced by the presence of an analyte of interest. Vesicles can be used as drug delivery vehicles (56–59), where perhaps lipid phase behavior could be tuned in order to target particular cell types for more specific therapy. Additionally, vesicles have potential for use as microreactors and as biomimetic surfaces for studying signaling cascades and chemical reactions (60–62).

1.3 Membrane Morphology

The different geometries of various lipids can have an effect on the morphology and mechanical properties of the membrane (1, 52, 63, 64). The degree of saturation of the acyl chain tailgroups influences the amount of space they fill since each double bond creates a kink in the tail. The shape of the overall lipid molecule is a function of the cross-sectional area (in the plane of the membrane) occupied by the headgroup compared with that of the tailgroups. When they occupy roughly the same amount of area, the lipid is cylindrical, but if one is larger than the other, the lipid has the shape of a cone or inverted cone. As illustrated schematically in Fig. 1.7, lipids with two saturated tailgroups and an average-sized headgroup tend to be cylindrical; lipids with two unsaturated tailgroups and a small headgroup tend to have a cone shape;

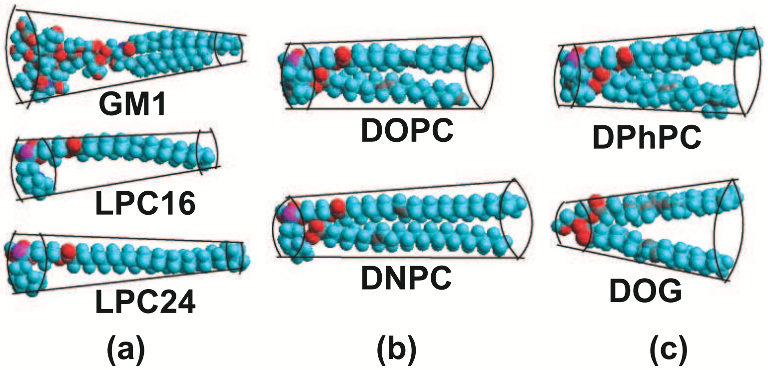

Figure 1.7: Space-filling atomistic models of various lipids illustrating their overall shapes, drawn in as truncated cones. (a) Cone-shaped lipids, (b) cylindrical lipids, and (c) inverted-cone-shaped lipids. Color key: hydrogen, blue; oxygen, red; phosphate, purple; and carbon, gray. Abbreviations are ganglioside (GM1), lysophosphatidylcholine (LPC), dioleoylphosphatidylcholine (DOPC), dinervonoylphosphatidylcholine (DNPC), diphytanoylphosphatidylcholine (DPhPC), and dioleoylglycerol (DOG). Figure copied and modified from Ref. 64.

lipids with a single tailgroup and/or large headgroup tend to have an inverted-cone shape (63).

An asymmetric bilayer is defined as a lipid bilayer where the two leaflets are composed of different lipids. Natural biological membranes are asymmetric; for example, in the plasma membrane of mammalian cells, the inner leaflet tends to be rich in phosphatidylserine (PS) and phosphatidylethanolamine (PE), while the outer leaflet tends to be rich in phosphatidylcholine (PC) and sphingomyelin (SM) (2, 65, 66). Spontaneous curvature is a characteristic of membranes where the molecular shapes of the membrane components give the membrane a tendency to adopt a particular curved morphology. For example, a single-component lipid monolayer with a lipid headgroup that occupies a different cross-sectional area than the tailgroup would have a nonzero spontaneous curvature. For a single-component (and therefore symmetric) lipid bilayer, the dimensions of the lipids in the two opposing leaflets are all the same, and the membrane would therefore have zero spontaneous curvature. However, for an

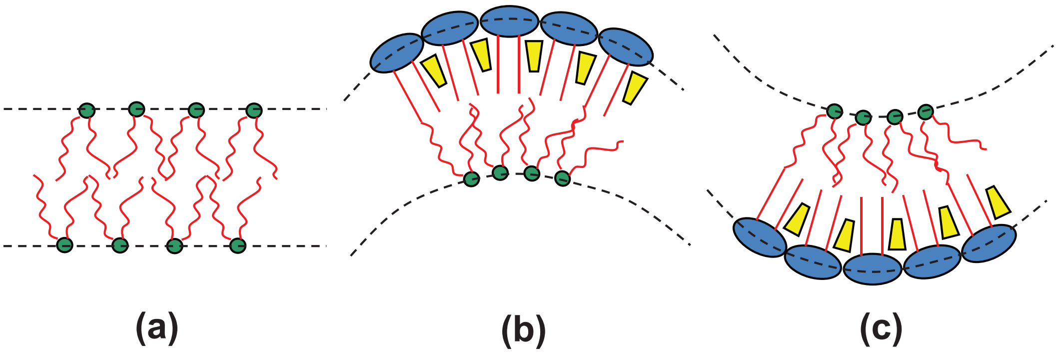

Figure 1.8: Schematics of symmetric (a) and asymmetric membranes (b,c) and their spontaneous or preferred curvatures. Positive (b) or negative (c) curvatures can arise depending on which leaflets the different lipids reside in. In these examples, the lipid shown with a green headgroup has an overall inverted-cone shape with a small headgroup and two unsaturated tailgroups, while the lipid shown with the blue headgroup has an overall cone shape, with a large headgroup and saturated tailgroups. Cholesterol is also shown in yellow, partitioning with the saturated lipid, as it tends to do so in the L_o phase.

asymmetric bilayer, nonzero spontaneous curvature can arise if the dimensions of the lipids in the two leaflets differ. Schematics of such configurations are illustrated in Fig. 1.8. The phenomenon of spontaneous curvature is one way that the composition of a lipid bilayer can alter the morphology of the membrane, by making a nonzero curvature energetically favorable. Additionally, since the coexisting L_o and L_d phases have different molecular packing, they can have different resistance to bending away from this spontanoeous curvature, termed bending rigidity.

One example from nature where curved bilayer membranes with an asymmetric composition are observed is in the thylakoid membrane of chloroplasts. The thylakoid membrane has both zero curvature regions and regions with very high curvature of approximately 10 nm^{-1} (67, 68). There is lateral and transverse heterogeneity in the thylakoid membrane, which are both present for reasons related to protein function and also to help maintain the membrane structure. The two main lipids that together compose 75% of the membrane are monogalactosyldiacylglycerol (MGDG)

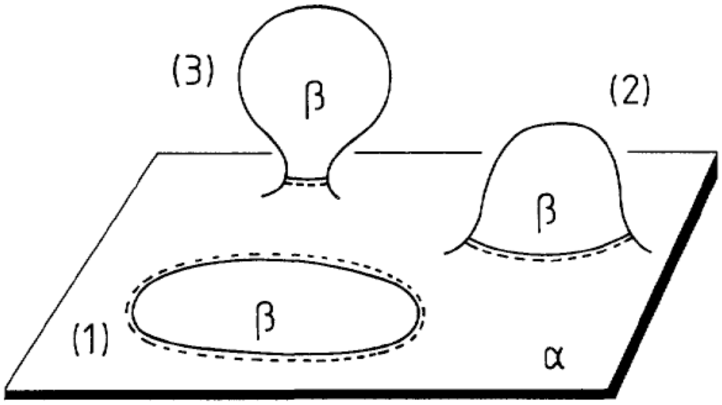

Figure 1.9: Schematic showing the budding of a membrane domain driven by line-tension energy. The interface between the β domains and the α matrix is shown with the double solid-dashed line, and is of higher energy than the bulk. Progressing from (1) to (3), the length of this interface is greatly reduced as the β domain bulges out (2) and finally forms a bud (3), reducing the line-tension energy. Reproduced from Ref. 69.

and digalactosyldiacylglycerol (DGDG). MGDG is cone-shaped, where the tailgroups occupy more cross-sectional area than the headgroup. DGDG has a large headgroup and has the shape of an inverted cone. Therefore, it makes sense that to form the highly-curved regions of the thylakoid membrane, the MGDG is enriched in the concave inner leaflet while DGDG is enriched in the convex outer leaflet (67, 68).

Another way that the composition of a lipid membrane can affect its morphology is related to line-tension energy. In a membrane with coexisting L_o and L_d phases, the interfacial regions where the immiscible phases meet have higher energy than the pure, bulk-phase regions. Therefore, there is a driving force to reduce the total amount (or length) of interface. One way that this can be accomplished is if one phase bulges away from the plane of the membrane, such that the length of interface shortens, as illustrated in Fig. 1.9. Therefore, even a symmetric bilayer that has phase separated can experience composition-driven deformation, as observed in some of the systems in Fig. 1.6.

In this section so far, examples of how composition can affect the curvature of the membrane have been discussed. However, the interplay between composition and morphology appears to be two-way, where altering the membrane morphology can affect the distribution of the membrane components. Deforming a membrane can cause compositional phases to redistribute, occupying portions of the membrane that best satisfy their bending preferences. One example is shown in Fig. 1.10, where an osmotically deflated vesicle (with excess surface area for its volume) shows the L_o and L_d phases sorting themselves to low- and high-curvature regions, respectively (8). The L_o phase, shown in blue, is more rigid and/or prefers to have a lower curvature compared with the L_d phases shown in red, and therefore occupies the lower-curvature regions of the membrane, even though the presence of these numerous domains is unfavorable in terms of the line-tension energy. Another experiment illustrating phase sorting with respect to membrane curvature utilized the micropipette aspiration technique to draw a thin membrane tubule from a phase-separated vesicle, containing two fluorescent dyes known to partition into each of the phases (70). When the tubule was drawn to a diameter of 70 ± 10 nm, the dyes were detected at equal levels throughout the tubule, but when the tubule was pulled further down to a diameter of 20 ± 2 nm, the dye that partitioned into the L_d phase was detected at approximately twice the concentration of the dye in the L_o phase, indicating that altering the membrane curvature caused the membrane components to redistribute. Lastly, sorting of phase-separated lipid domains in planar bilayers supported on a patterned surface with regions of high and low curvature was observed in Ref. 71.

As a common theme in biological systems including membranes, form and function are closely related. Also, the local lipid environment can chemically affect how the membrane interacts with proteins. Therefore, membrane composition, morphology, and function are all intertwined. For example, in Ref. 72 it is reported that the interaction of the HIV-1 Nef protein with membranes is sensitive to both membrane composition (specifically, lipid charge) and membrane curvature, where the associa-

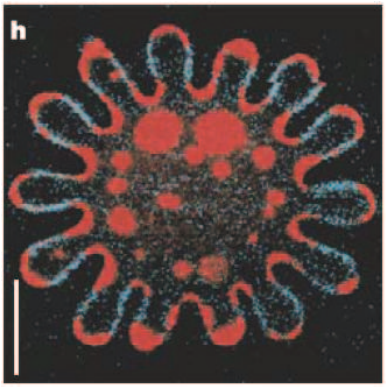

Figure 1.10: A confocal fluorescence micrograph of an osmotically deflated GUV composed of a mixture of DOPC, SM, and cholesterol. The red dye partitions into the L_d phase while the blue dye partitions into the L_o phase. The pattern of where the different phases appear suggests that the L_o phase is preferentially occupying lower-curvature regions, so much so that it has split into numerous isolated domains (increasing the line-tension energy compared with a coarser configuration) to satisfy its bending energy. The scale bar represents 5 microns. Reproduced from Ref. 8.

tion constant of Nef with liposomes varied with liposome size. This Nef protein is essential for HIV-1 replication and the progression of the disease to AIDS. A general example of how membrane composition can affect membrane function comes from the concept of hydrophobic mismatch, where the thickness of the hydrophobic region of a bilayer (a function mainly of the length of the lipid tailgroups, but also of molecular packing interactions) determines the available locations for insertion as well as the orientation of integral proteins, matching the hydrophobic regions of the protein with those of the bilayer (73, 74). Other examples include the high-curvature membrane regions required for vesicle budding (75, 76), and the curvature-sensing properties of some protein motifs including BAR domains (77, 78), amphipathic helices (79, 80), and membrane-anchored proteins (80, 81). This curvature-sensing can translate to proteins being concentrated in areas of particular curvature, binding only to areas of particular curvature, or being more active in areas of particular curvature, as a result of physicochemical properties of curved membranes, as reviewed in Refs. 82 and 83.

1.4 Membrane Interleaflet Interactions

There is theoretical and experimental evidence that the phase behavior of one leaflet can influence the behavior of the opposing leaflet (84–86). In asymmetric planar lipid bilayer membranes composed of simple mixtures to mimic the inner and outer leaflets of a cell plasma membrane, it has been found that phase separation can be induced in the inner leaflet (or can be suppressed in the outer leaflet), depending on the strength of the tendencies of the leaflets to phase separate (or to remain homogeneous) (87). It has also been observed that in model membranes where both leaflets phase separate, the domains in the two leaflets interact and tend to align laterally (65, 88). New phases can also arise from the interleaflet interactions, where intermediate phases form near phase boundaries when domains in opposing leaflets cannot perfectly align because they are present in different fractions (87).

As an example of a process in living cells where there is evidence that interleaflet coupling plays an important role, it has been observed that peripheral proteins (interacting with only one leaflet of the membrane) can "sense" the presence of peripheral proteins interacting with the opposite leaflet to trigger signaling cascades. In some cases, transmembrane proteins assist in this "sensing" by interacting with both peripheral proteins, but in other cases the "sensing" is thought to occur via the membrane lipids alone (89–93). In the latter case, it is hypothesized that specific lipids in the outer leaflet first cluster around a peripheral protein, inducing lipids to cluster at the same location in the inner leaflet, which then in turn attracts the second peripheral protein to the inner leaflet (92).

Mechanisms to explain this transmembrane lipid coupling have been proposed, although the dominant effect has not been fully determined. The possible mechanisms include interdigitation of the tailgroups of the lipids in the opposing leaflets (94), the exchange of cholesterol across the bilayer, and molecule-molecule interactions similar to what liquid-disordered and liquid-ordered phases in a single leaflet experience at their interface (95, 96). Spontaneous flip-flop of lipids from one leaflet to the other can occur, but typically on time scales much longer than the coupling observed in experiments due to the energetic penalty of bringing a hydrophilic lipid headgroup through the hydrophobic tail region of the bilayer.

1.5 Overview and Outline of Dissertation

Because of the rich connections between membrane composition, morphology, and ultimately, function, the investigations in this work focus on the morphological aspects of phase separation in lipid membranes.

The overall aim of this work was to develop an understanding of the thermodynamics and kinetics involved in phase-separating lipid membrane systems, investigating the interplay between membrane composition and morphology, in particular. In this work, we have developed a continuum-level method for modeling phase separation in multicomponent lipid membranes, where the composition is coupled to mechanical properties of the phases. Since different lipids have different shapes, and mixtures of lipids have different packing structures, the membrane composition is related to the preferred morphology of the membrane. This means that as the composition evolves from, for example, a random mixture to a macroscopically phase-separated configuration, the membrane can deform in response. Also, since the phases have preferred curvature, particular membrane morphologies can influence the locations and sizes of the compositional domains.

In Chapter II, an outline of the main numerical methods used in this work is presented. The chapter begins with a literature review of recent work using computational modeling to investigate aspects of lipid membranes relevant to this work. This is followed by an introduction to the phase-field model, a version of which is used here to model the compositional evolution. Finally, the finite difference method is presented, which is a scheme for numerical derivative calculations and numerical integrations via discretization.

Chapter III presents the first iteration of the model we have developed to simulate compositional phase separation and the corresponding morphological evolution, in this case for a nearly planar portion of a membrane. The model detailed in this chapter was later modified to include additional aspects of the governing physics or applied to membranes with different geometries. Therefore, the later chapters will build on the model from this chapter, detailing only the modifications made. Results produced with this nearly planar membrane model are presented, examining the formation of stripe phase morphologies employing different initializations and constraints.

Chapter IV describes the modification of the planar model from the previous chapter to apply it to a spherical background geometry, in order to model lipid vesicles. This model represents the membrane as a closed surface, including an internal pressure to represent the fluid within the vesicle interior. A special meshing system, known as the Yin-Yang grid system, is employed for this spherical background geometry model, and its advantages as well as the implications for its implementation are described. Results are presented examining different parameter sets, investigating how the stationary states and dynamics are affected by factors such as the spontaneous curvatures of the two phases in relation to the inverse of the size of the vesicle, the fraction of the two phases, and the bending rigidities of the phases. Vesicles initialized with ellipsoidal shapes are also studied.

Chapter V presents an alternative modification to the planar model, applying it to a cylindrical background geometry in order to study lipid membrane tubules. Much of this model is similar to the spherical model, although no special meshing scheme is employed. The model is used to examine the morphologies formed in cylindrical systems where the phases have mismatched spontaneous curvatures, producing a complex system with shape features not observed using the spherical model. We observe what we believe to be Plateau-Rayleigh instabilities, where the tubule is driven to pinch apart to decrease surface-tension energy.

Chapter VI describes the last iteration of the original planar model, this time being extended to include an additional physical aspect of lipid membranes: how the two leaflets of the bilayer individually affect each other and the entire membrane system. The geometry is assumed to be of the nearly planar configuration, but the compositions of the two leaflets are treated individually, and the spontaneous curvature is defined as a function of the leaflet compositions and how the components in the two leaflets preferentially interact. The effects of this interleaflet interaction on the dynamics and equilibrium morphologies is investigated, producing morphological phase diagrams and contrasting them at different relative interleaflet coupling strengths.

Lastly, Chap. VII discusses overarching conclusions drawn from the investigations in each chapter, potential experimental studies that could be performed to complement this work, applications in medicine and biotechnology that the reported results could impact, and ideas for future studies to build on this work.

CHAPTER II

Background

2.1 Literature Review

This section will present a review of work that has been published in the field of computational studies of lipid membranes. Although computational tools have been applied to study a wide range of membrane phenomena, we focus on studies that examine membrane aspects that are relevant to the work presented here. Some of the membrane phenomena not discussed here include membrane poration and stalk formation, the formation of nonbilayer phases, interactions between membranes and proteins, and the effects of charged molecules on membranes. The following discussion will cover two main modeling approaches: particle-based modeling and continuum-level modeling. The particle-based models will further be broken up into molecular dynamics modeling, coarse-grained modeling, and Monte Carlo methods.

Molecular Dynamics (MD) modeling is a particle-based approach using an atomistic representation. This representation can either treat each atom individually (all-atom), or, more commonly, includes a small degree of coarse-graining where a carbon bonded to hydrogen atoms is treated as a single particle (united-atom) (97). This coarse-graining is done to improve computational efficiency; various degrees of coarse-graining will be described later in this section. Whether the atoms or small particles are represented, MD simulations use force fields to describe how the atoms/particles interact. For example, these force fields can be used to describe the nature of chemical bonds. The spatial location of each atom/particle is tracked, and using the force fields governing their interactions with neighboring particles, trajectories can be generated using Newton's equations of motion to map how the atom/particle locations change over time. Commonly used simulation packages include CHARMM (98, 99), GROMACS (100, 101), NAMD (102), and LAMMPS (103), as reviewed in Refs. 104 and 105.

While computational resources and parallelization methods continue to improve, length and time scales accessible in MD simulations are limited to nanometers and nanoseconds, respectively. This makes it difficult to apply MD methods to simulate heterogeneous membranes since in these systems diffusion occurs over time and length scales larger than those accessible using MD. However, MD simulations of pure, binary, and ternary mixtures have been carried out and are useful for making connections between molecular properties, such as the structure and size of the lipid headgroups and tailgroups or the presence of cholesterol, and local and global properties of the membrane, including molecular order (106–108), hydrogen bonding (106, 109), interactions between lipids and cholesterol (110–115), bilayer thickness (112, 113), and elastic properties (104, 113). These simulations tend to include on the order of one to two thousand (or less) lipids and in some cases roughly $50,000$ water molecules, for periods of 20 to 200 nanoseconds.

A variation on MD models called coarse-grained (CG) models have been developed, where instead of representing every molecule, clusters of molecules are represented, trading atomistic detail for access to larger length and time scales than traditional MD methods. Different levels of coarse-graining applied to a lipid molecule are presented in Fig. 2.1, including the united-atom MD coarse-graining. While the description of the molecules differs in CG compared to MD models, the same basic ideas carry over, where interaction potentials define molecule trajectories. CG

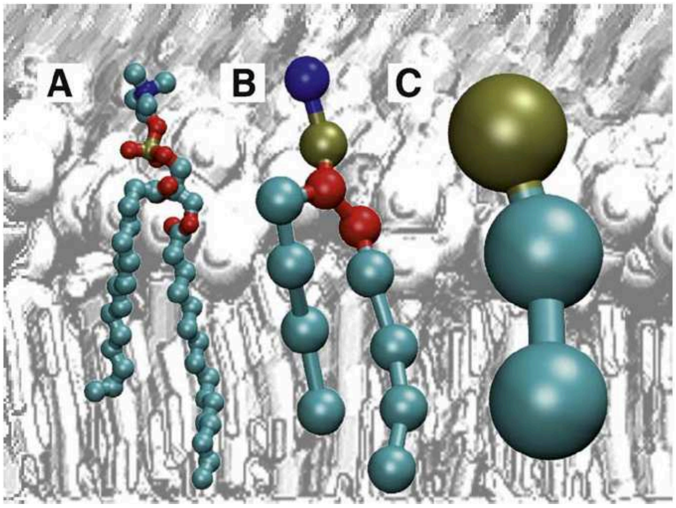

Figure 2.1: Various representations of a lipid molecule: united-atom MD (A), and two levels of coarse-grained representations, with more (B) or less (C) atomistic detail. Representations with a higher degree of coarse-graining can access larger length and time scales, though less atomistic detail is retained. Reproduced from Ref. 97.

simulations have been used to investigate a wide variety of topics (104, 116, 117), including measurements of fundamental membrane elastic properties (118–120), the effects of factors such as tailgroup length or inclusion of cholesterol on lipid phase behavior (at a larger length scale) (121–123), the dynamics of asymmetric lipid bilayers (124), and entire phase-separated vesicles (125) (at an even larger length scale). A particular version of the CG technique known as Dissipative Particle Dynamics (DPD) uses a "bead-and-spring" model for lipid molecules, representing a lipid as a hydrophilic headgroup bead and hydrophobic tailgroup beads, in a system with water molecule beads. Soft, repulsive non-bonded potentials between molecules define the difference between hydrophilic and hydrophobic beads, such that like-beads prefer to interact with each other (116). DPD techniques have been used to study relationships between lipid architecture and surface tension (126), and the dynamics of phase-separated lipid vesicles (127, 128).

An alternative to the MD and CG algorithm is a simulation technique known as the Monte Carlo (MC) method. In MC modeling, atom or particle configurations are evolved with "trial moves," where the energy of a potential new configuration is calculated, and whether it is adopted or not depends on the change in energy it accompanies in combination with a probability function to add a stochastic element. This method has the advantage that, since actual trajectories are not computed, equilibrium states can be reached relatively quickly by using the right trial moves. However, MC trial steps introduce nonphysical kinetics into the model, and investigations of certain time-sensitive properties (for example, those related to transport) are not well-suited to MC simulations (116). Kinetic Monte Carlo (KMC) is a variation on the MC method that incorporates kinetics into the model. This is done by assigning each trial move with an attempt frequency that reflects an effective rate constant of the associated process, such that the trial moves allowing a particular process to progress have a higher probability of being selected if that process occurs more quickly.

MC simulations have been used to study membranes at atomistic scales and more macroscopic scales, investigating phenomena ranging from bilayer self-assembly (129, 130) to surface tension and bending and compression moduli (122, 129) to phase separation and/or domain budding in membrane vesicles (131, 132). KMC simulations have been used to investigate dynamic shape instabilities in membranes (133), diffusion dynamics related to clathrin pits (134), and phase separation in asymmetric membranes (135).

The second class of modeling, an alternative to particle-based models, is to employ continuum-level methods to study dynamical evolution at larger length and time scales. Rather than representing atoms or groups of atoms, these models take the membrane to be smooth and continuous, perhaps as an infinitely thin, deformable sheet or defined as an interface in space (*e.g.*, occupying the interface between oil and water in an emulsion). The system is described with free energy functionals, where the evolution is directed toward the minima in the free energy landscape. These free energy functionals are written in terms of fields or collective variables, such as order parameters. Different values of the order parameter could correspond to different materials or degrees of tailgroup ordering, for example. To solve for continuous variables numerically, they must be discretized on a grid of points distributed over the domain, which can introduce difficulties and artifacts not encountered with particle-based methods. Continuum-level models examining aspects of phase separation in membranes will be the focus of the following discussion.

Continuum-level computational studies that consider coupling of membrane shape with spatially varying composition have been performed in two dimensions with the effects of hydrodynamic flow (136), and in three dimensions both excluding (137, 138) and including (139, 140) spontaneous curvature effects. A continuum approach based on the representation of a vesicle as a level set has been used by Du *et al.* to study complex axis-symmetric shapes in Refs. 141 and 142, and unrestricted three-dimensional shapes in Ref. 138, focusing on the effects of bending energy and line tension. Taniguchi has studied two-phase lipid vesicles using a dissipative dynamical model to investigate how the coupling of the membrane shape with composition can affect the dynamics of domain coarsening (143). Processes contributing to membrane compartmentalization, such as lipid trafficking and interactions with immobile proteins, were examined in Refs. 144 and 145, providing possible explanations for how domains in simple membrane systems can grow to be orders of magnitude larger than lipid rafts in cell plasma membranes. Double membranes are considered in the model in Ref. 139, such as those in some intracellular organelles, and the model includes an interaction term to couple the two membranes, which have differing compositions. Similarly, but in a single bilayer, the two leaflets of a membrane are considered in Ref. 140, where the spontaneous curvature of each of the leaflets is included in the free energy individually.

A variation on pure continuum models is a quasi-particle method called Smooth Particle Applied Mechanics (SPAM). SPAM is a Lagrangian scheme, in which individual membrane mass elements are tracked in space, as if the "grid" follows their trajectories, rather than discretizing the membrane by imposing a fixed grid of points and tracking how state variables change in time at those points. Each SPAM particle is like a small subsystem of the continuum membrane, possessing usual particle quantities such as mass, position, and velocity, but also composition and chemical potential. Particles can exchange not only momentum, but also properties like composition based on free energy functionals typical of traditional continuum models (146). SPAM used with a Landau field theory model was used by Ayton *et al.* (137) to study how domain formations on two-phase vesicle surfaces correlated with deformations. They found that composition responded to geometrical surface perturbations imposed on the vesicle.

In this work, we aim to simulate phase separation and deformation in multicomponent membranes, and have chosen to employ a continuum model with mechanical coupling to do so. A continuum model was selected since the processes we simulate occur on length and time scales that are difficult to access with MD or even CG. Additionally, the Thornton Group has extensive experience using the phase-field method in materials science problems, and we therefore have chosen to use this method for the biological material system of lipid membranes.

2.2 Phase-Field Model

The foundation for the compositional-evolution component of the simulations in this work is the phase-field model (147, 148). This model stems from work done by Cahn, Hilliard, Allen, Landau and Ginzberg beginning in the 1950s (149–153), and has been applied to study a variety of physical phenomena including spinodal decomposition (154, 155), solidification (156, 157), grain growth (158, 159), coarsening of a precipitate phase (160–162), and other phenomena that require interface tracking (163–167) (see Refs. 168 and 169 for reviews on phase-field modeling). The phase-field model uses partial differential equations to govern the spatial and temporal evolution of bulk quantities, such as concentration. It is a diffuse-interface approach, meaning that interfaces are assumed to have a finite volume rather than being infinitesimally thin, making the model more numerically tractable compared with sharp interface models. The locations of interfaces are specified by where these bulk quantities have their interfacial value, and thus the location of the interface does not need to be explicitly tracked.

There are two classes of phase-field models: the Allen-Cahn and the Cahn-Hilliard. The Allen-Cahn models apply to systems with non-conserved quantities, such as crystalline ordering, and will not be discussed further. The Cahn-Hilliard models apply to systems with conserved bulk quantities, such as concentration, as is the case in this work.

We first define a conserved order parameter, in the context of two-phase spinodal decomposition. For a mixture of multiple species, the order parameter represents the concentration of a single species, which is normalized such that the concentration in the two bulk phases is 0 and 1. Such an order parameter, denoted as ϕ, can be constructed from the local concentration of a species, C, and the concentration of that species in the bulk phases at equilibrium, C^e_α and C^e_β:

$$\phi = \frac{C - C^e_\beta}{C^e_\alpha - C^e_\beta}. \tag{2.1}$$

The free energy per unit volume, $\tilde{f}$, within a body Ω is defined in terms of this order parameter and its gradient. The total free energy then is given by the integral of this function over the body:

$$\mathcal{F} = \int\limits_{\Omega} \tilde{f}(\phi, \nabla\phi) dV. \tag{2.2}$$

If this free energy per unit volume is expanded around the bulk homogeneous value, $\tilde{f}(\phi, 0)$, using a Taylor expansion, the following expression is obtained:

$$\tilde{f}(\phi, \nabla\phi) = \tilde{f}(\phi, 0) + \mathbf{L} \cdot \nabla\phi + \frac{1}{2}\nabla\phi \overleftrightarrow{K} \nabla\phi + \ldots \,. \tag{2.3}$$

For a system where the homogeneous materials are isotropic, $\mathbf{L} = \mathbf{0}$ and $\overleftrightarrow{K} = KI$, where I is the identity matrix, since the free energy does not have any directional dependence on the gradient. In this simplified case, with higher-order terms of the Taylor expansion being neglected, the free energy can be written as

$$\mathcal{F} = \int\limits_{\Omega} \Big(f(\phi) + \frac{\varepsilon^2}{2}|\nabla\phi|^2 \Big) dV, \tag{2.4}$$

with the notation ε^2 being substituted for K and $f(\phi) = \tilde{f}(\phi, 0)$. In this expression, the first term describes the bulk free energy, while the second can be viewed as a penalty for sharp composition gradients. The latter, the so-called gradient term, is what gives the model diffuse interfaces, with the width of the interface depending on the value of ε. Once again in the context of spinodal decomposition to form two phases, the bulk free energy $f(\phi)$ is typically a double-well-shaped function with minima at $\phi = 0$ and $\phi = 1$. One example of such functions is $f(\phi) = \frac{W}{4}\phi^2(1-\phi)^2$, used as an approximation of the thermodynamic Flory free energy for ideal mixtures, $g(\phi) \propto A\phi(1-\phi) + \phi \ln \phi + (1-\phi)\ln(1-\phi)$, where A is a constant, in order to improve computational efficiency. Plots of the double-well polynomial used here as well as the Flory free energy are presented in Fig. 2.2.

To model how changes in concentration affect the free energy, variational calculus

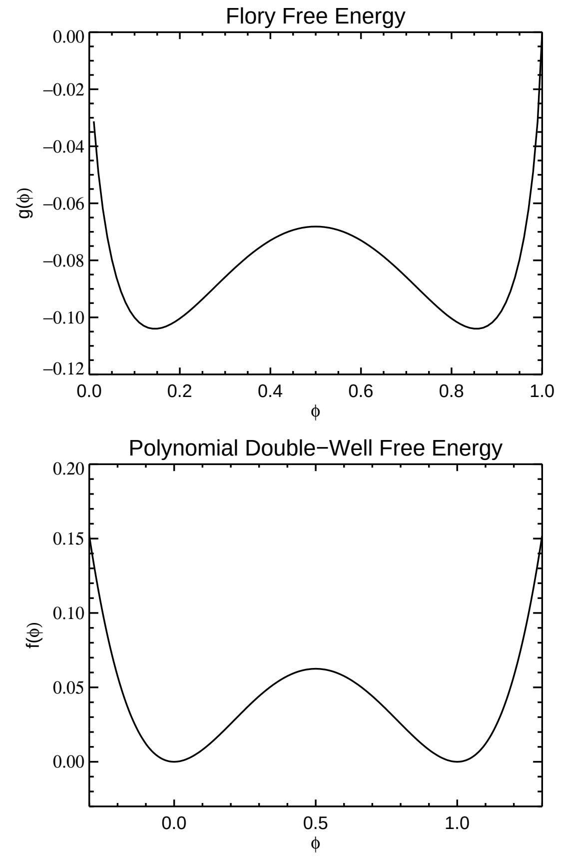

Figure 2.2: Plots comparing the Flory free energy potential, $g(\phi) \propto A\phi(1-\phi) + \phi \ln \phi + (1-\phi)\ln(1-\phi)$ with $A = 2.5$, and the polynomial double-well potential adopted in this model, $f(\phi) = \frac{W}{4}\phi^2(1-\phi)^2$ with $W = 4$, showing qualitative correspondence. The minima of $f(\phi)$ are at $\phi = 0$ and $\phi = 1$, as desired.

is utilized. A quantity similar to chemical potential is defined as

$$\mu = \frac{\delta \mathcal{F}}{\delta \phi} = \frac{df}{d\phi} - \varepsilon^2 \nabla^2 \phi = \frac{W}{2}\phi(1-\phi)(1-2\phi) - \varepsilon^2 \nabla^2 \phi. \tag{2.5}$$

When this chemical potential is uniform, there ceases to be a driving force for changes in concentration and the system is defined to be at equilibrium. To model the concentration change in time, we can write the following expression as a form of Fick's second law, where a concentration changes with the divergence of its flux:

$$\frac{\partial \phi}{\partial t} = -\nabla \cdot \mathbf{J}. \tag{2.6}$$

We can write the flux in terms of the chemical potential defined in Eq. 2.5, since concentration will flow from areas of high chemical potential to areas of lower chemical potential:

$$\mathbf{J} = -M \nabla \mu, \tag{2.7}$$

where M is the mobility, which may be a function of ϕ. Combining Eqs. 2.6 and 2.7, we arrive at a relation between the time derivative of ϕ and spatial derivatives of ϕ:

$$\frac{\partial \phi}{\partial t} = \nabla \cdot (M \nabla \mu), \tag{2.8}$$

which, for a constant mobility, M, and substituting in the form of μ, becomes

$$\frac{\partial \phi}{\partial t} = M \nabla^2 \Big(\frac{W}{2}\phi(1-\phi)(1-2\phi) - \varepsilon^2 \nabla^2 \phi \Big). \tag{2.9}$$

For a two-component system in 1D, Eq. 2.9 has four possible steady-state solutions, though three of them are trivial. The first two are for a homogeneous system where $\phi = 0$ or $\phi = 1$ everywhere; the third is where $\phi = 0.5$ but is unstable and unphysical. The fourth solution is where there is a single interface between homogenous regions

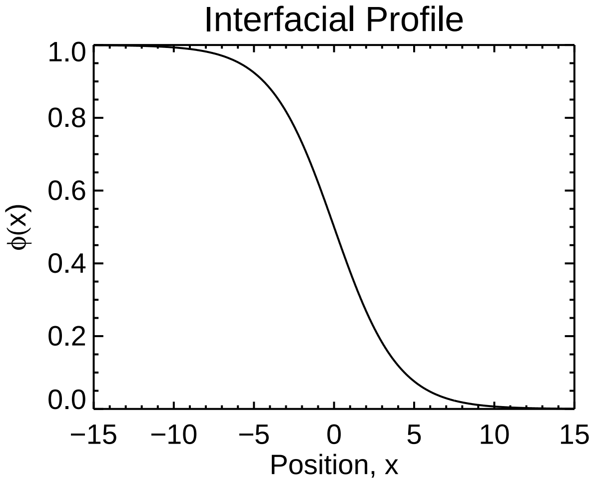

Figure 2.3: The interfacial profile of the order parameter ϕ vs. position. The width of the interface as defined by the ϕ range of 0.1-0.9 is 4δ, where δ is a parameter that sets the width in Eq. 2.10. The interface is approximately 8 position units on this plot.

with $\phi = 0$ and $\phi = 1$, where the interface has the form

$$\phi(x) = \frac{1}{2}\Big(1 - \tanh\left(\frac{x}{2\delta}\right)\Big), \tag{2.10}$$

as illustrated in Fig. 2.3. The width of the interface as defined by the ϕ range of 0.1-0.9 is given by 4δ, where δ can be related to the parameters in the free energy, f, as

$$\delta = \varepsilon\sqrt{2/W}. \tag{2.11}$$

This interfacial width results from the competition between the gradient term that drives the interface to widen and the bulk free energy term that drives it to be more narrow. If the parameters are set such that the interface is too wide to accurately model the physical system, then the diffuse interface approach has failed. To ensure that the interface is sufficiently narrow, it must be significantly smaller than the characteristic length of the system l, $\delta/l << 1$.

2.3 Finite Difference Method

The fourth-order partial differential equations presented in the previous section are nonlinear, and must be solved numerically. This means that the continuous functions and variables must be discretized so that numerical computations can be performed. For a continuous variable x, where $X_1 < x < X_2$, its discretized representation will have values at N points in the interval $[X_1, X_2]$, as

$$x_i = X_1 + \sum_{k=1}^{i-1} \Delta x_k, 1 < i \leq N, \tag{2.12}$$

where Δx_k is the spacing between adjacent points, as $\Delta x_k = x_{k+1} - x_k$. A continuous function can then be translated to a discrete function by being defined in terms of the discrete variable points x_i as

$$q_i = f(x_i). \tag{2.13}$$

Of course there is information lost between a continuous function and a discrete representation of that function, so care must be taken to ensure that the discrete points are spaced closely enough to capture the sharpest features (*i.e.*, the most rapid changes) in the continuous function. The finite difference method can then be used to calculate derivatives of the discrete function with respect to the discrete variable based on Taylor expansions.

A Taylor expansion can be used to approximate the value of the function f at a point near x_i, such as $q(x_{i+1})$. The expression for the Taylor expansion for $q(x_{i+1})$ around x_i with uniform grid spacing, Δx, is

$$q(x_{i+1}) \approx q(x_i) + q'(x_i)\Delta x + \frac{1}{2!}q''(x_i)(\Delta x)^2 + \frac{1}{3!}q'''(x_i)(\Delta x)^3 + \ldots . \tag{2.14}$$

Similarly, the Taylor expansion for $q(x_{i-1})$ around x_i is

$$q(x_{i-1}) \approx q(x_i) - q'(x_i)\Delta x + \frac{1}{2!}q''(x_i)(\Delta x)^2 - \frac{1}{3!}q'''(x_i)(\Delta x)^3 + \dots . \tag{2.15}$$

By subtracting the expression approximating $q(x_{i-1})$ from the expression approximating $q(x_{i+1})$, the derivative of interest, $q'(x_i)$, can be obtained:

$$q'(x_i) \approx \frac{q(x_{i+1}) - q(x_{i-1})}{2\Delta x} - \frac{1}{3!}q'''(x_i)(\Delta x)^2 - \dots . \tag{2.16}$$

If the second term and the following higher-order terms in Eq. 2.16 are neglected, the expression has an error on the order of $(\Delta x)^2$, and can then be written as

$$q'(x_i) \approx \frac{q(x_{i+1}) - q(x_{i-1})}{2\Delta x}, \tag{2.17}$$

giving a second-order-accurate expression for the derivative of q at x_i in terms of $q(x_{i+1})$ and $q(x_{i-1})$, making it a centered finite difference. This scheme is used to calculate derivatives in space in this work. A forward Euler (fully explicit) scheme is used to calculate temporal derivatives, which can be obtained similarly. As with spatial variables, time is discretized, and the scheme can be expressed as

$$\frac{\partial q(t_i)}{\partial t} = \frac{q(t_{i+1}) - q(t_i)}{\Delta t} + O(\Delta t), \tag{2.18}$$

where Δt is the timestep. The expression can be rearranged to obtain the discretized equation for integration in time:

$$q(t_{i+1}) = \frac{\partial q(t_i)}{\partial t}\Delta t + q(t_i). \tag{2.19}$$

In this form, it is clear that the value of the function q at the future time $t + \Delta t$ can be calculated from quantities at the current time t, making it an explicit method.

This is computationally advantageous as only simple algebra is required to calculate the value of the function at the future time. However, the size of the time step Δt is typically constrained to be quite small, on the order of $(\Delta x)^4$, to maintain numerical stability.

CHAPTER III

Planar Membrane Model

3.1 Introduction

Planar lipid monolayers and bilayers are commonly used as model systems to study phase separation in multicomponent membranes. Monolayers are typically formed at a water/air or water/oil interface, while bilayers can be formed in aqueous environments in various configurations. Planar bilayers can be formed on a rigid surface, with or without a spacer between the membrane and surface such as polymer chains or multiple layers of membranes (71, 88, 170–173). A spacer would be used so that the mobility of the membrane components is not altered as a result of interactions between the membrane and surface. Bilayers can also be created in unsupported configurations, where they may for example span a pore or gap in a rigid support rather than sit on top of the support. This configuration is useful for studying membrane protein transport between two chambers on either side of the bilayer-spanning pore/gap (174–176).

While perfectly planar membranes are not found in nature, they are still a valid membrane model since the physics of the lipid bilayer is intact. They are a suitable approximation of a portion of a large, overall spherical membrane where the curvature is negligible on the length scale studied. The model for planar membranes presented here applies to such "nearly planar" portions of membrane structures that have curvature on much larger length scales, such as giant vesicles and cell plasma membranes. The model is used to simulate unsupported and supported planar bilayers, since supported bilayers have potential for technological applications such as biosensors, as discussed in Sec. 1.2.1.

We present a continuum-level method for modeling phase transitions and corresponding morphological evolution of binary lipid membranes with approximately planar geometries, as presented in our work in Ref. 177. Our model is based on Cahn-Hilliard-type dynamics as in Ref. 137, but it explicitly treats the full nonlinear form of the geometrical scalars, tensors, and differential operators associated with the curved shape of the membrane. The model is applied to examine morphological evolution and stability of lipid membranes.

3.2 Methods

The morphological behavior of homogeneous vesicles and membranes can be quantified by the Helfrich free energy (178). This free energy is based on a continuum model that treats the membrane as a smooth surface. The spatial shape of the surface can be described by a three-dimensional coordinate function $\mathbf{x}(\mathbf{u})$ that depends on a two-dimensional coordinate $\mathbf{u}$, which parametrizes the surface. This model considers the energy cost of bending deformations away from conformations with the spontaneous curvature, *i.e.*, the preferred curvature originating from the molecular shapes and interactions. This model applies to monolayers and asymmetric bilayers. In addition, this formulation includes a Lagrangian multiplier, the surface tension, to control the value of the total area of the membrane.

The basic Helfrich model can be extended to multicomponent systems (179, 180). In a binary system with components A and B, we consider phase coexistence between two phases, α and β, with majority components A and B, respectively. The concentration of B in these phases is c_α and c_β, respectively; we denote the positiondependent concentration of B simply as c. We introduce a scaled composition function $\phi = (c - c_\beta)/(c_\alpha - c_\beta)$ that takes values between 0 and 1, which is referred to as an order parameter in phase-field modeling. In the strong-segregation limit, when the components are highly immiscible, most of the membrane area is occupied by single-phase regions with compositions of $\phi = 0$ or $\phi = 1$. In the boundary region between two phases, the composition field smoothly transitions between these values. Compared to the homogenous case, the energy of the system is modified in two ways; first, it is necessary to describe the immiscibility of the components, and second, each of the phases may have different mechanical properties.

Below, we write all contributions to the energy density and the resulting dynamical equations in covariant form. Specifically, the equations are independent of both the coordinate systems used for the position of the membrane surface and those used to parametrize it. At the end of the section we specialize the resulting equations to a particular type of coordinate system, the Monge gauge.

3.2.1 Free Energy Contributions

The modified Helfrich free energy F of a binary membrane can be written as an integral of an energy density H over the surface of the membrane. We decompose the density H into three terms,

$$F = \int H dA = \int (H_0 + H_1 + H_2) dA. \tag{3.1}$$

The first energy density H_0 describes the thermodynamics of the mixture. We use the standard Landau form (147),

$$H_o = \frac{w}{4}\phi^2(1-\phi)^2 + \frac{\zeta^2}{2}\nabla^i\phi\nabla_i\phi, \tag{3.2}$$

where w defines the barrier height in the double-well free energy (as in Fig. 2.2) and ζ sets the energetic penalty for composition gradients. In the absence of other interactions, the double-well free energy in the first term produces two phases at $\phi = 0$ or $\phi = 1$. The second term penalizes the presence of composition gradients. The coefficients w and ζ can be adjusted to describe the strength of the immiscibility with respect to the mechanical effects. In this work, we examine the strong-segregation regime, where, for flat systems, the equilibrium line tension of a straight interface between species can be identified as $\lambda = (w\zeta^2/72)^{1/2}$.

The gradient, divergence, and Laplace operators that appear in this formulation act on functions defined only at the surface of the membrane. We use the standard notation of subindices and superindices for contravariant and covariant vectors, respectively, as well as the index summation convention. These indices identify generalized coordinates that parametrize the surface. Explicit expressions for these differential operators are derived by applying the standard techniques used in general relativity. The results are given in covariant form and in the Monge gauge in Appendix A. Vector quantities appear in bold face, vector components are written within square brackets, and unit vectors are denoted with hats.

The second energy density is a modification of the original Helfrich Hamiltonian that describes the mechanical properties of the membrane,

$$H_1 = \frac{\Lambda_\alpha}{2} p(\phi)(K - C_\alpha)^2 + \frac{\Lambda_\beta}{2}(1 - p(\phi))(K - C_\beta)^2, \tag{3.3}$$

which represents the energy penalty for having a curvature that differs from the spontaneous curvature. In this expression, each term is a standard bending energy with bending rigidity Λ_α or Λ_β and spontaneous curvature C_α or C_β, and we introduce an interpolation function $p(\phi)$ to interpolate the energies in regions that do not correspond to a single phase ($\phi \neq 0, 1$), as discussed later. We have written the Helfrich expressions in terms of K, the trace of the curvature tensor K_{ab}, which is equal to twice the mean curvature. We will refer to this quantity as the curvature trace, for short, following the notation used in Ref. 181. We consider in this chapter only the case in which the two phases have equal bending rigidities $\Lambda_\alpha = \Lambda_\beta$ but have different spontaneous curvature values. These values are C_α for the phase with $\phi = 1$, and C_β for the phase with $\phi = 0$. To interpolate the energy between these values, we use a smooth function $p(\phi) = \phi^3(10 - 15\phi + 6\phi^2)$ that has the properties that $p(0) = 0$, $p(0.5) = 0.5$, $p(1) = 1$, and $\frac{dp}{d\phi}\big|_{\phi=0} = \frac{dp}{d\phi}\big|_{\phi=1} = 0$. This particular form of an interpolation function is obtained by integrating $\phi^2(1-\phi)^2$ (182), which has the form of the double-well function we adopted. However, other choices of interpolation functions satisfying these prescribed properties are equally valid (*e.g.*, $p(\phi) = \phi^2(3-2\phi)$), given that the function is numerically resolved and that the interfacial (interpolated) region is taken to be sufficiently thin. They provide thermodynamic consistency as discussed in Ref. 182. While a very simple interpolation function could be considered ($p(\phi) = \phi$ for example), the chosen form has a proper behavior near $\phi = 0$ and $\phi = 1$ and helps to ensure that the positions of the free energy minima remain at $\phi = 0$ and $\phi = 1$ for all curvatures outside of interfacial regions. We define a local average of the spontaneous curvature as $C_f = p(\phi)C_\alpha + (1 - p(\phi))C_\beta$.

We note that this mechanical energy term has a contribution to the magnitude of the line tension, and thus in general the line tension does not have the value given nominally by the well height of the double-well free energy and the gradient-energy coefficient appearing in Eq. (3.2). The change in the line tension is described by the Gibbs adsorption equation (153, 183, 184), and the resulting effect is similar to that obtained for surface stress effects in solidification (185). However, when the interfacial thickness is much smaller than the length scale given by the ratio of the interfacial energy to the bulk energy density, the excess becomes negligible (185–187). This is because the excess energy resulting from the bulk energy term scales with the interfacial thickness, while the parameters are set such that the line tension is independent of the interfacial thickness. A similar principle applies here. To ensure accuracy, we choose the interfacial thickness to be much smaller than the inverse of the spontaneous curvatures and a length scale given by the approximate ratio of the line tension to the mechanical energy density $\sim \lambda/\Lambda_{\alpha,\beta}$.

The third term controls the total area of the membrane, and is given simply by a constant surface tension:

$$H_2 = \sigma. \tag{3.4}$$

The tension σ is an isotropic contribution to the stress tensor that opposes an increase in the membrane area. This term arises from a coarse-graining of cohesive forces between the molecules that form the membrane, including hydrophobic forces. Upon integration of this density, we obtain a linear coupling of the tension and the total area of the membrane, A.

3.2.2 Deformations and Dynamics

Our model describes both the equilibrium configurations and the dynamical approach toward equilibrium of lipid membranes. The equilibrium configurations that result from the above free energy are determined from suitable minimization of the functional with respect to shape and local composition. To describe the dynamics of the system, more information is required. We propose a simple dynamical scheme that couples shape deformations and compositional redistribution.

The structure of the dynamical equations of a homogeneous membrane that obey the covariant condition has been previously studied by Cai and Lubensky (188). Among the possible reductions of the full dynamics to a manageable set of variables, they considered a Rouse model without inertial terms. This approximation is still covariant, but neglects inertial terms and tangential forces. The forces generated by deformations of the membrane are then compensated for by friction terms proportional to the normal velocity of the membrane. We adopt this approach to the study of the dynamics of multicomponent systems. The free energy change associated with a normal deformation $\psi\hat{\mathbf{n}}$ (see Fig. 3.1) can be written as the integral $\delta F = -\int T\psi \, dA$. T is the generalized force density that couples to the displacement ψ. Expressions for this force are well known for homogeneous membranes. In the case of multicomponent systems, the proper expressions are most easily obtained using the covariant methods of Capovilla *et al.* (181), and are presented explicitly below and derived in Ref. 177. The normal velocity field is $\mathbf{v}_n = \partial_t\psi\hat{\mathbf{n}}$, where ∂_t denotes a partial derivative with respect to t, and the friction force opposing the motion is given by

$$\mathbf{f}_v = -\mathbf{v}_n/\Gamma = -\partial_t\psi\hat{\mathbf{n}}/\Gamma, \tag{3.5}$$

where Γ is the inverse of the friction coefficient. The dynamical equation is then obtained from the condition $T\hat{\mathbf{n}} + \mathbf{f}_v = \mathbf{0}$:

$$\begin{aligned} \frac{\partial\psi}{\partial t} &= \Gamma T, && (3.6) \\ -T &= HK + Q(R - K^2) && (3.7) \\ &\quad -\nabla^2 Q - \zeta^2 K^{ab}\nabla_a\phi\nabla_b\phi, && \end{aligned}$$

where $Q = \frac{\partial H_1}{\partial K} = \Lambda_\alpha p(\phi)(K - C_\alpha) + \Lambda_\beta(1 - p(\phi))(K - C_\beta)$, ∇^2 is the Laplace operator, and K^{ab} is the curvature tensor (see Appendix A). The shape equation (*i.e.*, the equation governing the morphology of the membrane surface) in equilibrium is simply $T = 0$. The shape equation of a homogeneous membrane is recovered when the composition field is set to one of the two equilibrium phase values.

The local composition of the membrane is modified both by diffusion processes and advection by tangential displacements. As mentioned above, to obtain a simple effective dynamical scheme we assume that the local composition field evolves by means of diffusional processes. The diffusion is driven by gradients in the chemical

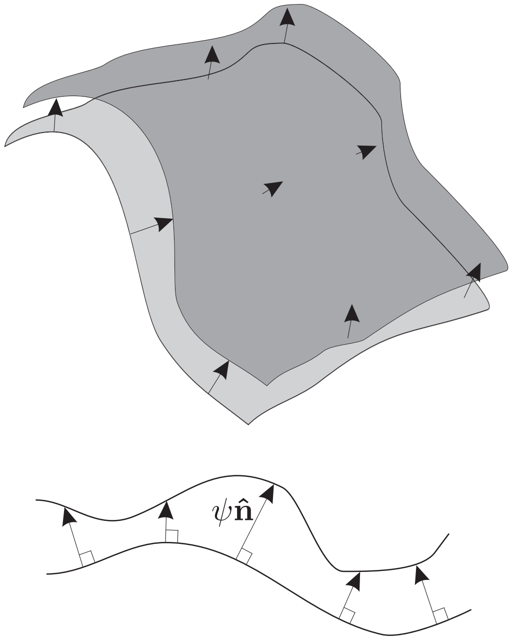

Figure 3.1: A schematic illustrating membrane deformations, showing how each point of the membrane can be mapped onto a new point in the deformed membrane located a distance ψ away from its initial location, in the direction of the unit normal vector $\hat{\mathbf{n}}$ at that point.

potential of the species. For a binary system it is sufficient to consider the diffusion of just one of the components, say B, which is proportional to ϕ. A chemical potential μ for phase composition is obtained from variation of the free energy with respect to the composition field ϕ, $\delta F = \int dA\, \mu \delta\phi$. Simple model dynamics are obtained by assuming that the flux, j_i, of the scaled composition (per unit time and unit area) is proportional to the gradient of the chemical potential, *i.e.*, $j_i = -M\nabla_i \mu$, where M is an effective mobility, assumed constant throughout this work. The rate of composition change is then given by $\partial_t \phi = -\nabla^i j_i$. Combining these equations we obtain a Cahn-Hilliard-type dynamics for the composition:

$$\begin{aligned} \frac{\partial \phi}{\partial t} &= M\nabla^2 \mu, && (3.8) \\ \mu &= \frac{w}{2}\phi(1-\phi)(1-2\phi) - \zeta^2 \nabla^2 \phi && (3.9) \\ &\quad + \frac{p'(\phi)}{2}(K^2(\Lambda_\alpha - \Lambda_\beta) + 2K(\Lambda_\alpha C_\alpha - \Lambda_\beta C_\beta) + (\Lambda_\alpha C_\alpha^2 - \Lambda_\beta C_\beta^2)). \end{aligned}$$

Equilibrium is achieved when the chemical potential becomes uniform so that its gradient is zero. Normal deformations that change the shape leave the composition invariant. It is necessary, however, to consider the change of composition at fixed background points induced by the normal motion; this is considered at the end of this section.

The dynamical equations proposed above can be solved numerically using various methods. Since the dynamics of the shape has been reduced to that of a single scalar variable, it is viable to use the Monge gauge. That is, after setting a fixed geometrical background, we describe the shape of a membrane by specifying its projection onto the background. We require that this projection be one-to-one. These shapes are then described by a single "height" function, $h(\mathbf{u})$, as shown in Fig. 3.2. The dynamical behavior of the system can then be reduced to the time evolution of the composition

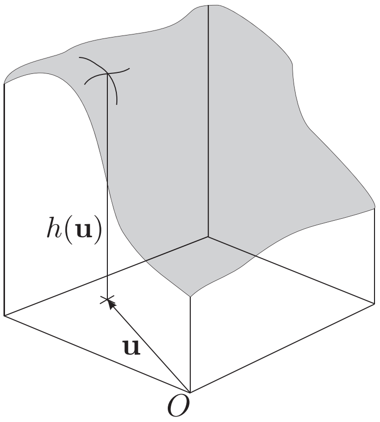

Figure 3.2: A schematic illustrating one-to-one projection of the membrane surface onto the background surface. In this case, every shape can be described by a single "height" function $h(\mathbf{u})$.

ϕ and the height variable. To obtain an explicit numerical scheme, it is necessary to write all the geometric invariants and differential operators that appear in our equations in terms of the height.

We consider only membrane shapes that can be projected one-to-one onto the background plane. A point within the surface is described by its Cartesian coordinates $\mathbf{x} = [x_1, x_2, x_3]$, and we define the reference plane to lie in the $x_3 = 0$ plane so that a point in the reference plane has coordinates $\mathbf{u} = [u_1, u_2, 0] = [x_1, x_2, 0]$. The third coordinate of a point on the surface is then $x_3 = h(u_1, u_2)$, and

$$\mathbf{x} = [u_1, u_2, h(u_1, u_2)]. \tag{3.10}$$

We can write expressions for vectors tangent to the surface as

$$\mathbf{e}_1 = \frac{\partial \mathbf{x}}{\partial u_1} = [1, 0, h_1], \tag{3.11}$$

$$\mathbf{e}_2 = \frac{\partial \mathbf{x}}{\partial u_2} = [0, 1, h_2], \tag{3.12}$$

where we use the shorthand h_i for the partial derivatives of h with respect to u_i.

The explicit forms of the relevant geometric quantities and operators are presented in Appendix A. To use our dynamical equations in this setting, we need to (i) transform the normal deformation rate, $\partial\psi/\partial t$, into a rate of change of the height function, $\partial h/\partial t$, and (ii) describe the rate of change of the composition at a physical point in terms of the rate of change at a fixed background point.

Let us consider the first problem, with the vectors in the following discussion illustrated in Fig. 3.3. For a normal deformation of $\psi\hat{\mathbf{n}}$, the height changes from $h\hat{\mathbf{z}}$ to $(h+\Delta h)\hat{\mathbf{z}}$, where $\hat{\mathbf{z}}$ is a unit vector in the z-direction (normal to the reference plane). If $\hat{\mathbf{n}}$ and $\hat{\mathbf{z}}$ are not parallel, the projection of $\hat{\mathbf{z}}$ along the membrane surface lies along a unit vector $\hat{\mathbf{t}}$ tangent to the surface such that $\hat{\mathbf{z}} = (\hat{\mathbf{z}}\cdot\hat{\mathbf{t}})\hat{\mathbf{t}} + (\hat{\mathbf{z}}\cdot\hat{\mathbf{n}})\hat{\mathbf{n}}$. A general height change can then be written as $\Delta h\hat{\mathbf{z}} = \psi\hat{\mathbf{n}} + s\hat{\mathbf{t}}$. By taking the dot product of both sides of this equation with $\hat{\mathbf{n}}$, we arrive at

$$\Delta h(\hat{\mathbf{z}}\cdot\hat{\mathbf{n}}) = \psi, \tag{3.13}$$

$$\Delta h = \frac{\psi}{\hat{\mathbf{z}}\cdot\hat{\mathbf{n}}} = \frac{\psi}{\sqrt{g}}, \tag{3.14}$$

where g is the metric factor as defined in Appendix A. Finally, the rate of change of the height function can be written as

$$\frac{\partial h}{\partial t} = \Gamma g^{1/2} T. \tag{3.15}$$

To address the second problem, the composition at a point above a background plane point $\mathbf{u}$ changes not only due to diffusion but also due to the motion of the surface:

$$\begin{aligned} \partial_t\phi\big|_{\mathbf{u}} &= \partial_t\phi\big|_{diff} + \partial_t\phi\big|_{ad}, \\ \partial_t\phi\big|_{ad} &= (g^{ij} z_i \nabla_j \phi)\partial_t h. \end{aligned} \tag{3.16}$$

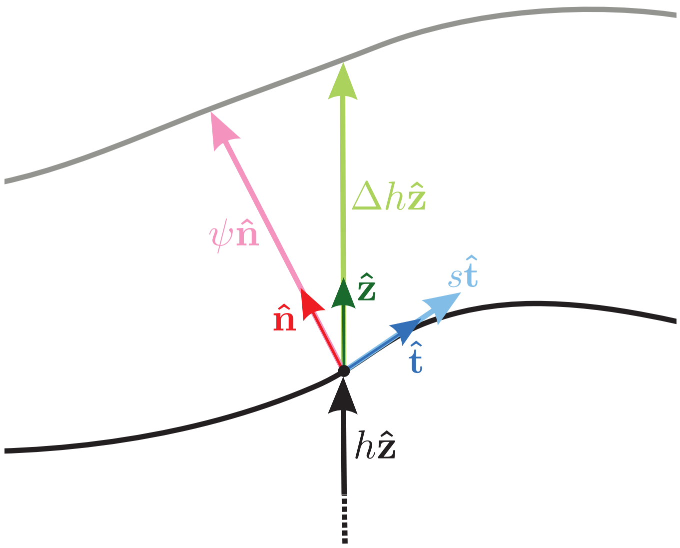

Figure 3.3: Illustration of the vectors involved in the conversion from deformation ψ to a change in height Δh. The current deformed surface is shown in black and the future deformed surface in gray. The black vector $h\hat{\mathbf{z}}$ is drawn from the reference plane at $h = 0$ (not shown), and all other vectors are drawn from the grid point on the current surface. The unit vectors $\hat{\mathbf{z}}$, $\hat{\mathbf{n}}$, and $\hat{\mathbf{t}}$ lie in the z direction, normal to the deformed surface, and tangent to the deformed surface, respectively. The height change vector, $\Delta h\hat{\mathbf{z}}$, can be expressed in terms of the normal deformation vector, $\psi\hat{\mathbf{n}}$, and a scaled version of the tangent vector, $s\hat{\mathbf{t}}$.

In these expressions, z_i is the inner product of $\hat{\mathbf{z}}$ and the basis vectors $\mathbf{e}_i$, $z_i = \hat{\mathbf{z}} \cdot \mathbf{e}_i$. The derivative $\partial_t \phi\big|_{\mathbf{u}}$ measures the composition change at fixed background coordinates. The diffusional contribution, $\partial_t \phi\big|_{\mathit{diff}}$, is determined by the Cahn-Hilliard-type dynamics as given in Eq. (3.8). The advection term, $\partial_t \phi\big|_{ad}$, is determined as follows. The Lagrangian derivative is related to the Eulerian derivatives by $D\phi/Dt = \partial\phi/\partial t + \partial_t u^i \partial_i \phi$, and is identically zero when only advection is considered. Therefore, we have $\partial_t \phi\big|_{ad} = -\partial_t u^i \partial_i \phi$. To express $\partial_t u^i$ in terms of known quantities, we first decompose the height change rate vector $\partial_t h \hat{\mathbf{z}}$ into two vectors, one the normal deformation and the other tangential to the surface. Thus,

$$\partial_t h \hat{\mathbf{z}} = \partial_t \psi \hat{\mathbf{n}} + \xi^j \mathbf{e}_j. \tag{3.17}$$

The advection rate in the reference plane is $\partial_t u^i \hat{\mathbf{w}}_i$, where $\hat{\mathbf{w}}_i$ is a unit vector within the reference plane. Since $\mathbf{e}_i$ projects onto the unit vector $\hat{\mathbf{w}}_i$, we have $\xi^i = -\partial_t u^i$, or

$$\partial_t h \hat{\mathbf{z}} = \partial_t \psi \hat{\mathbf{n}} - \partial_t u^j \mathbf{e}_j. \tag{3.18}$$

Taking the inner product of both vectors with the $\mathbf{e}_i$ basis, we obtain $\partial_t h z_i = -\partial_t u^j g_{ij}$ that can be rearranged to $\partial_t u^j = -g^{ji} z_i \partial_t h$, and the expression in Eq. (3.16) follows.

3.2.3 Numerical Methods

The dynamical scheme presented above for the geometric and compositional changes can be studied numerically in terms of two fields: the phase composition and height with respect to a background geometry. Orthogonal lattices consisting of 64 by 64 mesh points are used to discretize the composition and height on a computational domain of size 2.25 by 2.25. This cell size was selected to ensure that the lowest energy morphological phase is stripes. Energy and length scales of the system can be set by the bending rigidity and spontaneous curvature of phase α. Specifically, we measure all energies in units of the bending rigidity of the α phase, Λ_α, and all lengths in units of the radius of spontaneous curvature of the α phase, C_α^{-1}. The line tension, surface tension, spontaneous curvature of phase β, and compositional area fraction are all independent parameters.

Derivatives are calculated using the finite difference method, with a second-order centered-differencing scheme for spatial derivatives and an explicit time-stepping scheme for time derivatives, as discussed in Chapter II. The size of the time step is determined to provide numerical stability. Periodicity is imposed on all four boundaries of the computational domain. Mass and surface area are not conserved quantities as we allow deformation of the surface. However, in the cases considered herein, they deviate only minimally from the initial values throughout the evolution (typically, surface area increases by $1\% - 4\%$, resulting in area fraction changes of $1\% - 4\%$). Compositional interfaces are resolved with a minimum of six lattice points to preserve numerical accuracy.

An analytical extended phase diagram (including compositional and morphological phases) presented in Ref. 179 indicates a phase with a periodic stripe-like arrangement of single-phase domains for a range of concentrations, spontaneous curvatures, line and surface tensions. Harden *et al.* (180) have also studied membranes analytically; their model predicts a similar stripe morphology in systems with low line tension and near-symmetric compositions. In order to further investigate this stripe morphology, we numerically simulate the approach toward equilibrium using parameters suggested in Ref. 179, defined as follows: $\lambda = 0.5, \sigma = 0.4, C_\alpha = 1, C_\beta = -1, \phi_{avg} = 0.4, \Lambda_\alpha = \Lambda_\beta = 1$. In addition, we set $w = 120, \zeta = \sqrt{0.15}, M = 1$, and $\Gamma = 30$. Figure 3.4 shows a plot of a cross-section of the height profile for the stripe morphological phase, comparing analytical results (189) and the simulation.

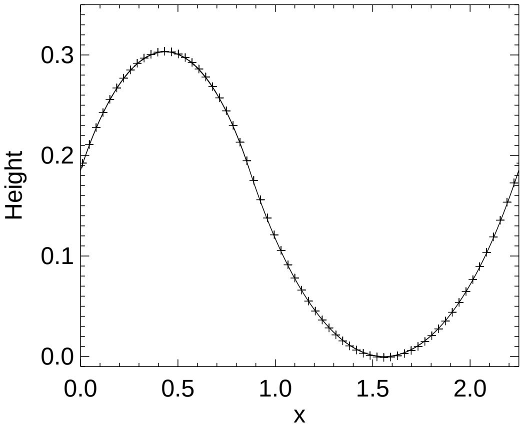

Figure 3.4: One-dimensional plot of a cross-section of the height profile for a stripe morphological phase, comparing analytical (189) and simulation results. Line: the analytical result, symbol: the simulation result.

3.3 Results and Discussion

In the membrane systems investigated, dynamical mechanisms and a competition between multiple driving forces determine the evolution and stable late-stage configurations. These driving forces result from the system's attempt to reduce the sum of surface-tension energy, line-tension energy, and bending energy. In addition, the model includes two pathways for relaxation of non-equilibrium states: the normal deformation of the membrane and diffusional processes that transport material within the membrane. Surface-tension energy is minimized when the membrane is exactly planar; any deformation away from the plane increases the surface-tension energy. The line-tension energy is lowered when the length of the interface between phases is reduced. This can be accomplished both by the process of coarsening, where multiple small domains evolve into fewer, larger domains, and also by domains bulging away from the membrane plane. Bending energy is minimized when domains are able to adopt the curvature preferred by that phase (the spontaneous curvature). We assume that the diffusion process is slower than normal deformations, and thus the evolution

Table 3.1: Summary of compositional and geometrical initial conditions used for the simulations.

	Case Number			
	1	2	3	4
Composition	Random Noise	Random Noise and Stripe Perturbation	Random Noise or No Perturbation	Random Noise or No Perturbation
Geometry	Flat	Flat	Ripple Perturbation	Fixed Ripple

is effectively governed by diffusion, with the geometric shape minimizing the total energy for a given membrane composition.

While there exists a lowest-energy state for a given parameter set, it is unknown whether a phase-separating system will reach such a state or how it evolves toward it. Thus, we investigate membrane systems with the same parameter set but different initial conditions. The height profile is initialized in one of two ways: set to zero everywhere (flat) or offset from zero with a small perturbation imposing a periodic ripple structure. Furthermore, in one of the cases where the height profile is initialized with a ripple perturbation, the height is held fixed and not allowed to evolve with time to simulate a membrane supported on a rigid surface possessing a fixed topography. Composition is initialized in one of three ways: set to a constant value everywhere, set with a small amplitude of uniform random noise perturbation centered around an average value ϕ_{avg}, or superposition of this random noise with an additional small perturbation imposing a periodic stripe-like structure. A summary of these initial conditions is presented in Table 3.1.

3.3.1 Evolution of Initially Planar Membranes

Systems initialized as flat membranes with random noise in the composition field (Case 1) will be discussed first. At early stages of the evolution, an initially planar height profile remains nearly flat while the composition changes to the thermodynamic equilibrium values as the mixture separates, forming small domains of minority phase in a matrix of majority phase (see Fig. 3.5). These small minority-phase domains then coarsen into larger ones, a process driven by the line-tension energy, reducing the total interfacial length. As larger domains form, the height profile responds to the changes in the composition field, and the domains then bulge inward or outward, depending on their spontaneous curvatures. The contour plots in Fig. 3.5 illustrate the correspondence between local composition and shape. The minority phase α (shown in red in all figures) has a positive spontaneous curvature while the majority phase β (shown in black in all figures) has a negative spontaneous curvature. The curvature effects are evident in the height plots, which show the minority phase bulging outward and the majority phase inward. It should be noted that, in some simulations, the average height slowly deviates from zero during evolution because the dynamics for the height is non-conserving. In these cases, the height values are shifted so that the average height remains at zero.

The process of domains bulging away from the initial membrane plane illustrates the competition among driving forces that governs the compositional and morphological evolution in these membrane systems. Domain bulging increases surface-tension energy, decreases line-tension energy, and could increase or decrease bending energy, depending on the curvature properties possessed by the phases. The bending energy is minimized when domains adopt their spontaneous curvatures; this is generally accomplished by each domain forming a shape resembling either a portion of a half-cylinder or a spherical cap, with a curvature trace equal to the local spontaneous curvature. However, to minimize line-tension energy, a circular domain (or spherical cap) is preferred over a long, cylindrical domain. This is illustrated in Fig. 3.5c at $t = 7.64 \times 10^{-3}$; after coarsening has occurred, minority-phase domains have long, partial-cylinder shapes. In the system in Fig. 3.5, the composition field eventually evolves to a state with a caplet morphology (*i.e.*, a single circular minority-phase domain), as the line-tension energy dominates the energetic competition. Thirty different Case 1 simulations were performed, each using a difference random seed in the initialization, and each of these systems evolved to a caplet morphology.

Systems initialized with a small stripe-like perturbation superimposed on random noise (Case 2) will now be discussed. These systems begin in a less random mixture than in Case 1, with the stripe structure visible in the composition plot (Fig. 3.6a at $t = 1.53 \times 10^{-6}$). Systems are simulated with random-noise amplitudes, A_{noise}, of 5.0×10^{-3}, 1.0×10^{-2}, and 5.0×10^{-2}, along with stripe perturbations of sinusoidal form with amplitude, A_{stripe}, of 5.0×10^{-5}, 5.0×10^{-4}, 5.0×10^{-3}, 1.0×10^{-2}, and 5.0×10^{-2}, with the wavelength equal to the simulation cell size. The system represented in Fig. 3.6 has $(A_{noise}, A_{stripe}) = (5.0 \times 10^{-2}, 5.0 \times 10^{-2})$. In this system, as phase separation occurs, domains of the minority phase form, which are initially small and isolated. However, the membrane shape has already responded to the initial compositional stripe perturbation, forming a ripple structure in the height profile (Fig. 3.6b, $t = 1.91 \times 10^{-3}$; 3.6c, $t = 6.11 \times 10^{3}$). To better visualize the height profile at $t = 1.91 \times 10^{-3}$, it is presented as a surface plot in Fig. 3.7a. We note that Fig. 3.7a shows four unit cells (two in each direction) for clarity. Figure 3.7b shows a contour plot of the curvature trace, also at $t = 1.91 \times 10^{-3}$. Once the small domains begin to coarsen, the largest domain oriented along the axis of the computational domain is able to grow and connect to itself, spanning the computational domain and forming a stripe structure (Fig. 3.6d at $t = 1.76 \times 10^{-2}$). The material in the remaining minority-phase domains apart from the largest domain diffuses to the largest stripe domain in order to reduce line-tension energy as well as surface-tension and bending energies. This creates the stable stripe structure shown in Fig. 3.6e at $t = 2.75 \times 10^{-1}$.

The stable stripe structure can be obtained when a sufficient amount of stripe perturbation is imposed on the initial composition field. We find that, regardless of the magnitude of the random noise in the chosen range, a sufficiently large amplitude of perturbation is required in order to create a stable stripe structure. This amplitude was found to be $A_{stripe} = 5.0 \times 10^{-2}$. However, stripes do not form deterministically

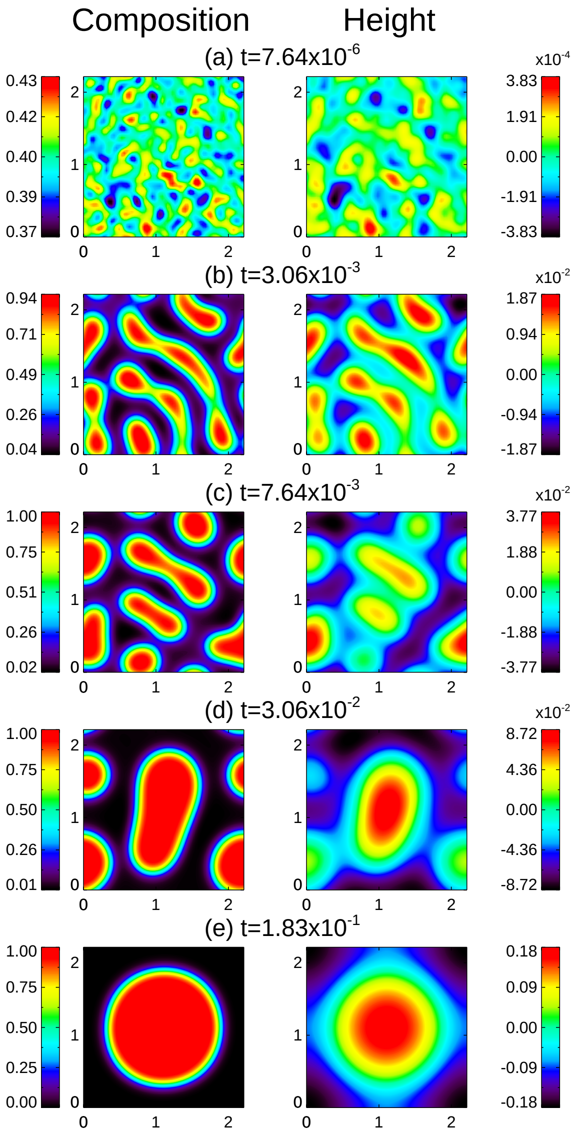

Figure 3.5: Contour plots representing the composition and corresponding height fields from a Case 1 simulation with $A_{noise} = 5.0 \times 10^{-2}$. From top to bottom, (a) $t = 7.64 \times 10^{-6}$, (b) $t = 3.06 \times 10^{-3}$, (c) $t = 7.64 \times 10^{-3}$, (d) $t = 3.06 \times 10^{-2}$, and (e) $t = 1.83 \times 10^{-1}$. Without any special perturbation imposed on composition or geometry ($A_{stripe} = A_{ripple} = 0$), all systems evolve similarly to this, forming a caplet morphology rather than stripes.

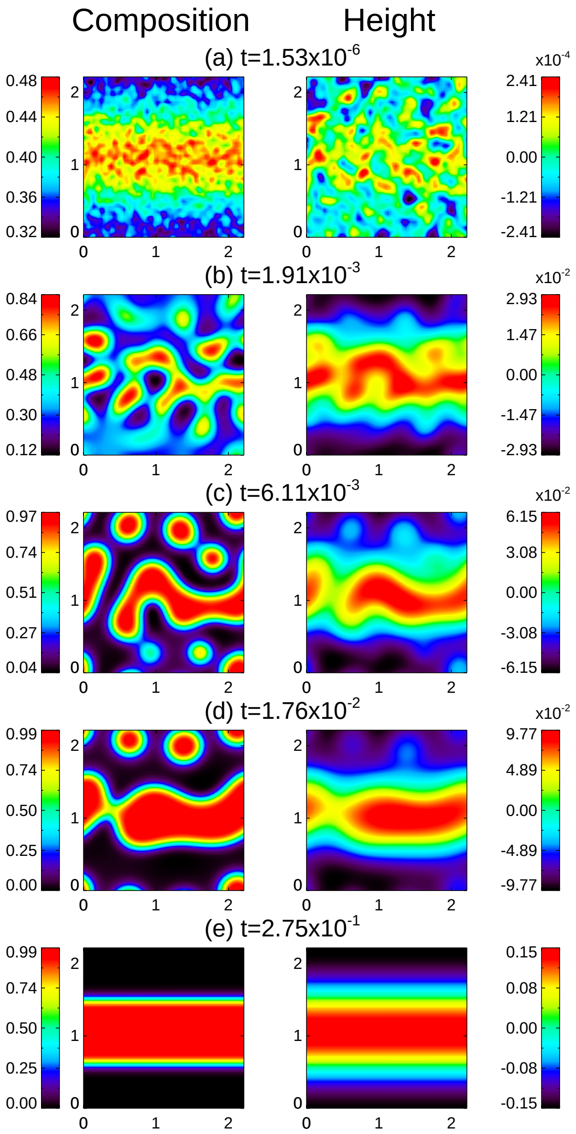

Figure 3.6: Contour plots representing the composition and corresponding height fields from a Case 2 simulation with $(A_{noise}, A_{stripe}) = (5.0 \times 10^{-2}, 5.0 \times 10^{-2})$. From top to bottom, (a) $t = 1.53 \times 10^{-6}$, (b) $t = 1.91 \times 10^{-3}$, (c) $t = 6.11 \times 10^{-3}$, (d) $t = 1.76 \times 10^{-2}$, and (e) $t = 2.75 \times 10^{-1}$. In this case, the perturbation $A_{stripe} = 5.0 \times 10^{-2}$ is sufficient to create a stable stripe morphology by $t = 2.75 \times 10^{-1}$.

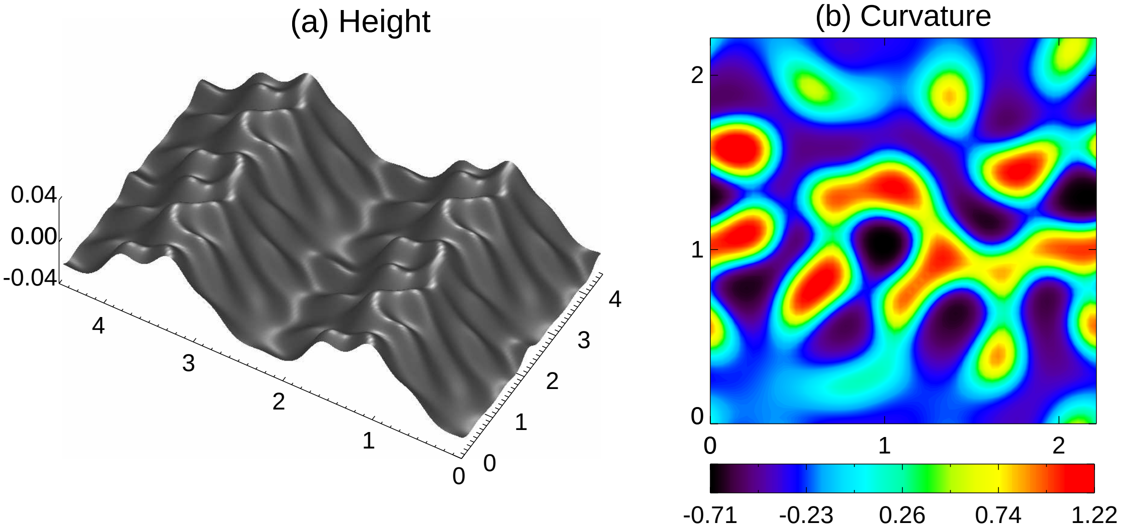

Figure 3.7: Surface plot representing membrane geometry (a) and contour plot representing the curvature trace (equal to twice the mean curvature) (b) from a Case 2 simulation with $(A_{noise}, A_{stripe}) = (5.0 \times 10^{-2}, 5.0 \times 10^{-2})$ at $t = 1.91 \times 10^{-3}$. Note that the surface plot shows four unit cells (two in each direction) for clarity. Compare with the contour plot of height in Fig. 3.6b, which presents the same data in two dimensions.

Table 3.2: Stationary-state morphologies observed for Case 1 and Case 2 simulations in terms of noise amplitude and stripe amplitude. Caplet and stripe morphologies are denoted by ‘c’ and ‘s’, respectively; numbers indicate how many different simulations, using different random seeds, formed the indicated morphology.

	A_{stripe}					
A_{noise}	0	5.0×10^{-5}	5.0×10^{-4}	5.0×10^{-3}	1.0×10^{-2}	5.0×10^{-2}
5.0×10^{-3}					c	s (x3)
1.0×10^{-2}						s (x3)
5.0×10^{-2}	c (x30)	c	c	c	c	s (x2), c (x1)

at this amplitude. Different sets of random numbers used to initialize composition occasionally result in very different evolution, as can be observed by comparing Fig. 3.6 and Fig. 3.8. Both of these cases are initialized with the same sinusoidal and random-noise amplitudes, although one evolves to stripes while the other evolves to a caplet morphology. The difference is evident in the fourth row of plots in each of the figures (Fig. 3.6d and Fig. 3.8d, at $t = 1.76 \times 10^{-2}$). As coarsening occurs in the system in Fig. 3.6, the largest minority-phase domain is able to connect with itself to span the computational domain. Once this connection has been made, a stripe structure begins to form, which becomes more stable with time. Contrastingly, in the system in Fig. 3.8, no domains make a connection spanning the entire width of the computational domain, and line-tension energy then drives the minority phase to form round, isolated domains that coarsen to a single caplet. While this illustrates the stochastic nature of the evolution of these systems, stripes do typically form in cases where $A_{stripe} \geq 5.0 \times 10^{-2}$. Table 3.2 tabulates which morphology was observed in all Case 1 and Case 2 simulations, including the results when multiple simulations initialized with different sets of random numbers were performed.

The above example indicates that a stripe structure is able to form only when a single minority-phase domain connects with itself across the simulation cell, as in Fig. 3.6. As a result of the periodicity we impose on the computational domain, this single connection is all that is necessary to cause the system to evolve into stripes.

(a) t=1.53x10^{-6}

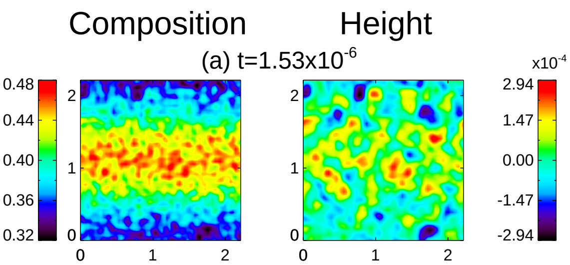

(b) t=1.91x10^{-3}

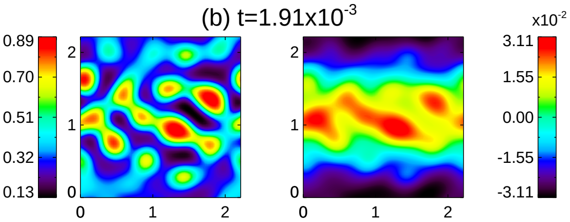

(c) t=6.11x10^{-3}

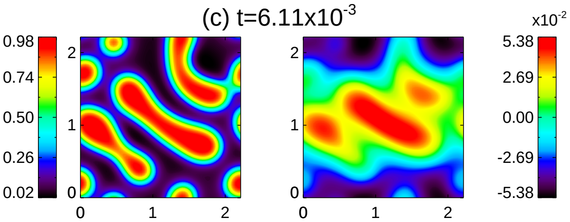

(d) t=1.76x10^{-2}

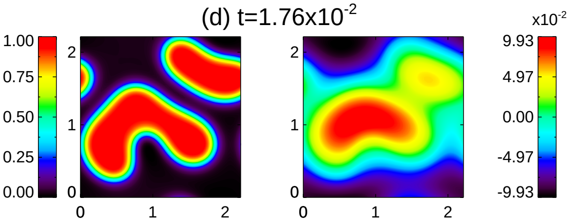

(e) t=2.75x10^{-1}

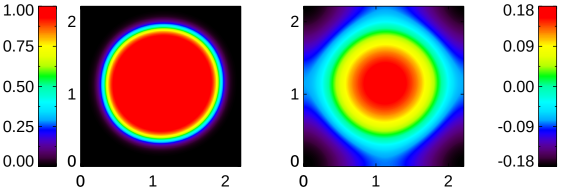

Figure 3.8: Contour plots representing the composition and corresponding height fields from a Case 2 simulation with $(A_{noise}, A_{stripe}) = (5.0 \times 10^{-2}, 5.0 \times 10^{-2})$. From top to bottom, (a) $t = 1.53 \times 10^{-6}$, (b) $t = 1.91 \times 10^{-3}$, (c) $t = 6.11 \times 10^{-3}$, (d) $t = 1.76 \times 10^{-2}$, and (e) $t = 2.75 \times 10^{-1}$. In this case, $A_{stripe} = 5.0 \times 10^{-2}$ is insufficient to create stable stripes, although Case 2 simulations with these parameters do typically create a stable stripe morphology (see Fig. 3.6). This is one example illustrating how the dynamics and final configurations of these systems are very sensitive to initial conditions.

However, in a physical system where there is no periodicity, such connections would need to form between all isolated domains in order for a similar stripe structure to form. Without an imposed periodicity, line-tension energy overcomes the tendency toward a stripe structure, and the minority phase is expected to form circular caplet domains, as in Fig. 3.8.

3.3.2 Evolution of Membranes with Initial Sinusoidal Height Perturbations

Systems initialized with a periodic sinusoidal, or ripple, structure imposed on the height profile (Case 3) will now be discussed. In these simulations, composition is initialized with $A_{noise} = 0$, 5.0×10^{-4}, 5.0×10^{-3}, or 5.0×10^{-2}, and $A_{stripe} = 0$ for all, while the height is initialized to a sinusoidal shape of amplitude $A_{ripple} = 5.0 \times 10^{-2}$, 1.0×10^{-1}, or 2.0×10^{-1}, with wavelength equal to the size of the simulation cell. In the case where composition is constant ($A_{noise} = 0$), the order parameter is initially set to $\phi_{avg} = 0.4$ everywhere (Fig. 3.9). In this constant composition case, even at very early times a stripe structure begins to form in the composition field, although the minimum and maximum values of the order parameter have changed only slightly from $\phi_{avg} = 0.4$. As the system phase separates and the order parameter approaches the equilibrium phase values, the system develops a stripe structure, with a different periodicity than the ripple that was imposed initially on the height profile (Fig. 3.9d at $t = 1.53 \times 10^{-2}$). Since the ripple perturbation in the initial height profile is not fixed in time, the height responds to changes in the composition field at later times during phase separation. While a stripe structure has formed in the system at $t = 1.53 \times 10^{-2}$, these stripes later merge with each other to form fewer, wider stripes in order to reduce the line-tension energy. The final configuration of the system we observe is a stripe structure, which still has a different periodicity than the structure initialized in the height. While this periodicity is higher in energy than the equilibrium state with the periodicity used for the height initialization, the driving force for stripes to coarsen is too small to push the system out of this relatively stable configuration, at least in the time scale of simulations we are able to perform.

The results from simulations using $A_{noise} \neq 0$ differ significantly from those using $A_{noise} = 0$. The ripple structure tends to remain in the height profile only until the composition order parameter approaches the equilibrium phase values as the system phase separates (Fig. 3.10c at $t = 3.82 \times 10^{-3}$). The random noise imposed in the composition determines roughly where domains of the two phases will form. Unlike in the $A_{noise} = 0$ case, the random noise causes the composition to initially deviate from the periodicity of the height profile, and compact minority-phase domains form in all regions of the membrane. The height profile then follows the evolving composition, losing all of the ripple structure it initially possessed. The system then evolves just as the Case 1 systems do, eventually forming a caplet morphology. In one Case 3 simulation, where $(A_{noise}, A_{ripple}) = (5.0 \times 10^{-3}, 2.0 \times 10^{-1})$, the evolution is similar to the $A_{noise} = 0$ simulation (Fig. 3.9). Since A_{noise} is small, the relatively large height perturbation is able to impose a stripe structure before the height begins to follow the phase separation, and therefore the stripe morphology forms. In general, however, if a ripple perturbation is imposed only as the initial condition, it is insufficient to drive the system to form a stable stripe morphological phase, unless the composition is nearly uniform. Table 3.3 tabulates which morphology was observed in all Case 3 simulations.

3.3.3 Evolution of Membranes Supported on Rigid Surfaces with a Sinusoidal Height Profile

Systems where the height is fixed with a periodic ripple structure throughout the entire evolution will now be discussed (Case 4). In these simulations, $A_{noise} = 0$, 5.0×10^{-2}, 1.0×10^{-1}, 2.0×10^{-1}, or 3.0×10^{-1}, and $A_{stripe} = 0$, while $A_{ripple} =$

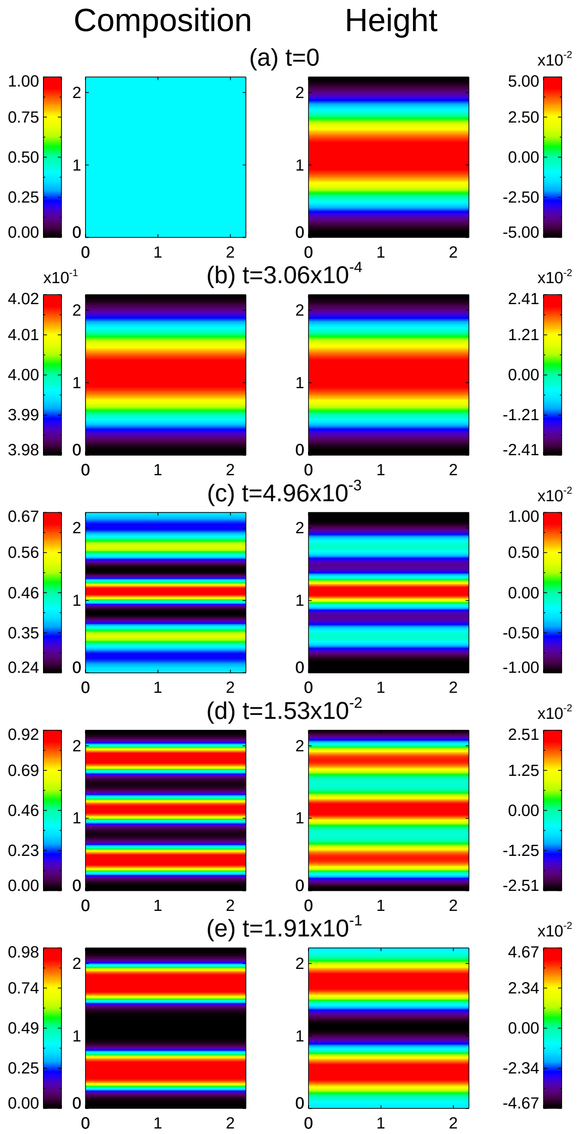

Figure 3.9: Contour plots representing the composition and corresponding height fields from a Case 3 simulation with $(A_{noise}, A_{ripple}) = (0, 5.0 \times 10^{-2})$. From top to bottom, (a) $t = 0$, (b) $t = 3.06 \times 10^{-4}$, (c) $t = 4.96 \times 10^{-3}$, (d) $t = 1.53 \times 10^{-2}$, and (e) $t = 1.91 \times 10^{-1}$. As the system phase separates, domains of the two phases form where their spontaneous curvatures are best satisfied. However, the height evolution follows the compositional evolution, and consequently the final stripe morphology we observe attains a different periodicity than the initial ripple.

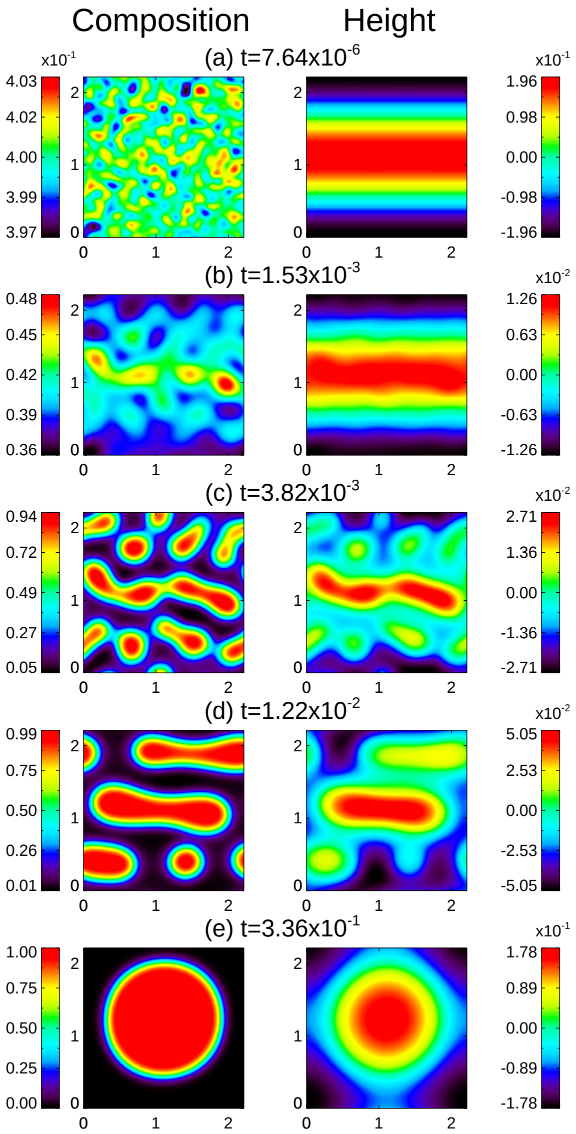

Figure 3.10: Contour plots representing the composition and corresponding height fields from a Case 3 simulation with $(A_{noise}, A_{ripple}) = (5.0 \times 10^{-3}, 2.0 \times 10^{-1})$. From top to bottom, (a) $t = 7.64 \times 10^{-6}$, (b) $t = 1.53 \times 10^{-3}$, (c) $t = 3.82 \times 10^{-3}$, (d) $t = 1.22 \times 10^{-2}$, and (e) $t = 3.36 \times 10^{-1}$. As the system phase separates, the ripple structure is disappearing (b-d, $t = 1.53 \times 10^{-3}$ - 1.22×10^{-2}) because the height evolution follows the compositional evolution that is dictated by the initial random noise. Therefore, no stripes form and the system evolves to a caplet morphology.

Table 3.3: Stationary-state morphologies observed for Case 3 simulations in terms of noise amplitude and ripple amplitude. Caplet and stripe morphologies are denoted by ‘c’ and ‘s’, respectively.

	A_{ripple}		
A_{noise}	5.0×10^{-2}	0.1	0.2
0	s		
5.0×10^{-4}		c	s
5.0×10^{-3}	c	c	c
5.0×10^{-2}	c	c	c

1.0×10^{-2}, 1.5×10^{-2}, 2.0×10^{-2}, 2.5×10^{-2}, 3.0×10^{-2}, 4.0×10^{-2}, 5.0×10^{-2}, or 6.0×10^{-2}. The $A_{noise} = 0$ simulation (Fig. 3.11) initially behaves very similarly to the Case 3 system with $A_{noise} = 0$ (Fig. 3.9). In both cases, minority-phase stripes form in the composition plot as the system phase separates, with a different periodicity than the initial ripple in the height profile. Very quickly, the stripes widen and merge to reduce line-tension energy. Finally, unlike the Case 3 $A_{noise} = 0$ simulation, the remaining stripes merge together to match the periodicity of the fixed ripple structure in the height profile. These $A_{noise} = 0$ Case 4 simulations evolved to stripes for the entire range of ripple amplitudes investigated.

In the cases where composition begins with random noise (Fig. 3.12, $(A_{noise}, A_{ripple}) = (5.0 \times 10^{-2}, 5.0 \times 10^{-2})$), the evolution resembles Fig. 3.6 where stable stripes form in Case 2 simulations. In both of these cases, the presence of a ripple in the height profile during phase separation causes single-phase domains to form in locations which best satisfy their spontaneous curvatures. This means that the domains conform to the ripple shape of the membrane, forming stripes in the composition profile. However, there is a threshold value of A_{ripple} for each amplitude of random noise, below which stripes do not form. The final stationary state that is reached in these cases is a single caplet domain within the periodic simulation box, positioned on the region of positive curvature of the fixed ripple structure. The results from all Case 4 simulations are presented in Table 3.4. The general trend is that membranes with a

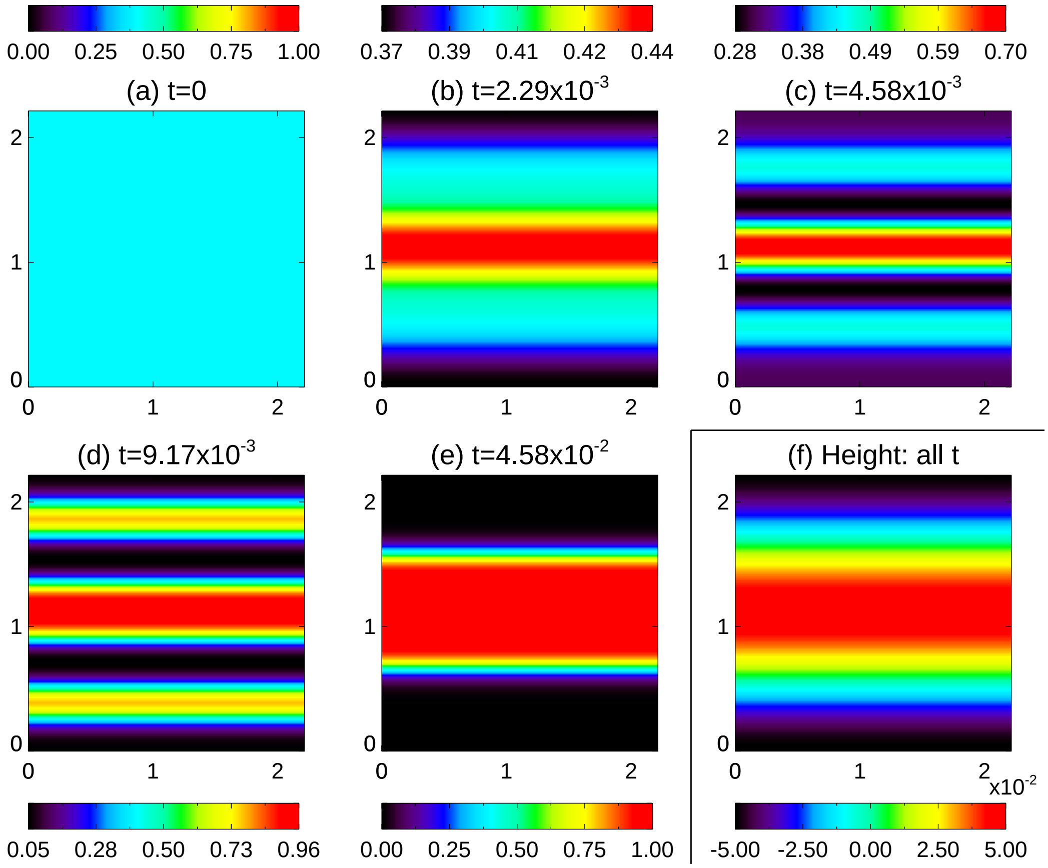

Figure 3.11: Contour plots representing composition and height fields for a Case 4 simulation, with $(A_{noise}, A_{ripple}) = (0, 5.0 \times 10^{-2})$. From top to bottom, left to right, composition at (a) $t = 0$, (b) $t = 2.29 \times 10^{-3}$, (c) $t = 4.58 \times 10^{-3}$, (d) $t = 9.17 \times 10^{-3}$, and (e) $t = 4.58 \times 10^{-2}$; (f) height at all t. The fixed ripple geometry, simulating a membrane on a rigid patterned surface, causes the two phases to form where their spontaneous curvatures are best satisfied, creating a stripe morphology.

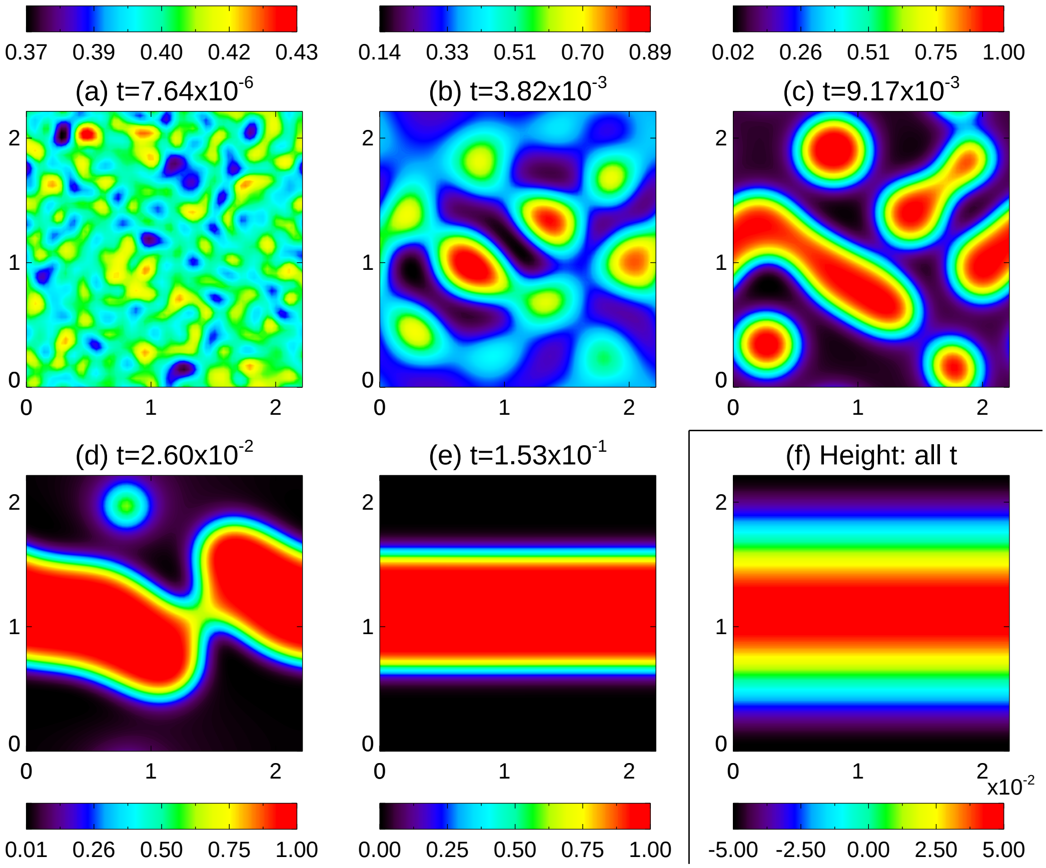

Figure 3.12: Contour plots representing composition and height fields for a Case 4 simulation with $(A_{noise}, A_{ripple}) = (5.0 \times 10^{-2}, 5.0 \times 10^{-2})$. From top to bottom, left to right, composition at (a) $t = 7.64 \times 10^{-6}$, (b) $t = 3.82 \times 10^{-3}$, (c) $t = 9.17 \times 10^{-3}$, (d) $t = 2.60 \times 10^{-2}$, and (e) $t = 1.53 \times 10^{-1}$, (f) height at all t. The fixed ripple geometry has amplitude above the threshold for stripes formation, and therefore the two phases form where their spontaneous curvatures are best satisfied, despite the initial compositional fluctuation.

higher amplitude of random noise in composition require a larger ripple amplitude to induce a stripe structure. Overall, a membrane initially having either a uniform composition or random mixture, resting on a surface that is fixed with a sufficiently large ripple amplitude will, after phase separation, conform its composition profile to match the height profile and form a stripe morphological phase. Thus, we find that topographical patterns with sufficiently large amplitude have a strong influence on the morphological evolution in these systems.

Table 3.4: Stationary-state morphologies observed for Case 4 simulations in terms of noise amplitude and fixed ripple amplitude. Caplet and stripe morphologies are denoted by ‘c’ and ‘s’, respectively.

	A_{ripple}							
A_{noise}	0.01	0.015	0.02	0.025	0.03	0.04	0.05	0.06
0	s						s	
0.05	c	s	s	s	s		s	
0.1	c	c	s	s	s	s	s	
0.2	c	c	s	s	s		s	s
0.3		c	c	s	s	s	s	

3.4 Conclusions

In this chapter, we examined phase separation in nearly planar lipid membranes using a coupled composition-deformation phase-field method. We focused on a system that has a stripe morphology as the lowest energy state. We found that, for the membrane system investigated, the final configuration (morphological phase) is highly sensitive to initial conditions. When there was no initial stripe-type or ripple-type perturbation, the stripe morphological phase was consistently not observed. In initially planar systems, we showed that stripes form only when an initial compositional perturbation with sufficiently large amplitude is imposed. Therefore, it is unlikely that a stripe structure would form spontaneously from a random lipid mixture on a flat background even if it is the lowest-energy morphology. Similarly, a sinusoidal ripple perturbation initially imposed on the height that is allowed to evolve is insufficient to induce stripes when random fluctuations in composition exist. Stripes formed in this case only when the composition was initially nearly uniform ($A_{noise} \approx 0$). Typically, as isolated single-phase domains form from the compositional random fluctuations, the height profile follows composition, and the ripple perturbation that had initially been imposed in the height dissipates. Although the lowest-energy morphology for the given parameter set is stripes, the dynamics of their formation have specific symmetry requirements that are rarely met in systems with random fluctuations.

Contrastingly, for a membrane with a rigid sinusoidal ripple structure of sufficiently large amplitude, stripes will form regardless of the initial conditions in composition. Thus, we find that rigid topographical surface patterns have a strong effect on the phase separation and compositional evolution in these systems. Experiments with supported multicomponent lipid bilayers have been performed on patterned surfaces, reporting that the phases can be sorted by the patterns to satisfy their bending energy (71, 190). One study found that a micropatterned surface with curved ridges could be used to sort liquid-ordered and liquid-disordered phases, where the liquid-ordered phase, which is more rigid, preferred to reside in areas of lower curvature (71). A second study used a surface with nanosmooth patches in an otherwise nanocorrugated background, finding that similarly, the liquid-ordered phase segregated to the nanosmooth parts of the surface (190). While both of these studies used symmetric bilayers with zero spontaneous curvature, they concluded that separated phases partitioned to particular regions of a patterned surface in order to best satisfy their bending energies, similar to the finding reported here.

CHAPTER IV

Spherical Vesicle Membrane Model

4.1 Introduction

As introduced in Sec. 1.2.1, lipid vesicles are often used as a model membrane system when studying lipid phase separation. Vesicles can be thought of as simple, empty cells, since the bilayer forms an approximately spherical shell that encapsulates an inner volume. In experiments, giant unilamellar vesicles (GUVs) are typically used (also known as giant liposomes), defined as vesicles with a diameter on the order of tens of microns, and consist of only one lipid bilayer (as opposed to multilamellar vesicles, which are essentially a system of multiple vesicles housed within each other). GUVs are a desirable model membrane system because they are relatively simple to create, are large enough to view using optical microscopy techniques, and are a good geometric approximation of the plasma membrane, being a curved, closed surface as opposed to supported or unsupported planar lipid membranes. In addition to GUVs created *in vitro* (starting from lipid solutions), giant plasma membrane vesicles (GPMVs) have also been used to study lipid behavior (42, 191). GPMVs are similar to GUVs, although they are made by inducing living cells to produce blebs, or budded-off vesicles from their plasma membranes. The GPMVs then have a lipid composition equivalent (or nearly equivalent) to that of the cell, while still lacking cytoskeletal components. GPMVs are a better representation of living cells than the laboratory-fabricated GUVs, typically composed of simple, ternary mixtures of lipids. To simulate vesicular systems, the model presented in Chapter III must be extended to accommodate the spherical background geometry of vesicles.

In this chapter, a model for unilamellar vesicles is presented, as an extension of the nearly planar membrane model from Chapter III to a spherical background geometry (192). This model is a closer representation of *in vivo* membranes since these membranes form a closed surface with an internal volume. This chapter will present the modifications made to the original nearly planar model to achieve this spherical extension, and will present results obtained with this vesicle model.

4.2 Methods: Extending the Nearly Planar Membrane Model to a Spherical Geometry

The first modification made to the nearly planar model is related to the volume within the closed vesicle surface, adding an additional term to the free energy:

$$F = \int H dA - PV = \int (H_0 + H_1 + H_2) dA - PV, \tag{4.1}$$

where P is the internal pressure of the vesicle and V is the internal volume. Since water molecules can pass through lipid membranes largely unhindered, while other larger and/or charged molecules cannot, osmotic effects can be used to alter the internal pressure of the vesicle. For example, if the solution inside the vesicle has a higher solute concentration than the solution outside the vesicle, water will flow into the vesicle in response to the osmotic gradient, increasing the internal pressure. In our model, P is an input parameter to which V responds to reduce the free energy. The expressions for H_0 and H_1 are unchanged, and are given by Eqs. 3.2 and 3.3, to model the free energy of the mixture and coupling composition with mechanical properties, respectively. However, the term H_2 for the surface-tension energy has been modified to implement a new area conservation scheme, as discussed in the next section.

4.2.1 Area Conservation

In the nearly planar model, the surface area was not explicitly conserved, but rather the system had an energetic penalty imposed if the surface area increased, scaled by the constant Lagrange multiplier σ. The changes in surface area in simulations using the nearly planar model were observed to be approximately $1\% - 4\%$, which was considered acceptable since the molecules in the membrane do have a small amount of leeway with regard to their separation distance. For the spherical case, however, using a similar scheme led to much larger changes in surface area, which were deemed unphysical. Therefore, a more sophisticated scheme was developed and implemented to conserve the surface area of the vesicle.

Area conservation is accomplished using two Lagrange multipliers, σ_α and σ_β, which are applied to the areas occupied by the α and β phases, respectively. This gives rise to additional terms, $\sigma_\alpha(A_\alpha - A_{\alpha,0}) + \sigma_\beta(A_\beta - A_{\beta,0})$, in the free energy, where A_α and A_β are the areas occupied by the α and β phases, respectively, and the subscript '0' denotes their initial values. Without loss of accuracy, the free energy can be shifted to eliminate the constant initial area terms, $\sigma_\alpha A_{\alpha,0}$ and $\sigma_\beta A_{\beta,0}$, leaving only $\sigma_\alpha A_\alpha + \sigma_\beta A_\beta$. Since $A_\alpha = \int \phi dA$ and $A_\beta = \int (1-\phi)dA$, the surface-tension energy term H_2 can be written as

$$
\begin{aligned}
H_2 &= \sigma_\alpha \phi + \sigma_\beta(1-\phi) && (4.2) \\
&= \sigma + \frac{\Delta\sigma}{2}(2\phi - 1), && (4.3)
\end{aligned}
$$

where we define $\sigma = (\sigma_\alpha + \sigma_\beta)/2$ and $\Delta\sigma = \sigma_\alpha - \sigma_\beta$. The Lagrange multipliers are uniform over the surface of the vesicle at any time, but are variable in time and are determined dynamically at each time step. While this causes the constant initial area terms that were eliminated from the free energy to vary in time, they are constant in space at each time step, and thus the dynamics are accurately modeled. The following scheme for calculating σ and $\Delta\sigma$ not only conserves the surface area of the vesicle, but also the area fractions of the α and β phases. In response to a normal deformation $\psi\hat{\mathbf{n}}$, the variation in total area and the variation in the difference in area between the two phases can be written as

$$\delta A = \int \psi\hat{\mathbf{n}} \cdot K\hat{\mathbf{n}} dA, \tag{4.4}$$

$$\delta(\Delta A) = \int (2\phi - 1)\psi\hat{\mathbf{n}} \cdot K\hat{\mathbf{n}} dA, \tag{4.5}$$

where $\Delta A = A_\alpha - A_\beta$, which will be referred to as the area difference. As in previous chapters, vector quantities are shown in bold, and unit vectors are denoted with hats.

The variation in the total free energy with respect to $\psi\hat{\mathbf{n}}$ can be written, with $H_m = H_0 + H_1$, as

$$\begin{aligned} \delta F &= \delta\Big(\int H_m dA - PV\Big) + \sigma\delta\int dA + \frac{\Delta\sigma}{2}\delta\int(2\phi - 1)dA & (4.6)\\ &= -\int \mathbf{f}_m \cdot \psi\hat{\mathbf{n}} dA + \sigma\int \psi\hat{\mathbf{n}} \cdot K\hat{\mathbf{n}} dA + \frac{\Delta\sigma}{2}\int(2\phi - 1)\psi\hat{\mathbf{n}} \cdot K\hat{\mathbf{n}} dA & (4.7)\\ &= -\int \mathbf{f} \cdot \psi\hat{\mathbf{n}} dA, & (4.8) \end{aligned}$$

where $\mathbf{f}_m$ is the force density (force per unit area) associated with mechanical and chemical energy, while the net force density $\mathbf{f}$ includes surface tension terms, *i.e.*, $\mathbf{f} = \mathbf{f}_m - K\sigma\hat{\mathbf{n}} - K(\Delta\sigma/2)(2\phi - 1)\hat{\mathbf{n}}$. In scalar form, these force densities can be written as

$$T_m = \mathbf{f}_m \cdot \hat{\mathbf{n}} = -(H_m K + Q(R - K^2) - \Delta Q - \zeta^2 K^{ab}\nabla_a\phi\nabla_b\phi - P), \tag{4.9}$$

$$T = \mathbf{f} \cdot \hat{\mathbf{n}} = T_m - K\sigma - \frac{K\Delta\sigma}{2}(2\phi - 1), \tag{4.10}$$

where Eq. 4.9 is very similar to Eq. 3.7 presented with the nearly planar membrane model, only with the surface tension terms absent and the addition of the pressure term.

We calculate σ and $\Delta\sigma$ specifying that the two variations in Eq. 4.4 and 4.5 be zero to conserve the total area and the area difference. To begin, we examine area changes that result from small deformations occurring during a single time step, $\psi = \partial_t \psi \delta t$, where $\partial_t \psi = \partial \psi / \partial t$. We can rewrite this expression for the deformation ψ using the relationship in Eq. 3.5 that relates the friction force density to the velocity $\partial_t \psi$, and substitute the net force density $\mathbf{f}$ since it is equal and opposite to the friction force density $\mathbf{f}_v$:

$$\begin{aligned} \partial_t \psi &= -\Gamma \mathbf{f}_v \cdot \hat{\mathbf{n}} = \Gamma \mathbf{f} \cdot \hat{\mathbf{n}}, && (4.11) \\ \psi &= \Gamma \delta t \mathbf{f} \cdot \hat{\mathbf{n}} = \Gamma \delta t T. && (4.12) \end{aligned}$$

Using this expression to substitute for the small deformation ψ in the area variations (Eqs. 4.4 and 4.5), we arrive at the following expressions:

$$\begin{aligned} \delta A &= \Gamma \delta t \int K T dA, && (4.13) \\ \delta(\Delta A) &= \Gamma \delta t \int (2\phi - 1) K T dA. && (4.14) \end{aligned}$$

Further, we can substitute in the expression for T from Eq. 4.10:

$$\begin{aligned} \delta A &= \Gamma \delta t \Big(\int K T_m dA - \sigma \int K^2 dA - \frac{\Delta\sigma}{2} \int K^2 (2\phi - 1) dA \Big), && (4.15) \\ \delta(\Delta A) &= \Gamma \delta t \Big(\int K T_m (2\phi - 1) dA - \sigma \int K^2 (2\phi - 1) dA && (4.16) \\ & \quad - \frac{\Delta\sigma}{2} \int K^2 (2\phi - 1)^2 dA \Big). \end{aligned}$$

Setting the two variations δA and $\delta(\Delta A)$ to zero in order to conserve total area and area difference, we obtain a set of linear equations, which can be solved to determine the instantaneous values of σ and $\Delta\sigma$:

$$\begin{pmatrix} \int K^2 dA & \int K^2(2\phi-1)dA \\ \int K^2(2\phi-1)dA & \int K^2(2\phi-1)^2 dA \end{pmatrix} \begin{pmatrix} \sigma \\ \frac{\Delta\sigma}{2} \end{pmatrix} = \begin{pmatrix} \int K T_m dA \\ \int K T_m (2\phi-1) dA \end{pmatrix}. \tag{4.17}$$

To implement these equations numerically, it is important to note that small numerical errors at any given time step cause the area and area difference to not identically equal the initial values, A_0 and ΔA_0, respectively. The multipliers σ and $\Delta\sigma$ are then chosen so as to compensate for these differences. Using Eqs. 4.15 and 4.16 with $\delta A = A(t+\Delta t) - A(t) = A_0 - A$, we obtain the following numerical scheme to determine the values of σ and $\Delta\sigma$ so that the numerical values of A and ΔA approximate A_0 and ΔA_0, respectively, with high accuracy:

$$\begin{pmatrix} \int K^2 dA & \int K^2(2\phi-1)dA \\ \int K^2(2\phi-1)dA & \int K^2(2\phi-1)^2 dA \end{pmatrix} \begin{pmatrix} \sigma \\ \frac{\Delta\sigma}{2} \end{pmatrix} = \begin{pmatrix} \int K T_m dA - \frac{1}{\Gamma\Delta t}(A_0 - A) \\ \int K T_m (2\phi-1) dA - \frac{1}{\Gamma\Delta t}[(A_{\alpha,0} - A_{\beta,0}) - (A_\alpha - A_\beta)] \end{pmatrix}. \tag{4.18}$$

4.2.2 Shape Evolution in Terms of a Radius

In the nearly planar model, the membrane surface was defined as a height at locations specified by (x, y) coordinates in a reference plane at $h = 0$. Similarly, the nearly spherical membrane surface here is defined as a single-valued radial distance function, $r(\theta, \xi)$. This function is written with respect to two angles of the spherical coordinate system defined in Fig. 4.1, where ξ is the azimuthal angle and θ is the polar angle. These angles are defined such that $\xi = 0$ at the positive x-axis, and $\theta = 0$

at $z = 0$ (*i.e.*, the equator) and takes positive values where $z < 0$. The reference geometry in this system is a sphere with a radius equal to the value of the local radial distance function. Figure 4.2 illustrates this radial distance function specifying the deformed surface in relation to the local reference surface patch, where the deformed surface is projected one-to-one onto the reference surface patch.

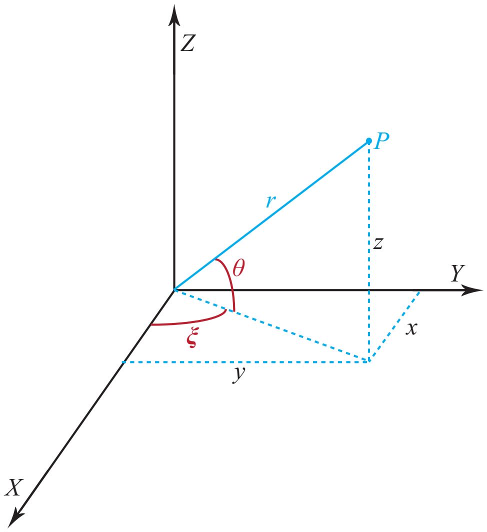

Figure 4.1: Definitions of the coordinates used for the spherical vesicle model, with azimuthal angle ξ and polar angle θ. The location P is expressed in terms of (r, θ, ξ), which can be expressed in Cartesian coordinates as the position vector $\mathbf{r}$ in Eq. 4.19. With the convention used, the θ coordinate for point P illustrated here has a negative value.

A point within the surface is described by its three-dimensional position vector:

$$\mathbf{r} = [r \cos\xi \cos\theta, r \sin\xi \cos\theta, -r \sin\theta]. \tag{4.19}$$

As in the previous chapter, we write vector components within square brackets. We use the indices $i = 1$ and 2 to refer to the θ and ξ coordinates, respectively. The derivatives of r with respect to the θ and ξ coordinates are defined as

$$r_1 = \frac{\partial r}{\partial \theta}, \quad r_2 = \frac{\partial r}{\partial \xi}. \tag{4.20}$$

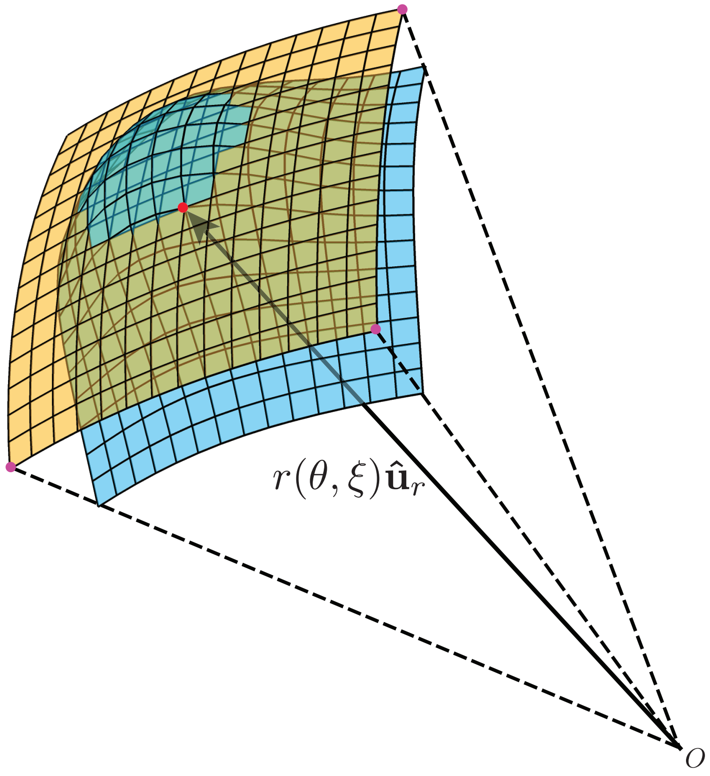

Figure 4.2: The membrane shape is described by a single-valued radial distance function $r(\theta, \xi)$. The figure shows the one-to-one projection of the deformed vesicle surface (blue grid) onto the local reference surface (orange grid), which is a spherical patch with radius $r(\theta, \xi)$ corresponding to the radius at the center point marked in red. $\hat{\mathbf{u}}_r$ is a unit vector in the radial direction.

Vectors tangent to the deformed surface can then be defined as

$$\begin{aligned}
\mathbf{e}_1 = \frac{\partial \mathbf{r}}{\partial \theta} &= [-r\cos\xi\sin\theta + r_1\cos\xi\cos\theta, -r\sin\xi\sin\theta + r_1\sin\xi\cos\theta, \qquad (4.21)\\
&\quad -r\cos\theta - r_1\sin\theta],\\
\mathbf{e}_2 = \frac{\partial \mathbf{r}}{\partial \xi} &= [-r\sin\xi\cos\theta + r_2\cos\xi\cos\theta, r\cos\xi\cos\theta + r_2\sin\xi\cos\theta, \qquad (4.22)\\
&\quad -r_2\sin\theta].
\end{aligned}$$

As discussed in Chapter III, the dynamical equation for the deformation is given by

$$\frac{\partial \psi}{\partial t} = \Gamma T, \tag{4.23}$$

and the conversion into the rate of change in radius, $\partial r/\partial t$, is performed as follows. An illustration defining the vectors in this discussion is presented in Fig. 4.3. We define a unit vector in the r direction as $\hat{\mathbf{u}}_r = \partial \mathbf{r}/\partial r = [\cos\xi\cos\theta, \sin\xi\cos\theta, -\sin\theta]$, so that the deformed surface is specified by $r\hat{\mathbf{u}}_r$ at a coordinate (θ, ξ). For a deformation of $\psi\hat{\mathbf{n}}$ in the radius, the radius changes from $r\hat{\mathbf{u}}_r$ to $(r+\Delta r)\hat{\mathbf{u}}_r$. If the unit vector normal to the deformed surface, $\hat{\mathbf{n}}$, is not parallel to $\hat{\mathbf{u}}_r$, then the projection of $\Delta r\hat{\mathbf{u}}_r$ along the membrane surface lies along a unit vector $\hat{\mathbf{t}}$ tangent to the deformed surface such that $\hat{\mathbf{u}}_r = (\hat{\mathbf{u}}_r \cdot \hat{\mathbf{t}})\hat{\mathbf{t}} + (\hat{\mathbf{u}}_r \cdot \hat{\mathbf{n}})\hat{\mathbf{n}}$. Using this unit vector $\hat{\mathbf{t}}$, the general radial change $\Delta r\hat{\mathbf{u}}_r$ can be written as $\Delta r\hat{\mathbf{u}}_r = \psi\hat{\mathbf{n}} + s\hat{\mathbf{t}}$. If we take the dot product of both sides of this equation with the unit normal to the deformed surface $\hat{\mathbf{n}}$, we arrive at

$$\Delta r(\hat{\mathbf{u}}_r \cdot \hat{\mathbf{n}}) = \psi, \tag{4.24}$$

$$\Delta r = \frac{\psi}{\hat{\mathbf{u}}_r \cdot \hat{\mathbf{n}}}. \tag{4.25}$$

We now rewrite the unit vectors $\hat{\mathbf{u}}_r$ and $\hat{\mathbf{n}}$ using the metrics of the deformed and reference surfaces, $\sqrt{g}$ and $\sqrt{g^0}$, respectively. The deformed surface metric (as in Appendix A) is given by the determinant of the metric tensor g_{ij}, and the reference

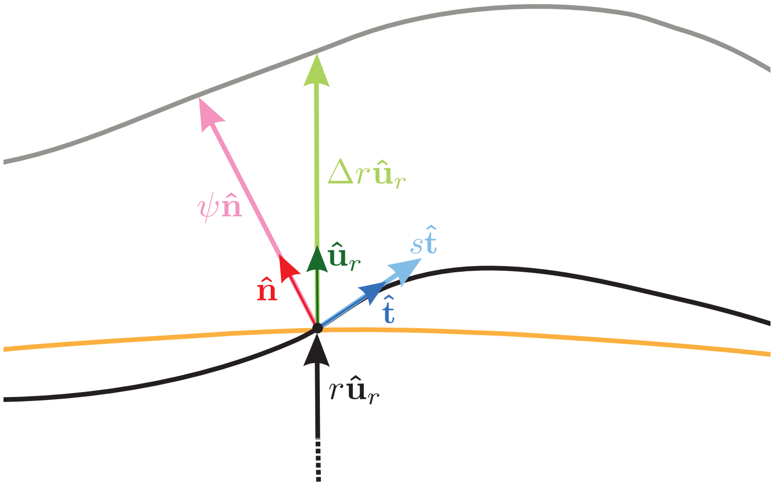

Figure 4.3: Illustration of the vectors involved in the conversion from deformation ψ to a change in radius Δr. The reference surface is shown in orange, the current deformed surface in black, and the future deformed surface in gray. The black vector $r\hat{\mathbf{u}}_r$ is drawn from the origin (not shown), and all other vectors are drawn from the grid point on the current surface. The unit vectors $\hat{\mathbf{u}}_r$, $\hat{\mathbf{n}}$, and $\hat{\mathbf{t}}$ lie in the radial direction, normal to the deformed surface, and tangent to the deformed surface, respectively. The radial change vector, $\Delta r\hat{\mathbf{u}}_r$, can be expressed in terms of the normal deformation vector, $\psi\hat{\mathbf{n}}$, and a scaled version of the tangent vector, $s\hat{\mathbf{t}}$.

surface metric is this same expression with a constant radius equal to the local radius:

$$\begin{aligned}\sqrt{g} &= r(r^2\cos^2\theta + r_1^2\cos^2\theta + r_2^2)^{1/2}, \quad (4.26)\\ \sqrt{g^0} &= r^2\cos\theta. \quad (4.27)\end{aligned}$$

These metrics can be related to the unit vectors $\hat{\mathbf{u}}_r$ and $\hat{\mathbf{n}}$ using the tangent vectors to the surfaces (basis pairs), where $\mathbf{e}_i^0$ is the projection of $\mathbf{e}_i$ onto the reference surface patch:

$$\begin{aligned}\sqrt{g}\hat{\mathbf{n}} &= \mathbf{e}_1 \times \mathbf{e}_2, \quad (4.28)\\ \sqrt{g^0}\hat{\mathbf{u}}_r &= \mathbf{e}_1^0 \times \mathbf{e}_2^0. \quad (4.29)\end{aligned}$$

By taking the dot product of these two vectors, $\sqrt{g^0}\hat{\mathbf{u}}_r \cdot \sqrt{g}\hat{\mathbf{n}} = (\mathbf{e}_1^0 \times \mathbf{e}_2^0)\cdot(\mathbf{e}_1 \times \mathbf{e}_2)$, we find that this expression reduces simply to g^0 by the properties of dot and cross products. Finally, we rearrange and make substitutions to relate the radial evolution to the velocity of the deformation:

$$\sqrt{g^0}\hat{\mathbf{u}}_r \cdot \sqrt{g}\hat{\mathbf{n}} = g^0, \quad (4.30)$$

$$\hat{\mathbf{u}}_r \cdot \hat{\mathbf{n}} = \frac{\sqrt{g^0}}{\sqrt{g}}, \quad (4.31)$$

$$\Delta r = \frac{\psi}{\hat{\mathbf{u}}_r \cdot \hat{\mathbf{n}}} = \frac{\sqrt{g}}{\sqrt{g^0}}\psi, \quad (4.32)$$

$$\frac{\partial r}{\partial t} = \frac{\sqrt{g}}{\sqrt{g^0}}\frac{\partial \psi}{\partial t}. \quad (4.33)$$

4.2.3 Numerical Methods

4.2.3.1 Yin-Yang Grid System

To solve the governing equations above, a discretization of the angular space is required. For the nearly planar model, grid points were defined as a simple orthogonal grid in Cartesian space. However, for the spherical geometry in this vesicle model, defining these grid points is a more complex problem. In standard spherical coordinates, a longitude-latitude system of mesh points is an intuitive way to place a grid on a spherical surface; however, this system has features that can create non-physical artifacts in numerical calculations. One such feature is the large amount of variability in the size of the grid cells (or distances between adjacent mesh points) when comparing mesh points at the equator to those near the poles. Ideally, all grid cells would be identical in size so that the surface is uniformly resolved. A second such feature is the convergence of the longitudinal lines at the poles of the sphere. Using the finite difference method, derivatives of functions are calculated at a specified location in terms of their values at neighboring points. However, the points at the poles of the sphere have a large (arbitrary) number of neighboring points, and would need to be treated specially to calculate derivatives.

In order to avoid both of these disadvantages, we have implemented the Yin-Yang grid system developed by Kageyama and Soto for computational geoscience studies (193). The Yin-Yang grid system uses two identical grids to cover the spherical surface, as illustrated in Fig. 4.4. Each grid covers the middle range of latitude and wraps around three-quarters of the equator of the sphere, covering the coordinate ranges of $\xi = [-3\pi/4, 3\pi/4]$ in the azimuthal angle and $\theta = [-\pi/2, \pi/2]$ in the polar angle (with $\theta = 0$ at the equator). By covering only this portion of the sphere, the variation in the size of the grid cells is minimal and the polar points are eliminated. The two grids are used to cover the spherical surface by rotating one of them using the following transformation, which can be written simply as

$$\begin{aligned} x' &= -x \qquad (4.34) \\ y' &= -z \\ z' &= -y. \end{aligned}$$

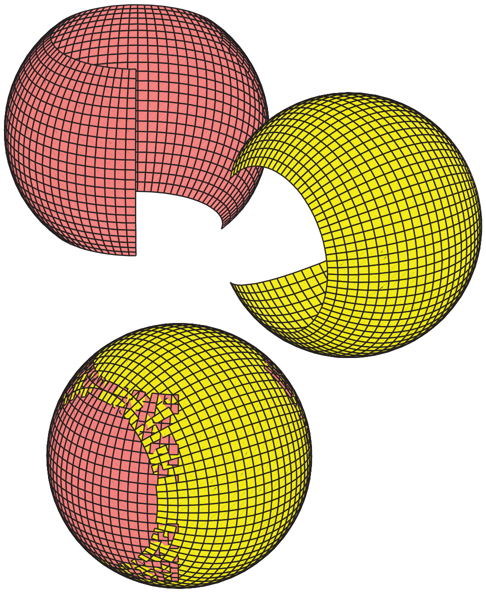

Figure 4.4: The Yin and Yang grids used to discretize the angular space, separated (top) and combined (bottom). The two grids are identical, and cover the spherical surface with minimal overlap.

Using this transformation, the grids cover the entire surface with a small amount of overlap and with boundaries similar to the locations of the seams on a tennis ball.

Calculations are performed separately in each grid within their local coordinate systems. In order to have the two grids together create a single, coherent surface, they must communicate at each time step in the simulations to account for overlapping regions. All overlapping regions are considered to have "real" data in one grid, occupying "primary zones," while in the other grid they are considered as "ghost zones." The locations of these ghost zones are shown schematically in Fig. 4.5, representative of a flattened version of either the Yin or Yang grid. The regions marked in green are determined to be in the ghost zone based solely on their θ coordinate, since these ghost zones are simply defined as boundary points. The regions marked in blue are more complex, since their boundary is curved with respect to the grid lines, and so points are determined to be in these ghost zones if they are outside of the semicircle traced by $\vec{r}_{ghost}$ originating from the point O_{ghost} nearest to them.

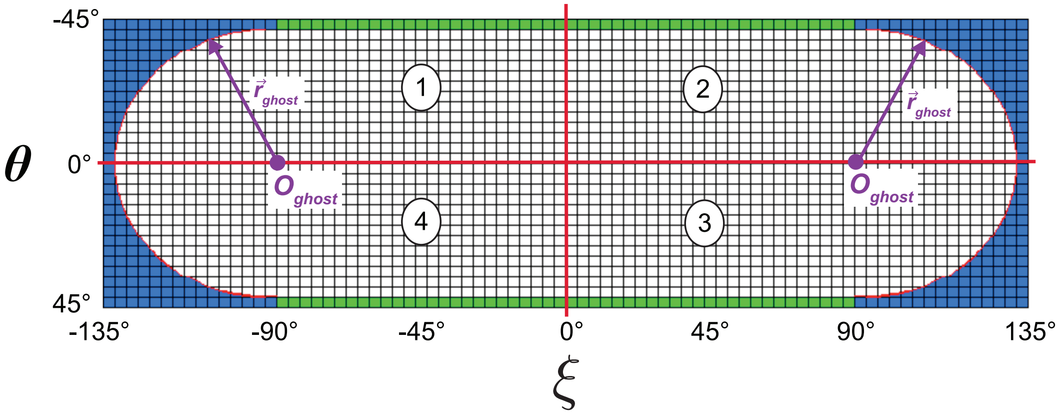

Figure 4.5: The unrolled view of one of the Yin-Yang grids is shown, with the four quadrants separated by red lines and labeled $1-4$. The ghost-zone regions, where the two grids overlap and the primary data is contained in the other grid, are colored in green and blue, while the primary zone is not colored. The green regions are defined by their θ coordinate, while the blue regions are defined by the semicircle traced by the vectors $\vec{r}_{ghost}$ originating from the points O_{ghost}.

Ghost-zone points need to have data copied onto them from primary-zone points on the other grid because they are used for calculating derivatives at primary-zone points that are located near ghost zone boundaries. However, since the points from the two grids are not perfectly coincident in overlapping regions, an interpolation scheme is implemented using a second-order Taylor series approximation to calculate the value of a ghost-zone point from values in the primary zone of the other grid as shown in Fig. 4.6:

$$\begin{aligned} W_{Yin}(\theta+a,\xi+b) &= W_{Yang}(\theta,\xi)+a\frac{\partial W_{Yang}}{\partial\theta}\bigg|_{(\theta,\xi)}+b\frac{\partial W_{Yang}}{\partial\xi}\bigg|_{(\theta,\xi)} \qquad (4.35)\\ &+ a^2\frac{\partial^2 W_{Yang}}{\partial\theta^2}\bigg|_{(\theta,\xi)}+b^2\frac{\partial^2 W_{Yang}}{\partial\xi^2}\bigg|_{(\theta,\xi)}+ab\frac{\partial^2 W_{Yang}}{\partial\theta\partial\xi}\bigg|_{(\theta,\xi)}, \end{aligned}$$

where W represents either the composition ϕ or the radius r, and is labeled for interpolating in the Yin ghost zones from Yang primary-zone points.

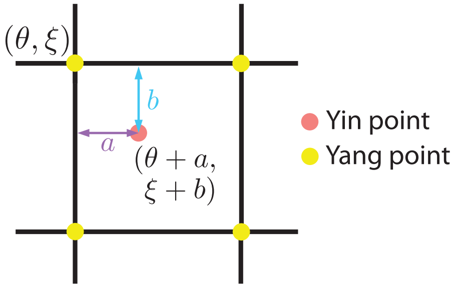

Figure 4.6: Illustration of interpolation for a ghost-zone point in the Yin grid from primary-zone points in the Yang grid. Interpolation must be performed since the points in the grids do not coincide perfectly in overlap regions. The interpolation for the Yin grid ghost-zone point (pink) at $(\theta+a,\xi+b)$ is done using Eq. 4.35 with the value of the nearest Yang point (yellow), marked (θ,ξ), and the offset distances a and b.

The calculation to determine the locations of the four nearest-neighbor points in the other grid is accomplished as follows (note that this calculation needs to only be performed once and can be done on the angular grid (θ,ξ)). For each mesh point in the Yin grid located in a ghost zone, its coordinates (specified in terms of the Yin grid angles, (θ,ξ)) are converted into Cartesian coordinates (x,y,z) using the components of the three-dimensional position vector in Eq. 4.19. Then, these Yin coordinates are converted to the Cartesian coordinates of the Yang grid, (x',y',z'), using the expressions in Eq. 4.34, and finally to the spherical coordinate angles on the Yang grid, (θ',ξ'), using

$$\theta' = \arcsin\left(\frac{-z'}{r}\right), \tag{4.36}$$

$$\xi' = \arccos\left(\frac{x'}{r\cos\theta'}\right)\mathrm{sgn}(y'), \tag{4.37}$$

where $\mathrm{sgn}(y')$ has the sign of y' and magnitude of unity.

Now the ghost-zone point in the Yin grid has its location specified in terms of the spherical angles in the Yang grid, and the nearest-neighbor points can then easily be found by rounding the coordinate values to those closest that are occupied by Yang grid points. The offset distances between the Yin grid point and the nearest-neighbor Yang grid points are then calculated.

4.2.3.2 Area Integral Calculations

In order to calculate the surface area of the deformed vesicle, or to calculate integrals taken with respect to the deformed vesicle surface, care needs to be taken in the overlapping ghost-zone regions of the Yin and Yang grids to ensure that no area is double-counted or neglected. This is done by summing over all of the grid cells the integrand (which is equal to unity for the surface area calculation) multiplied by the metric factor and the weighting factor, which is 1 for cells completely within the primary zone, 0 for cells completely within ghost zones, and a value between 0 and 1 for cells located partially within a ghost zone. In order to calculate the weighting factor, each grid cell needs to be placed into one of these three categories. A grid cell at a point (i, j) is defined to span $[i-1/2, i+1/2]$ and $[j-1/2, j+1/2]$, as shown in Fig. 4.7. Working with grid cells rather than points makes the determination of whether a grid cell lies inside, outside, or on top of the ghost-zone border more complex than in the case of interpolation in the previous section since a grid point may not lie within a ghost zone, while part of its grid cell does.

Similar to the setup for the interpolation calculations, the regions shown in blue and green in Fig. 4.5 are treated differently, since the green regions are defined simply by their θ coordinate, while the blue regions need more special treatment because their boundaries do not generally coincide with grid cells boundaries. Each Yin and Yang grid is split into four quadrants, divided by the lines $\theta = 0$ and $\xi = 0$. While the following algorithm is the same for each quadrant, the signs differ in each one. For this discussion, the quadrant with positive θ and ξ will be described. For each grid point in the blue region in this quadrant, (i, j), the corner of its cell at $(i+1/2, j+1/2)$

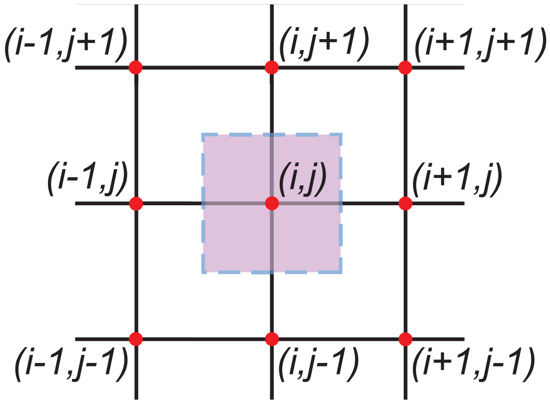

Figure 4.7: The grid cell corresponding to the point (i, j) is defined to span the intervals $[i-1/2, i+1/2]$ and $[j-1/2, j+1/2]$, as shown shaded in purple.

is further away from the origin O_{ghost} than the corner of its cell at $(i-1/2, j-1/2)$, and thus these locations are referred to as the far corner and near corner, respectively. The grid point is determined to require a weight of 1 if the distance between the origin O_{ghost} and both the near and far corners is less than $|\vec{r}_{ghost}|$, since that indicates it is located entirely inside the primary zone. Similarly, the grid point requires a weight of 0 if the distance between the origin O_{ghost} and both the near and far corners is greater than $|\vec{r}_{ghost}|$, indicating that it is located entirely inside the ghost zone. If the distance between the origin O_{ghost} and the far corner is greater than $|\vec{r}_{ghost}|$, but the distance between the origin O_{ghost} and the near corner is less than $|\vec{r}_{ghost}|$, this indicates the grid cell is straddling the ghost-zone boundary and requires a weight somewhere between 0 and 1 to account for only its partial area inside the primary zone. One very important piece of this calculation is that the distances calculated between these points are not in a Euclidean geometry, but rather follow the surface of the sphere. This means that the simple distance formula cannot be used, but rather the spherical distance formula taken from the field of spherical trigonometry, where the distance d between points $\mathbf{P}$ and $\mathbf{Q}$ on a sphere is given by

$$d = \arccos(\mathbf{P} \cdot \mathbf{Q}). \tag{4.38}$$

For the points requiring a weight between 0 and 1, the curve forming the boundary of the ghost zone will intersect with exactly two of the four edges of the cell. An α intersection point is defined as one with the $j-1/2$ cell edge, a β intersection point is defined as one with the $i-1/2$ edge, a γ intersection point with the $j+1/2$ edge, and a δ intersection point with the $i+1/2$ edge. Again, for any boundary cell, exactly two of these points will exist. By determining which two types of points exist, the cell can be placed into one of four configuration categories specifying the geometry of the area within the cell inside the primary zone, and the coordinates of the intersection points are determined. The configuration categories are shown in Fig. 4.8 for each of the four quadrants. The partial area in the cells is calculated based on the intersection points and geometry, assuming that the curved boundary can be approximated by a line connecting the two intersection points. Specifically, the area inside the primary zone in configuration A can be calculated as a trapezoid and rectangle; for configurations B and C, a triangle and rectangle; and for configuration D, simply a triangle. This area divided by the area of the square cell is the weight used for that cell. (Here, we have not included the effect of the curvature of the surface because this is accounted for in the metric factor in the numerical integration.) With this scheme the surface area can be calculated to within a 0.2% error.

4.2.4 Interfacial Length Calculations

One measure that we use to analyze the evolution observed in our vesicle simulations is the total interfacial length. Since $p'(\phi) = 0$ in the bulk phases and $p'(\phi) = 1$ in interfacial regions (note that $p(\phi)$ appears in the bending energy, Eq. 3.3), the total interfacial length at a given time, L, is proportional to $\tilde{L} = \int p'(\phi) dA$. To determine the proportionality, $\tilde{L}$ was calculated for a number of vesicles (simulated using different parameters) in their stationary states. Once in a stationary state, the vesicles used for this measurement have a single cap of each phase, forming hemi-

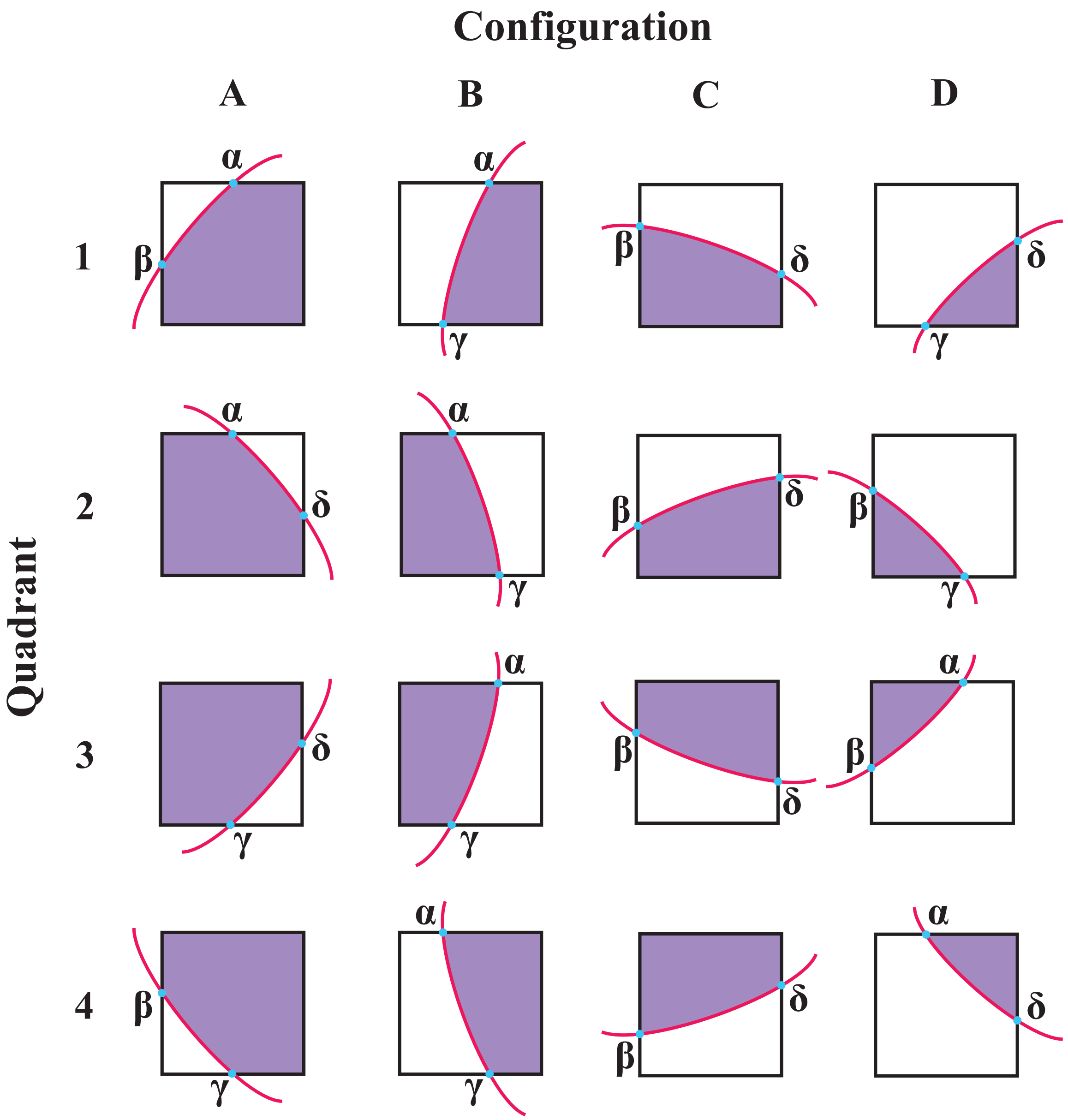

Figure 4.8: All of the possible configurations in each of the four quadrants for how the ghost-zone boundary could intersect with a grid cell straddling the boundary. The quadrant numbers are defined in Fig. 4.5. In each configuration, there are exactly two intersection points, labeled as α, β, γ, and δ, depending on which edge of the cell they lie on. Given the quadrant and configuration, the weight for the cell can be determined geometrically as the fraction of the cell within the primary zone, as shaded in purple.

spheres for an equal mixture, and differently sized caps for unequal mixtures. This configuration allows for a simple geometric calculation of the interfacial length, since there is a single interface with a length that can be calculated as the circumference from the radius where it is located. A linear relationship was established between L and $\tilde{L}$, and the proportionaility factor determined is used for all interfacial length calculations presented. The approach was found to be accurate to approximately 3% by plotting $\tilde{L}$ vs. L for 8 cases.

4.2.5 Simulation Parameters and Initializations

While some parameters are varied from one simulation to another in order to examine their effects on evolution, the following set of parameters are specified to have the same value in all simulations: $\Lambda_\alpha = 1$, $C_\alpha = 1$, $w = 86$, $\zeta = 0.458$, $M = 1$, $\Gamma = 0.05$, and $P = 5$. The parameters $\Lambda_\alpha = 1$ and the inverse of $C_\alpha = 1$ set the energy and length scales of the system, respectively, and all other quantities are measured with respect to these and are thus dimensionless in the model. Each Yin and Yang grid consists of 270 grid points in ξ and 90 grid points in θ. The shape is initialized as a perfect sphere (unless otherwise specified) with a radius of 3, which has a curvature trace of $K = 2/3$ (note that a sphere with a radius of 2 would minimize the bending energy for the α phase with $C_\alpha = 1$). The composition is initialized with a small amplitude of uniform random noise centered around the phase fraction, ϕ_{avg}. The parameters w and ζ are selected to satisfy two constraints: (i) since they determine the width of the diffuse interfaces, they are chosen such that a minimum of 6 grid points resolve the interfaces, and (ii) as a result of the bending energy term, the minima of the double-well potential in Eq. (3.2) can shift, and w and ζ are specified to set the line tension to be large enough such that this shift is no more than 2%. The friction coefficient and pressure are selected such that the vesicle is slightly inflated in order to remain overall convex, as the model cannot simulate extreme shape changes such as during a budding process.

4.3 Results and Discussion

In this investigation, the particular effects of spontaneous curvature, phase fraction, and bending rigidity are studied in approximately spherical vesicles. In each of the following sections, two of these parameters will be fixed across simulations while the other is varied. Additionally, the effects of phase fraction are studied in vesicle systems initialized with an elongated, non-spherical shape.

4.3.1 Varying Spontaneous Curvature in Equal Mixtures

The systems discussed in this section have equal mixtures of the two phases ($\phi_{avg} = 0.5$), $r = 3$, and equal bending rigidities $\Lambda_\alpha = \Lambda_\beta = 1$. The spontaneous curvature of the α phase is $C_\alpha = 1$ as in all cases in this chapter, while the spontaneous curvature of the β phase, C_β, is varied to isolate the effects of differences between the spontaneous curvatures of the α phase, the β phase, and the curvature of the vesicle surface. Simulation results are presented for systems with $C_\beta = -1, 0.5, 1, 2$, and 3, in addition to a control case where the bending energy is not included and the shape is a fixed, rigid sphere. This control case is referred to as the "no shape change" case, since there is no coupling between the phases and any mechanical shape effects.

Figure 4.9 presents plots of interfacial length vs. time as well as snapshots from systems with $C_\beta = -1, 2$, and 3. In all of these cases, the α phase has a spontaneous curvature closer to the curvature of the undeformed vesicle ($K = 2/3$) than does the β phase. As a result, the α phase behaves like a majority phase, forming a continuous domain structure around isolated β phase domains, even while being present at a phase fraction of 50%. From the interfacial length plots, it is clear that the case with $C_\beta = 3$ takes significantly longer to reach a stationary state than the other two cases. This is because the β phase domains prefer to have such a high curvature that smaller domains are favored over larger domains with respect to bending energy, and also because the β phase domains tend to bulge away from the surface more than when $C_\beta = 2$ or -1. For the $C_\beta = -1$ case, while the bending energy alone would produce β phase domains that would curve inward, the internal pressure and conserved surface area of the vesicle largely prevent this from occurring, except for in regions nearby interfaces. Figure 4.10 presents snapshots at the same time as t_1 in Fig. 4.9 plotting the curvature trace. The plot for the case with $C_\beta = -1$ shows the β phase domains having a negative curvature near the interfaces, though these negative curvature regions are compensated for with high curvature areas in the centers of the β phase domain from the internal pressure. Only when a β phase domain becomes small enough such that the negative curvature ring covers the entire domain area does it bulge inward. This occurs slightly later than time t_2 in Fig. 4.9, as can be observed in Fig. 4.11 showing a cross-section illustrating the negative, inward curvature of small β phase domains.

The jogs in the interfacial length curves in Fig. 4.9 indicate events where a domain disappears either by diffusion or by coalescing with another domain, and while the curves for the $C_\beta = -1$ and 2 cases appear similar at earlier times, coarsening proceeds more quickly with $C_\beta = 2$. This is because, of the three systems presented, the β phase in the $C_\beta = 2$ system has a spontaneous curvature that is closest to the spontaneous curvature of the α phase, and therefore the bending energy plays less of a role in the dynamics of this system than it does in the other two presented here. The plot of curvature for $C_\beta = 2$ in Fig. 4.10 has the smallest range of curvatures, and has a positive curvature everywhere, whereas for the $C_\beta = 3$ case, the β domain bulges outward with a higher curvature, and the extreme positive curvature just inside the β phase domains actually imposes a slight negative curvature on the other side of the interface in the α phase, slowing coarsening by forming barriers to domain coalescence.

In contrast, Fig. 4.12 presents interfacial length vs. time as well as snapshots from

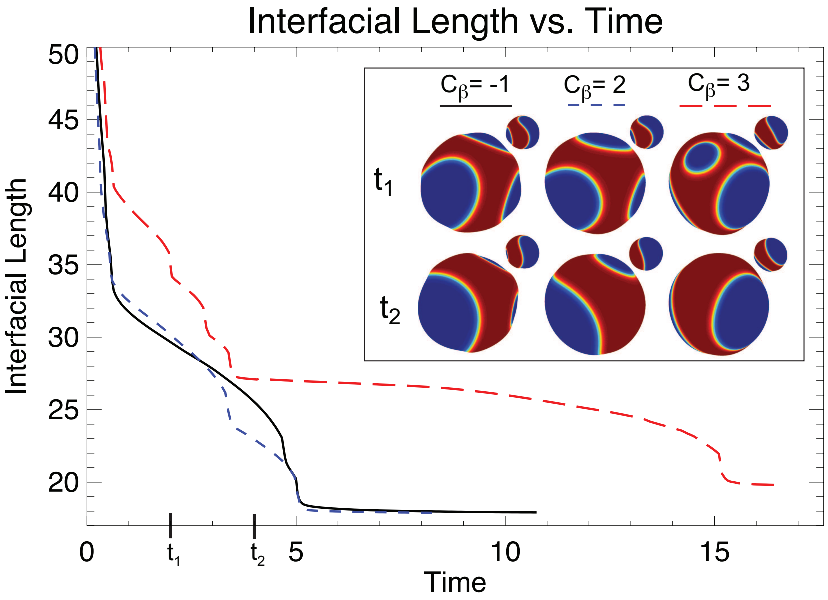

Figure 4.9: Interfacial length vs. time for three systems with $C_\alpha = 1$, 50% α, $r = 3$, $\Lambda_\alpha = \Lambda_\beta = 1$, and $C_\beta = -1$, 2, and 3. Snapshots at two times (marked as t_1 and t_2 on the time axis) from all three systems are presented in the inset, where the color indicates the composition variable ϕ such that the α phase is shown in red, the β phase is shown in blue, and the spectrum of colors in between represents interfaces. The small plots show a view of the back side of the vesicles. The red α phase forms continuous domain morphologies, appearing as a majority phase in these equal mixtures since its spontaneous curvature is closer to the overall vesicle surface curvature. The β phase domains then bulge inward or outward (depending on C_β), deforming the vesicle and slowing the coarsening, with the effect most pronounced with $C_\beta = 3$, being the case where C_β differs most from the overall vesicle surface curvature.

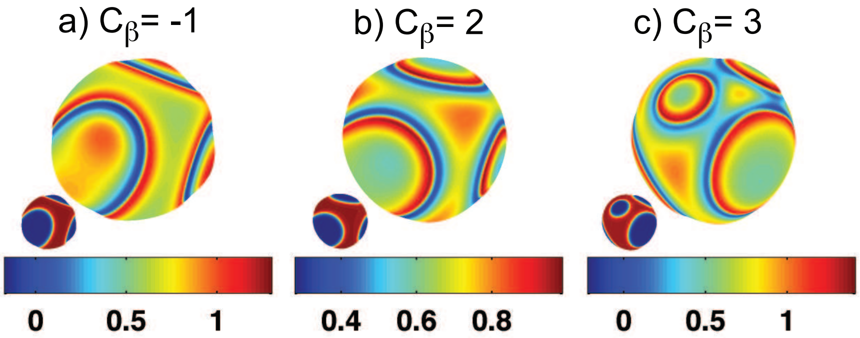

Figure 4.10: Snapshots of three systems with $C_\alpha = 1$, 50% α, $r = 3$, $\Lambda_\alpha = \Lambda_\beta = 1$, and $C_\beta = -1$ (a), $C_\beta = 2$ (b), and $C_\beta = 3$ (c), at time $t = 2.0$. The color bars indicate values of the curvature trace as plotted on the large images. The color on the small plots indicates the composition as a reference, with the α phase in red and the β phase in blue (the small plots are the same snapshots that appear at time $t_1 = 2.0$ in Fig. 4.9). In (a), the β phase domains are only able to adopt negative curvatures near their edges, since the surface tension and internal pressure prevent them from bulging inward over the entire area they occupy. Similarly, the β phase domains in (c) are only able to have a relatively high positive curvature at their edges, which imposes a slightly negative curvature in the adjacent α phase regions, acting as a barrier to domain coalescence and slowing the evolution. The bending energy plays a smaller role in (b) since the difference between the spontaneous curvatures of the two phases and the amount that they differ from the vesicle surface curvature is the smallest of all three systems.

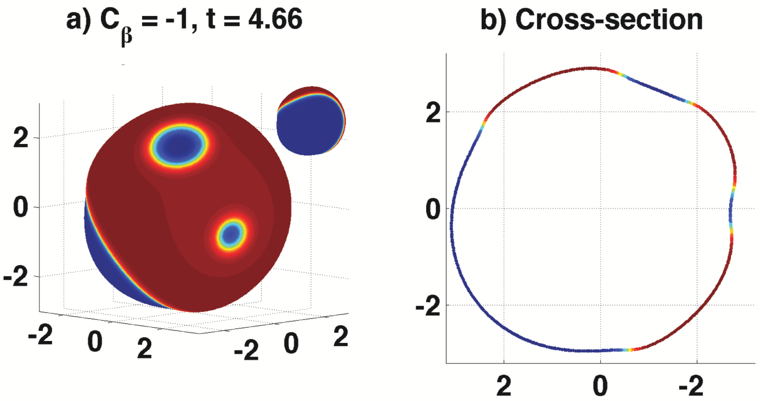

Figure 4.11: A snapshot from the system with $C_\beta = -1$ from Fig. 4.9 at $t = 4.66$ with two of the three β phase domains adopting negative curvatures to satisfy their spontaneous curvature, shown as a surface plot in (a) and a cross-sectional view in (b). The small plot in (a) shows the back side of the vesicle.

systems with $C_\beta = 1/3, 1$ and the "no shape change" case. The $C_\beta = 1/3$ value was chosen because the spontaneous curvatures of the α and β phases differ from the overall vesicle surface curvature ($K = 2/3$) with equal magnitude but opposite sign, and therefore both phases are equally consistent with the overall vesicle surface curvature. Similarly, with $C_\beta = 1$ the two phases have the same spontaneous curvature, thus differing equally from the overall curvature of the vesicle surface. The snapshots and the interfacial length vs. time curves for these three cases appear very similar. As the systems phase separate and continue to evolve, each phase remains continuous and does not separate into multiple isolated domains. This behavior is expected for equal mixtures with no shape coupling since neither phase is a majority or minority phase. However, this behavior was not observed in all systems investigated in this work, as in Fig. 4.9. The similarity of the three systems is an indication that when the spontaneous curvatures of the two phases are such that neither is closer to the overall vesicle surface curvature, the phase morphologies are largely unaffected by the bending energy, as the results appear very similar to the "no shape change" case where bending energy is completely excluded from the model.

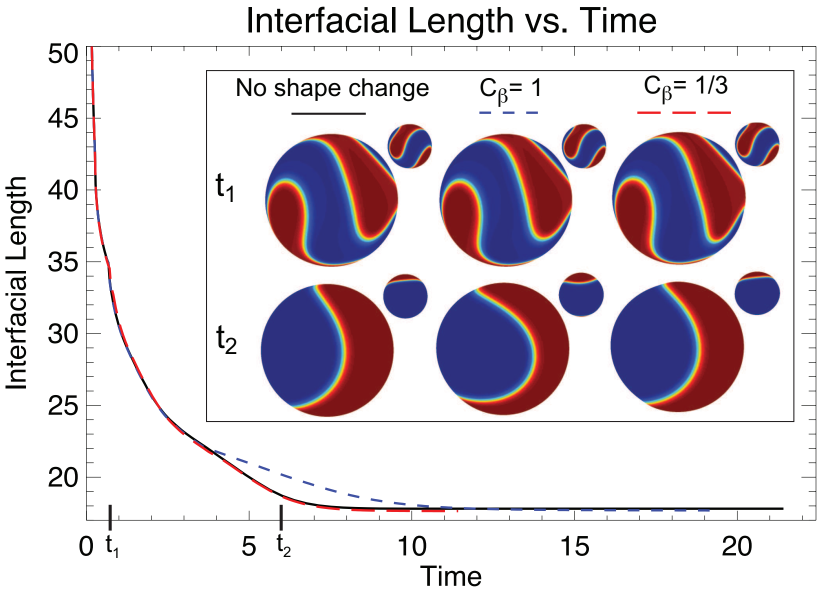

Figure 4.12: Similar to Fig. 4.9, with $C_\alpha = 1$, 50% α, $r = 3$, $\Lambda_\alpha = \Lambda_\beta = 1$, and $C_\beta = 1$, 1/3, and a third control case without shape change or bending energy. These values of C_β were chosen because they differ from the overall curvature of the vesicle surface with equal magnitude as does C_α, with the same sign for $C_\beta = 1$ and opposite sign for $C_\beta = 1/3$. All three systems appear quite similar, with neither phase behaving as a majority or minority phase and evolving to have a single domain of each phase quickly, as the smooth interfacial length vs. time curves indicate. This behavior is expected with equal mixtures in the absence of bending energy.

4.3.2 Varying Phase Fraction

Here a single set of spontaneous curvatures is used for all simulations ($C_\alpha = 1$ as in all cases in this chapter, and $C_\beta = 3$), while the fraction of the two phases is varied. The β phase therefore prefers to assume a curvature more than three times larger than the initial curvature of the vesicle surface, while the α phase prefers a curvature only 50% larger than the curvature of the vesicle surface. Figure 4.13 presents the interfacial length vs. time curves as well as snapshots from systems with equal or nearly equal mixtures, having 40%, 45%, 47.5%, or 50% α phase. The snapshots for the systems with 47.5% α and 50% α show the α phase acting as a majority phase, while the snapshots for the system with 40% α show the β phase acting as the majority phase. The system with 45% α behaves like an equal mixture, based on the snapshots as well as the smooth appearance of the interfacial length vs. time curve. The interfacial length vs. time curves for the 40% α and 50% α systems both have jogs (indicating isolated domains of the apparent minority phase), and also extend to later times than do the curves for the 45% α and 47.5% α cases, indicating that the isolated domains prolong the evolution toward a stationary state. With this set of spontaneous curvatures, we find that a mixture at and possibly around 45% α behaves like an equal mixture.

Figure 4.14 presents cases similar to those in Fig. 4.13, although these are composed of mixtures further away from the effective equal mixture of 45% α, having 30% α, 55% α, and 70% α. All of the interfacial length vs. time curves for these systems exhibit jogs, as would be expected for unequal mixtures. The system where the α phase is the minority phase (30% α) evolves to a stationary state more quickly than the other cases. This is because when the α phase forms small, isolated domains, they do not bulge outward as much as isolated β phase domains do; the highly bulged β phase domains must overcome a highly unfavorable curvature in order to coalesce, and also cause the entire vesicle to adopt a deformed shape that in some cases

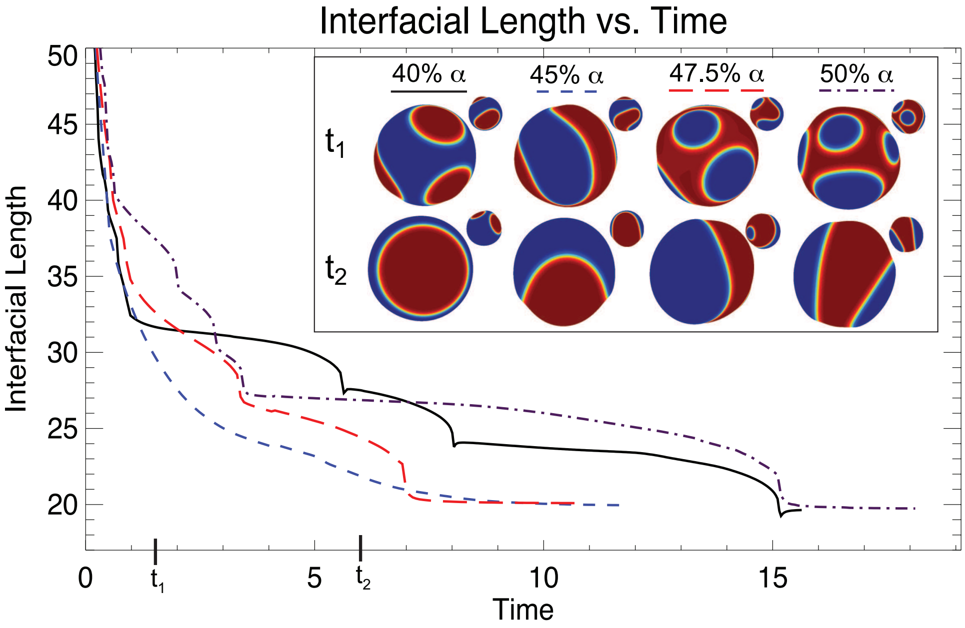

Figure 4.13: Similar to Fig. 4.9, with $C_\alpha = 1$, $C_\beta = 3$, $r = 3$, $\Lambda_\alpha = \Lambda_\beta = 1$, and 40%, 45%, 47.5% and 50% α phase. With this set of spontaneous curvatures, the system with 45% α appears to behave as an equal mixture, rather than the systems with 47.5% or 50% α. This is because C_α is closer to the overall vesicle surface curvature than is C_β by a factor of 7, and is therefore favored to form more continuous domain morphologies even when present at less than 50%. The numerous isolated α phase domains in the system with 40% α, and similarly the isolated β phase domains in the system with 50% α, slow down the evolution compared to the other two systems (as evidenced in the interfacial length vs. time curves), since the isolated domains prefer to have a different curvature than the matrix phase, and must overcome curvature barriers to coalesce.

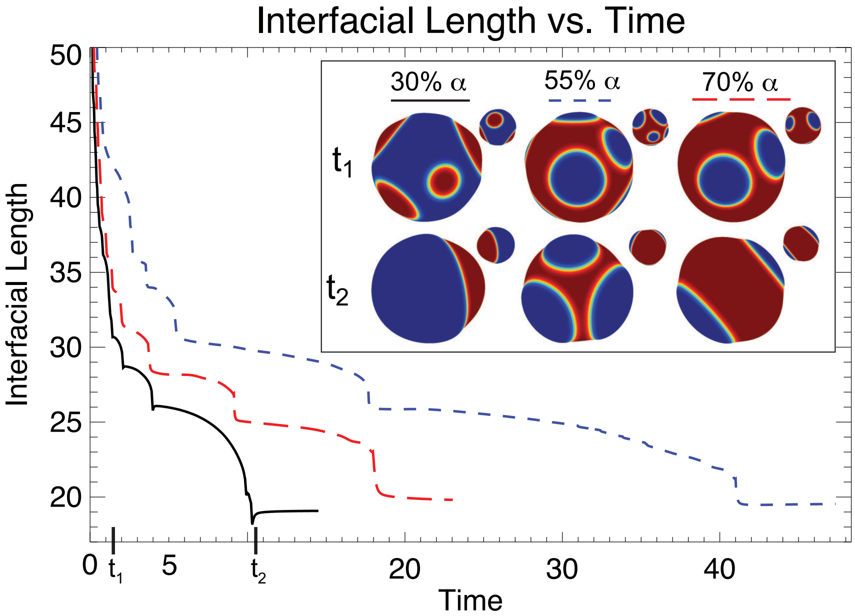

Figure 4.14: Similar to Fig. 4.9, with $C_\alpha = 1$, $C_\beta = 3$, $r = 3$, $\Lambda_\alpha = \Lambda_\beta = 1$, and 30%, 55%, and 70% α phase, representing cases that are further away from the effectively equal mixture fraction (45% α) compared to those shown in Fig. 4.13. Here, diffusion must take place over longer distances during ripening. Also the smaller isolated domains are able to better adopt their spontaneous curvatures since their deformation is less hindered by the internal pressure than it would be for larger domains. The system with 55% α exhibits special behavior, as explained in the text.

pushes the β domains further apart. This behavior is much less significant when the lower-curvature α phase domains are in the minority. Comparing with the systems in Fig. 4.13, the time axis on the interfacial length vs. time plots is much longer here, since the systems here have less of the minority phase, and longer distances must be overcome for diffusion and coalescence. Also, smaller domains are able to adopt their spontaneous curvatures more easily than larger domains, leading to an energetic penalty for ripening and coalescence.

The system with 55% α takes significantly longer to reach its stationary state than do the other similar systems. As the snapshots show, this is because three β phase domains have reached a favorable size in terms of the bending energy, where they bulge outward enough to resist coalescence even in close proximity to each other. This observation can be explained in terms of the line-tension and bending energies plotted over time in Fig. 4.15. At the three times marked t_a, t_b, and t_c, the system has evolved to have three, two, and one β phase domain remaining, respectively, and at each of these times the line-tension energy decreases while the bending energy increases. During ripening, the shrinking domain is able to adopt a curvature close to C_β as it becomes small enough, lowering the bending energy temporarily. However, as the shrinking domain gets closer to disappearing, the remaining domain or domains grow, which are then forced to adopt less favorable curvatures. The shrinking domain also has a decreasing contribution to the bending energy as it decreases in area with time. While the increase in bending energy associated with ripening slows the evolution, the larger decrease in line-tension energy continues to drive the ripening, and the system eventually forms a single β phase domain.

4.3.3 Varying Bending Rigidity

Two simulations were run using unequal bending rigidities for the two phases, setting $\Lambda_\alpha = 1$ and $\Lambda_\beta = 1.5$ and either $C_\beta = -1$ or 0, along with $C_\alpha = 1$, $r = 3$, and

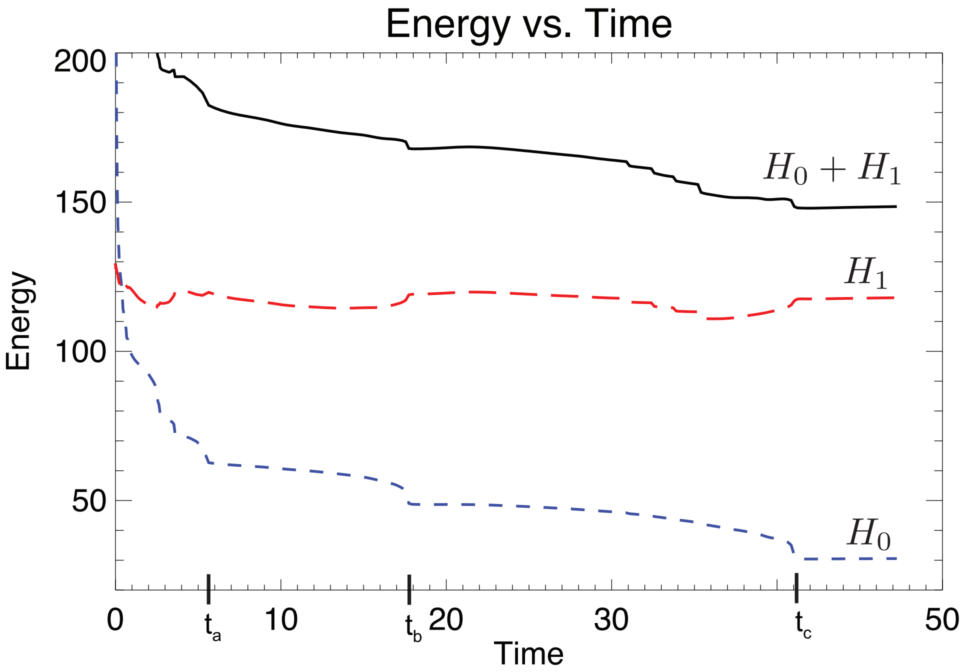

Figure 4.15: Line-tension energy, H_0 (blue); bending energy, H_1 (red); and combined energies $H_0 + H_1$ (black) vs. time for the system with $C_\beta = 3$ and 55% α. The three times marked t_a, t_b, and t_c are the times when the system has evolved to have three, two, and one β phase domain remaining, respectively (see Fig. 4.14 for a snapshot of the morphology with three domains at $t = 10.5$). While the line-tension energy decreases when a shrinking domain disappears, the bending energy increases and thus provides an energy barrier for reducing the number of domains.

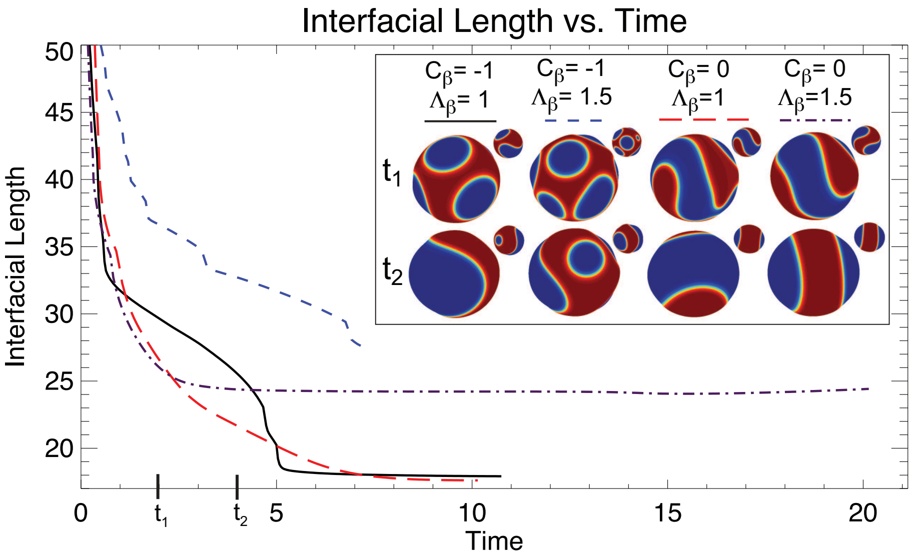

Figure 4.16: Similar to Fig. 4.9, with $C_\alpha = 1$, $r = 3$, 50% α, and $\Lambda_\alpha = 1$, with either $C_\beta = -1$ or 0 and either $\Lambda_\beta = 1$ or 1.5. Both of the systems with $\Lambda_\beta = 1.5$ evolved to extreme shapes with overhangs not able to be resolved with our model rather than reaching a stationary state. These systems evolved more slowly since the interfacial length vs. time curves are higher at all times. Compared to the equal rigidity simulation snapshots with the same parameters, the deformations are more severe, hindering domain coalescence and hence slowing evolution.

50% α. Figure 4.16 presents plots of interfacial length vs. time as well as snapshots for these two cases, along with comparable cases with $\Lambda_\alpha = \Lambda_\beta = 1$. The systems with the larger Λ_β have interfacial length vs. time curves that have similar features as the curves of their comparable cases with equal rigidities. However, at any given time, the systems with larger bending rigidity have more interfacial length and are therefore evolving more slowly than cases with smaller bending rigidity. Additionally, the deformation in the larger-rigidity cases is more extreme, to the degree that the single-valued radial function that is used to parametrize the vesicle surface was no longer able to resolve the highly deformed surface and the simulations ceased to run at the time when their interfacial length vs. time curves end.

4.3.4 Cases with Anomalous Kinetics

One particular point in parameter space, with $C_\alpha = 1$, $C_\beta = 2$, $r = 3$, $\Lambda_\alpha = \Lambda_\beta = 1$, and 60% α, exhibits enhanced stability in a configuration with two β phase domains on the ends of a vesicle that has evolved to a shape resembling an ellipsoid. Two simulations using different sets of random noise for the compositional initialization were run using these parameters; one of these (60% α Case A) took more than twice as long to reach the configuration with a single domain of each phase compared with systems with all of the same parameters but with 55% α or 65% α, and the other (60% α Case B) appeared to have enhanced stability with two β phase domains for approximately nine times longer than it took for the 55% α and 65% α to reach a stationary state (the simulation was discontinued at that time). Figure 4.17 presents the interfacial length vs. time plots as well as representative snapshots, illustrating the relative time scales over which the 60% α simulations remain stable with two β phase domains. This parameter set has the unique property that the configuration with more than one domain has a low enough total energy that the system can maintain such a configuration for a significant length of time.

Figure 4.18 compares the curvature trace and bending energy of the single-domain stable configuration for the 55% α and 65% α cases with that of the double-domain configuration for the 60% α cases. The curvature profiles in both phases appear quite similar for the cases with 55% α, 65% α, and Case A, while for Case B, the curvature in the β phase has higher values, closer to the spontaneous curvature $C_\beta = 2$. This is also indicated in the bending energy plots, where the bending energy in the β phase domains of the Case B simulation is lower than in the β phase domains of any of the other three simulations, explaining their enhanced stability compared with a single-domain configuration. The difference between Cases A and B seems to stem from the shape of the vesicle, which for Case B has formed a more elongated ellipsoidal shape. This allows the β phase domains to have higher curvature (more consistent with

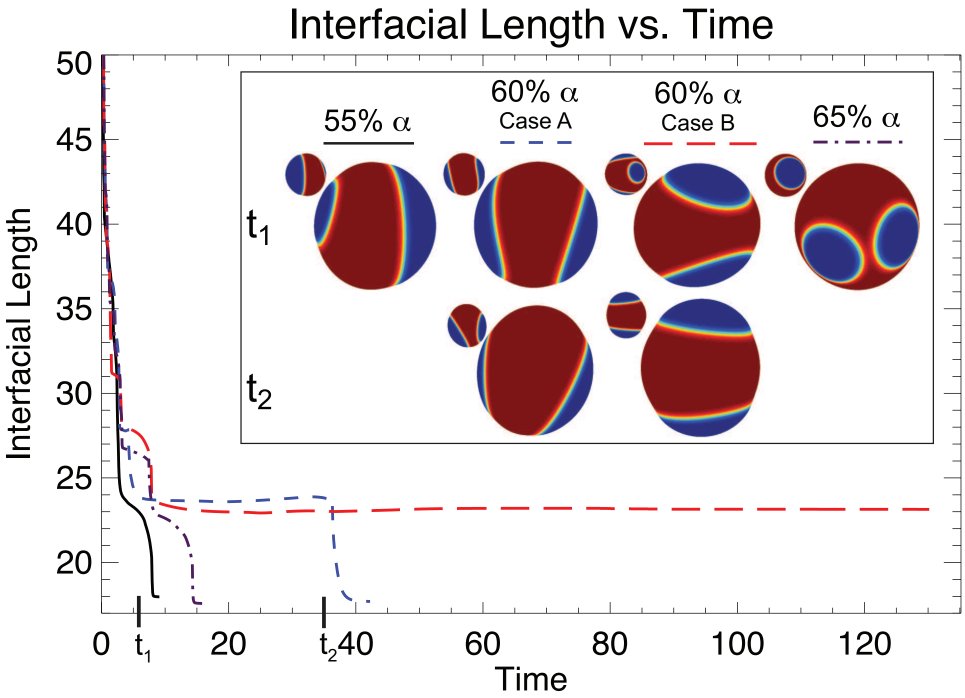

Figure 4.17: Similar to Fig. 4.9, with $C_\alpha = 1$, $C_\beta = 2$, $r = 3$, $\Lambda_\alpha = \Lambda_\beta = 1$, and 55%, 60%, and 65% α phase. The 60% α Cases A and B differ only in the random seed used for the initialization. Both of the simulations with 60% α evolved to morphologies with two domains of the β phase, persisting through very late times in Case B, as indicated by the interfacial length vs. time curves (the Case B simulation was discontinued at approximately $t = 130$).

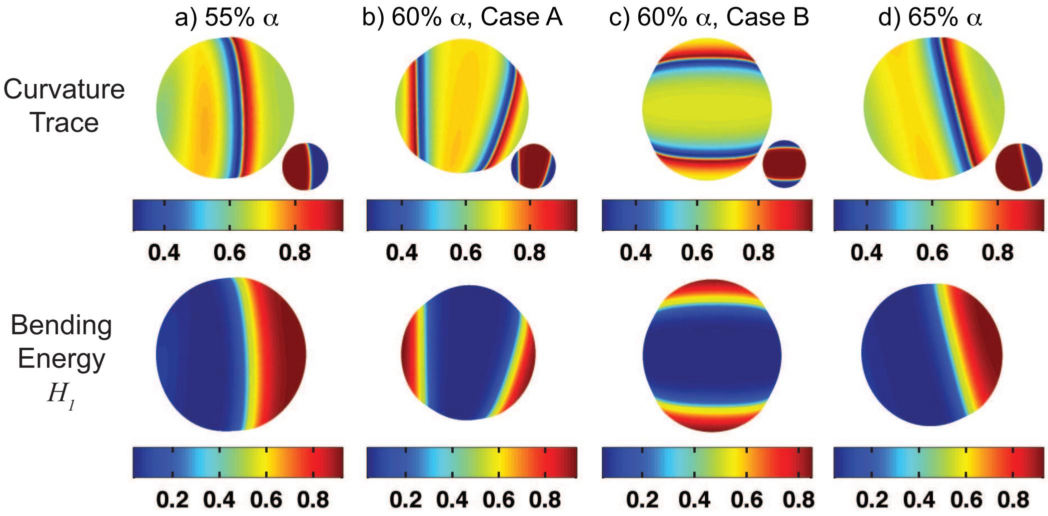

Figure 4.18: Plots of the curvature trace (top row) and bending energy H_1 (bottom row) for systems with $C_\alpha = 1$, $C_\beta = 2$, $r = 3$, $\Lambda_\alpha = \Lambda_\beta = 1$, and 55%, 60%, and 65% α phase. The 60% α Cases A and B differ only in the random seed used for the initialization. In the top row, the color bars indicate values of the curvature trace as plotted on the large images, while the color on the small plots indicates the composition as a reference, with the α phase in red and the β phase in blue. The plots for Cases A and B show their configuration with two β phase domains, while the other plots show stationary states. Comparing the curvature trace plots, they appear quite similar qualitatively and quantitatively, with the exception of Case B, where a larger portion of the β phase domains have adopted the maximum curvature (closer to $C_\beta = 2$), resulting in lower bending energy compared with the single β phase domains in the other systems. This lower bending energy gives the configuration in Case B enhanced stability, despite having a larger line-tension energy than systems with one β phase domain.

their spontaneous curvature), and also presents a larger barrier for their coalescence or diffusion. For Case A, this elongation was not achieved from the random seed. However, the process of arriving at a single β phase domain still took significantly longer for Case A than for the cases with 55% and 65% α, indicating that this particular parameter set is prone to having enhanced stability in configurations with multiple β phase domains.

4.3.5 Ellipsoidal Vesicles

While all vesicle systems reported in this work thus far have been initialized as perfect spheres, two simulations were performed where the shape was initialized as an ellipsoid instead. The prolate spheroidal ellipsoid shape utilized has a major axis of 3 and minor axes of 2. The parameters used for these cases are $C_\alpha = 1$, $C_\beta = -1$, $\Lambda_\alpha = \Lambda_\beta = 1$, and either 50% or 40% α. Both systems exhibit enhanced stability in a state with multiple domains of one of the phases, as opposed to the configuration where there is only a single domain of each phase (the configuration with lowest line-tension energy). Figure 4.19 shows these enhanced-stability states, plotting the curvature trace and bending energy (from Eq. 3.3) on the surface.

In Sec. 4.3.1, we reported that a system with $C_\beta = -1$ and 50% α (initialized as a sphere) had the α phase behaving as a majority phase, isolating individual β phase domains. We observe this here in the same system but with the ellipsoidal initialization, and find that the β phase domains partition to the low-curvature parts of the vesicle, while the α phase covers the areas with the highest positive curvature. From the snapshots displaying the curvature trace, it appears that the α phase is able to adopt its spontaneous curvature over a large region of the vesicle, and would need to significantly alter that favorable curvature in order to allow the β phase domains to coalesce, contributing to the enhanced stability of this configuration.

With only 40% α phase, there is enough of the β phase such that the α phase behaves as the minority phase, and the isolated α phase domains are able to segregate to the higher-curvature regions of the ellipsoid, achieving curvatures very close to C_α at the ends of the vesicle. Over time, we observe that the vesicle becomes more elongated with less outward bulging around the lower-radius middle portion, as the α phase domains form caps on the ends to satisfy their spontaneous curvature while the negative curvature preference of the β phase also favors this deformation to reduce (positive) curvature. Here, the bending energy drives the system further from a state

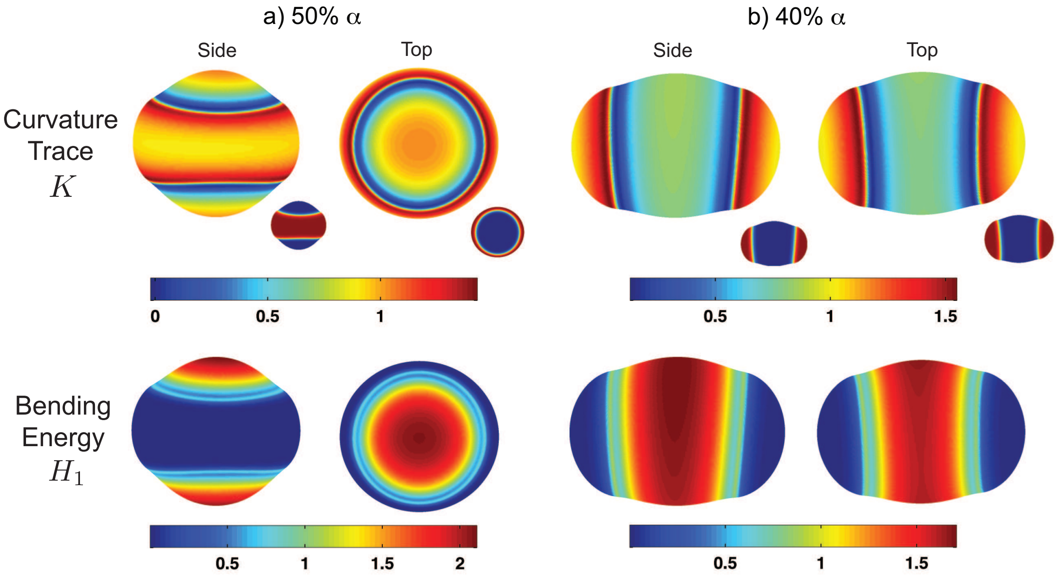

Figure 4.19: Plots of the curvature trace (top row) and bending energy H_1 (bottom row) for systems initialized with ellipsoidal shapes (major axis=3, minor axes=2) with $C_\alpha = 1$, $C_\beta = -1$, $\Lambda_\alpha = \Lambda_\beta = 1$, and 50% phase in (a) and 40% α phase in (b). In the top row, the color bars indicate values of the curvature trace as plotted on the large images, while the color on the small plots indicates the composition as a reference, with the α phase in red and the β phase in blue. Each plot represents the morphologies with enhanced stability observed in the simulations. In both systems, the α phase has partitioned to the regions of the ellipsoid with the highest positive curvature, as would be expected given $C_\alpha = 1$ and $C_\beta = -1$. However, since the α phase behaves as the majority phase in the 50% α case and the minority phase in the 40% α case, the morphologies are quite different. These distributions of the phases allow the system to adopt curvatures closer to the spontaneous curvatures of the phases.

with a single α phase domain with time, despite the driving force for the α phase domains to combine from the line-tension energy. In these ellipsoidal vesicles with enhanced stability of multiple minority phase domains (in addition to the vesicle in the previous section, initialized as a sphere but later evolving into an ellipsoidal shape), the bending energy contribution stabilizes the system against coarsening that would reduce the line-tension energy. This is unique in that all other parameter sets investigated eventually reached the stationary state of a single domain of each phase. The elongated shape is the common thread in all of the systems that maintain multiple domains for extended time, where the phases are able to migrate to locations that best satisfy their spontaneous curvatures and remain there, as opposed to when they are on an overall spherical vesicle where no one location is preferable for forming domains over another, and the line-tension energy is able to drive coalescence.

This observation that the shape of the membrane influences the compositional dynamics is similar to the observations reported for the nearly planar case with ripple perturbations in Sec. 3.3.2 and Sec. 3.3.3. In all of these systems, we observe that the membrane shape can be used to direct compositional morphologies. While much of the discussion in this work has revolved around how membrane composition can affect the shape, these are examples of the reverse effect, where membrane shape can affect composition.

4.4 Conclusions

Based on the results from the various parameter sets investigated in this chapter, the following overall conclusions can be drawn. First, the dynamics appear to be affected by the relationship between the overall curvature of the vesicle surface (a function of the size of the vesicle) and the spontaneous curvatures of the two phases. The spontaneous curvature does not appear to play a role in the dynamics if neither phase has a spontaneous curvature more similar to the overall curvature of the vesicle compared to the other phase. This occurs when C_α and C_β differ from the overall vesicle surface curvature with equal magnitude, but not necessarily the same sign. If this is not the case, and one phase has a spontaneous curvature closer to that of the overall vesicle surface compared with the other phase, then the spontaneous curvature has two primary effects, which are described below.

First, the phase with spontaneous curvature closer to the overall vesicle surface curvature is favored to form more continuous domain morphologies, even if it is present at an equal or slightly less than equal fraction as the other phase. In the absence of curvature effects, an equal mixture of two phases means that neither phase is a majority (or matrix) phase, and therefore the system phase separates into continuous, interwoven domains that over time unweave to form hemispheres. An unequal mixture will have isolated minority phase domains in a continuous background of the majority phase. These two different evolution regimes can be distinguished by examining the phase morphologies and the interfacial length vs. time curves, where the curves appear very smooth for equal mixtures and have jogs for unequal mixtures. When one phase is favored by curvature to form more continuous domain morphologies in an unequal mixture, we observe the situation expected for equal mixtures. This was observed when the phase favored to form continuous domains is present at less than 50%. In these cases, an equal mixture has the curvature-favored phase behaving like a majority phase, causing the minority phase domains to persist for longer times than would occur in the absence of bending energy. This effect is more pronounced when the unfavored curvature is less favored (*i.e.*, it is further from the overall vesicle surface curvature), lowering the phase fraction with interwoven domain morphologies further from 50%.

Second, we find that the following factors can slow the evolution of the system toward a single domain of each phase, by favoring multiple domains to persist for far longer than the line-tension energy alone would permit. If the phase that has a spontaneous curvature that differs more from the overall vesicle curvature is the minority phase, then the resulting isolated domains experience larger deformations and their coalescence is prevented by the unfavorable curvature of the other phase dividing them. In some cases, the bending energy contribution to the total energy becomes competitive to the line-tension energy and enhances the stability of configurations with multiple domains of the extreme curvature phase, particularly with elongated vesicle shapes. This observation is similar to that from the nearly planar membrane systems with ripples imposed, where the imposed shape of the membrane can direct compositional morphologies. Lastly, if one phase has a larger bending rigidity, we observe larger deformations, which is another effect slowing the phase evolution compared with similar systems where the phases have equal bending rigidities.

In summary, we have found that the coupling of compositional phases with mechanical effects leads to unexpected morphologies and often a slower evolution to equilibrium, in some cases with multiple domains of a single phase persisting for very long durations of time despite the driving force to reduce line-tension energy. Mechanical properties are thus important to the study of lipid phase behavior, and the findings here could be useful for engineering vesicles with particular phase morphologies and behaviors, in the context of functionalized membranes as biomimetic surfaces or drug delivery vehicles (62, 194, 195).

CHAPTER V

Cylindrical Tubule Membrane Model

5.1 Introduction

Lipid membrane tubules are of interest because they not only appear in nature and have potential technological applications, but also because they have a restricted geometry useful for isolating certain phenomena. Tubule structures with diameters of 50 to 200 nm, referred to as tunneling nanotubes (TNTs), have been observed forming connections between live cells. The TNTs were stretched between the closest points between two cells, and were observed to not be in contact with the substrate on which the cells were grown. While their diameters were on the order of nanometers, their lengths were in some cases equal to multiple cell diameters, and appeared to be used for transmission of vesicles and even organelles between cells, making them important for intercellular communication and transport (196). High-curvature tubules are also associated with transport within the endoplasmic reticulum and in connection with the Golgi complex (197, 198). In terms of technological applications, tubules can be used to connect membrane vesicles to form microreactor networks of containers of reactants and channels connecting them (61).

Most importantly for the investigation presented here, these long, thin tubules have a restricted geometry, and can be useful for investigations of membrane behavior. Tubules created in the laboratory are typically made using a technique known as micropipette aspiration, where a microbead is attached to one side of a vesicle, and on the opposite side a part of the vesicle is aspirated into a pipette. As the vesicle is aspirated into the pipette and it is drawn away from the microbead, a thin tubule is pulled from the membrane as shown in Fig. 5.1. Since the geometry of the vesicle is simple and the diameter of the pipette is known, the inner and outer diameters of the tubule can be calculated mathematically, which is useful because they are often smaller than what can be resolved by optical microscopy. Experiments have been performed with tubules drawn from phase-separated vesicles showing that the liquid-disordered (L_d) phase segregates to the high-curvature tubule (70), and in homogeneous lipid mixtures that tubule curvature could induce demixing (199). Other methods for creating membrane tubules or tube-like vesicles include hydrodynamic flow (200, 201), osmotic deflation (202, 203), and cationic nanoparticles placed inside vesicles used to push tubules out from the vesicle membrane (204).

In this chapter, the model from Chapters III and IV is modified in order to simulate membrane tubules with a cylindrical background geometry. The restricted geometry of the tubule introduces new aspects to the membrane system, such as barriers to coarsening (as observed in the work in Ref. 200, see Fig. 5.2), and also instabilities originating from the surface tension of the tubule driving it to break up.

5.2 Methods: Modifying the Spherical Membrane Model to a Cylindrical Geometry

The major modification made to the spherical vesicle model to develop this cylindrical model is the coordinate system; we here use cylindrical coordinates rather than spherical coordinates. This means that the surface of the tubule is still described by a radius function, but this radius function is written in terms of an azimuthal angle, θ, and a vertical position, z. The three-dimensional position vector now appears as

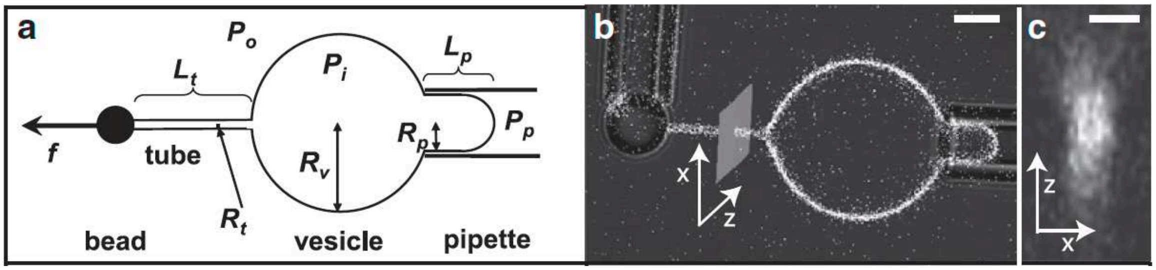

Figure 5.1: The micropipette aspiration technique. (a) A drawing of the technique, with the microbead on the left, pulling the tubule out from the vesicle in the center, while aspirated into the pipette on the right. P_i is the pressure inside the vesicle, P_o the pressure outside the vesicle, and P_p the pressure within the micropipette. Radii are labeled as R_t for the tubule, R_v for the vesicle, and R_p for the pipette. L_t is the length of the tubule, and L_p is the length of the portion of the vesicle aspirated into the pipette. The force from pulling the microbead is labeled as f. These quantities can be used to calculate the radius of the tubule. (b) A combined transmitted light/confocal fluorescence micrograph of the same setup in the schematic, with the scale bar representing 5 microns. (c) A confocal line scan image of the cross section of the tubule at the location in the shaded gray box in (b). The scale bar represents 1 micron. Reproduced from Ref. 205.

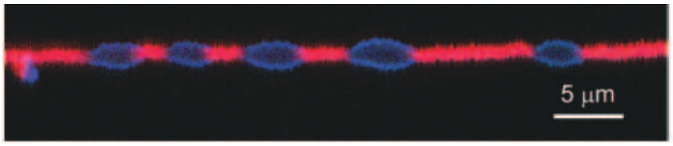

Figure 5.2: A confocal fluorescence micrograph of a phase-separated membrane tubule, composed of a mixture of dioleoylphosphatidylcholine (DOPC), sphingomyelin, and cholesterol. The red dye partitions into the L_d phase while the blue dye partitions into the L_o phase. The L_o domains appear to bulge outward from the high-curvature tubule, likely because of the higher bending rigidity and lower curvature preference compared with the L_d phase (200). Figure reproduced from Ref. 200.

$$\mathbf{r} = [r\cos\theta, r\sin\theta, z]. \tag{5.1}$$

In this tubule model the indices $i = 1$ and 2 correspond to θ and z, respectively, and the notation r_i indicates a partial derivative of r with respect to coordinate i. The tangent vectors within the membrane surface in directions parallel to θ and z are given by

$$\mathbf{e}_1 = \frac{\partial \mathbf{r}}{\partial \theta} = [-r\sin\theta + r_1\cos\theta, r\cos\theta + r_1\sin\theta, 0], \tag{5.2}$$

$$\mathbf{e}_2 = \frac{\partial \mathbf{r}}{\partial z} = [r_2\cos\theta, r_2\sin\theta, 1]. \tag{5.3}$$

As with the vesicle model, these basis vectors can be used to construct the metric tensor, curvature tensor, and differential operators with the expressions in Appendix A. Aside from these geometrical tensors and operators, the theory of the tubule model is identical to that of the spherical model.

5.2.1 Numerical Methods

For the vesicle model, special methods were used when imposing a mesh of points over the vesicle surface in order to avoid the polar points and the variation in mesh size from equator to pole. However, in this tubule model using a cylindrical background geometry, neither of these problems are encountered, since there are no poles, and the geometry is only curved in the azimuthal direction so there is no “equator.” Therefore, the Yin-Yang grid system is not needed for the tubule model, and a single, simple mesh is used instead. This mesh spans the circumference of the tubule with $\theta = [-\pi, \pi]$, and the length of the tubule in z. Periodic boundary conditions are imposed in the θ direction as a result of the axial symmetry since $f(\theta = -\pi) = f(\theta = \pi)$, and periodic boundary conditions with various periodicities are used in the z direction. By not requiring the Yin-Yang grid system, no interpolation is necessary, nor are any special algorithms needed to calculate surface integrals because there is only a single grid.

5.2.2 Simulation Parameters and Initializations

Unless otherwise specified, all simulations use the following parameters: $r = 1$, $\Lambda_\alpha = \Lambda_\beta = 1$, $w = 367$, $\zeta = 0.665$, $M = 1$, $\Gamma = 0.05$, and $P = 5$. The parameters $\Lambda_\alpha = 1$ and the radius $r = 1$ set the energy and length scales of the system, respectively, and all other quantities are measured with respect to them and are thus dimensionless in the model. The computational grid consists of 128 points in θ, and in z the number of grid points is set such that the grid spacing $\Delta z = \Delta\theta$. The shape is initialized as a perfect cylinder, which has a curvature trace of $K = 1$. As in the previous chapters, the parameters w and ζ are selected to satisfy two constraints: (i) they are chosen such that a minimum of 6 grid points resolve the interfaces, and (ii) as a result of the bending energy term, the minima of the double-well potential in Eq. (3.2) can shift, and w and ζ are specified to set the line tension to be large enough such that this shift is less than 2%. The friction coefficient and pressure are selected for numerical stability and such that the tubule is slightly inflated, respectively.

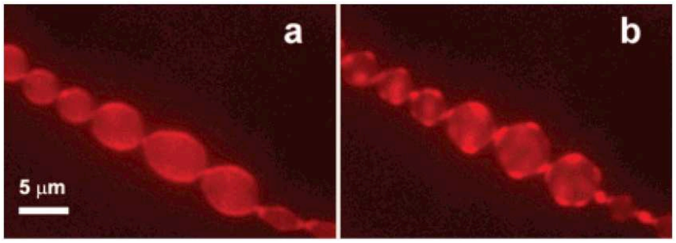

Figure 5.3: A lipid bilayer tubule composed of a ternary lipid mixture exhibiting the pearling instability, with image (b) taken 30 seconds after image (a), where phase separation has been induced by lipid peroxidation. The L_d phase appears light while the L_o phase appears dark, and it can be observed that the L_d phase partitions to the higher-curvature neck regions between the pearls. Reproduced from Ref. 200.

5.3 Results and Discussion

The cylindrical geometry of the membrane tubules discussed in this chapter introduces a tendency for instability not present in the nearly planar and vesicle systems. This instability is known as the Plateau-Rayleigh instability, where a cylinder of fluid with the proper aspect ratio will break up into droplets as a result of surface tension (206). When the length of the cylinder is greater than the circumference, small oscillatory perturbations in the shape will grow, leading to the cylinder pinching off (207). In lipid bilayer membrane tubules, this type of instability has been observed in the form of pearling, where the tubule pinches together in a series of locations, but does not break apart, since the hydrophobic forces among the lipids drive the bilayer to remain intact. An experimental image of this pearling instability is shown in Fig. 5.3.

5.3.1 Bending Energy as a Stabilizer Against Pearling

The bending energy of the membrane will also affect the stability of the tubule, and the following simulations were performed to investigate whether or not the pearling instability could be stabilized by the bending energy with nonzero spontaneous curvature. Two simulations were run, each with a single phase assigned with a spontaneous curvature $C = 1$. The Plateau-Rayleigh instability is theoretically predicted to occur only if the tubule length is greater than a threshold value: the tubule circumference. Therefore, we set the tubules to be twice as long as this threshold length, with radius $r = 1$ and length $\ell = 4\pi$. The shape of the tubules was initialized with a small sinusoidal perturbation with an amplitude of 0.1, as shown in Fig. 5.4. For Case A, the bending rigidity was set as $\Lambda = 1$, while in Case B, we set $\Lambda = 0$ to remove the effects of the bending energy and spontaneous curvature. Both cases had no internal pressure contribution ($P = 0$), leaving only the surface-tension energy (and bending energy in Case A) to govern the evolution. In Case A, we observe the tubule evolving toward a straight cylinder, where the initial perturbation diminishes over time, while in Case B, the perturbation is amplified over time. A plot of the difference between the maximum radius and minimum radius vs. time is presented in Fig. 5.5 for both cases, illustrating the different behaviors. Since the only difference between these two systems is the presence of the bending energy with spontaneous curvature, we conclude that the bending energy must be the stabilizing factor.

5.3.2 Two-Phase Tubules

We now focus on two-phase tubule systems where the phases have mismatched spontaneous curvatures of $C_\alpha = 0$ and $C_\beta = 2$, with a tubule radius of $r = 1$ (and therefore a curvature trace of $K = 1$). Thus the α phase prefers to have a lower curvature than the initial shape while the β phase prefers to have a higher curvature, while both differ from the overall curvature of the tubule with equal magnitude. Simulations were performed with 50% α and 40% α using a tubule of length $\ell = 8\pi$, which is large enough to render the effect of the boundary condition in z negligible.

Figures 5.6 and 5.7 present snapshots taken during the evolution of the tubules with 40% and 50% α, respectively. As in the corresponding vesicle system, because

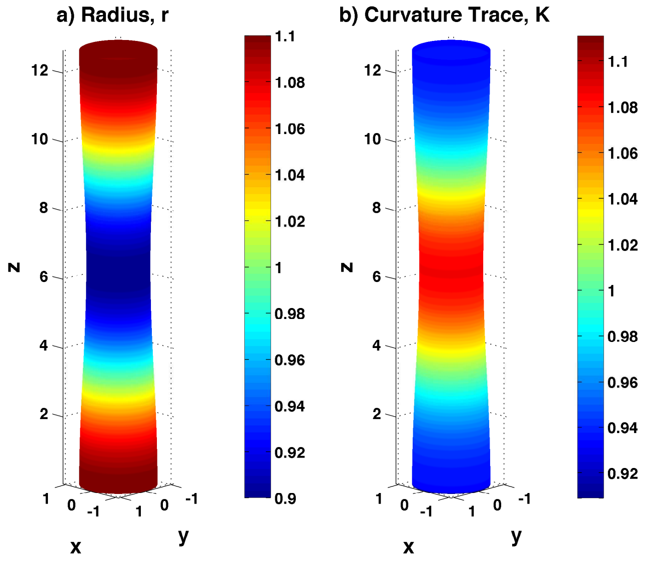

Figure 5.4: Initial conditions for the Case A and Case B simulations used to test whether spontaneous curvature can stabilize a tubule against the Plateau-Rayleigh instability, using a sinusoidal radial perturbation with amplitude 0.1.

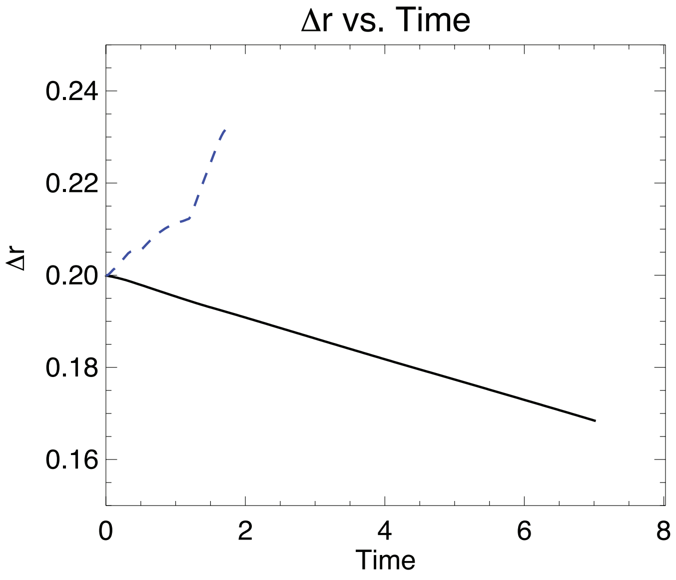

Figure 5.5: Plot of the difference between the maximum and minimum radius (Δr) vs. time for the Case A (with bending energy, solid black line) and Case B (without bending energy, dashed blue line) single-phase tubule simulations. The curve for the Case B simulation ends when the simulation could no longer run. This illustrates that the bending energy can stabilize tubules against the pearling instability.

neither phase has a spontaneous curvature closer to the overall curvature of the tubule surface, we observe that the system with 50% α indeed appears to behave like an equal mixture, and the system with 40% α has the α phase behaving as the minority phase as expected. The 50% α case coarsens more quickly at early times, as observed by comparing the number of domains in the snapshots in Figs. 5.6b and 5.7b. The system with 50% α initially forms both stripe and caplet domain morphologies, which ripen to form rings over time. This is because the primary driving force for coarsening, the interfacial energy reduction, has only a limited role when a stripe morphology is established. For example, if the radius of the tubule is constant, the line-tension contribution to the chemical potential is constant at the interfaces of rings. However, when rings form in the tubule system here, the bending energy contribution deforms the tubule, and ring interfaces are then located at regions with different radii, and thus they have different curvatures. This creates a driving force for coarsening.

As in the vesicle simulations with mismatched spontaneous curvatures, we observe that domains are able to adopt their spontaneous curvatures best in regions adjacent to interfaces, but not far from interfaces. This is because the volume penalty for bulging outward must generally be compensated by a region bulging inward. Furthermore, since $C_\alpha = 0$ and $C_\beta = 2$ and the overall tubule has a curvature of 1, it is natural for the morphology to best adopt the spontaneous curvatures near the interfaces, where each phase prefers to deform is such a way that compensates for the deformation in the other phase.

The system with 40% α at all times exhibits only caplet morphologies. Even when a caplet becomes large at late times, it does not join to itself around the tubule to form a ring. Such self-coalescence events are observed infrequently in the system with 50% α also, where a ring domain that wraps around the tubule appears to form only if the domain is already contiguous around the tubule following initial phase separation. If the domain forms a caplet, it is difficult to form a ring from it because

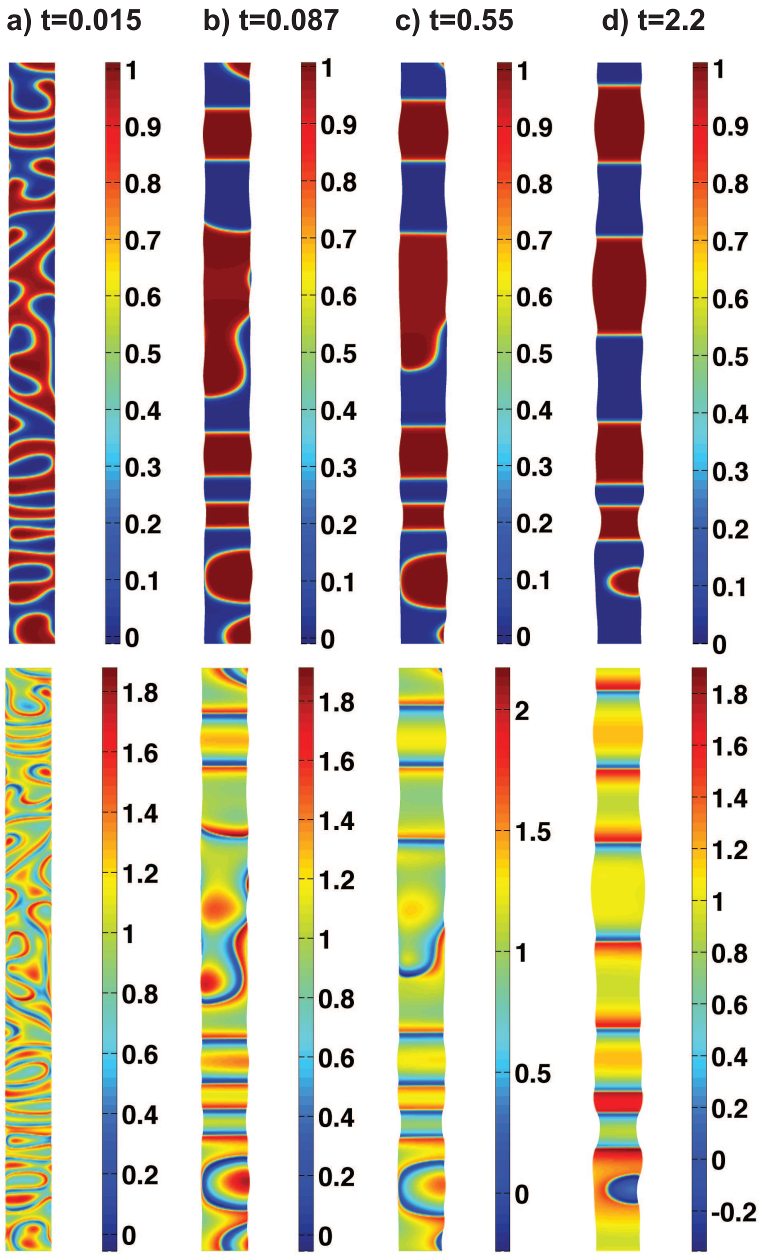

Figure 5.6: Snapshots of composition (top row) and curvature trace (bottom row) throughout the evolution of a tubule with $r = 1$, $C_\alpha = 0$, $C_\beta = 2$, and 50% α, at (a) $t = 0.015$, (b) $t = 0.087$, (c) $t = 0.55$, and (d) $t = 2.2$. Both phases form ring morphologies at later times, which coarsen as a result of deformation driven by the bending energy.

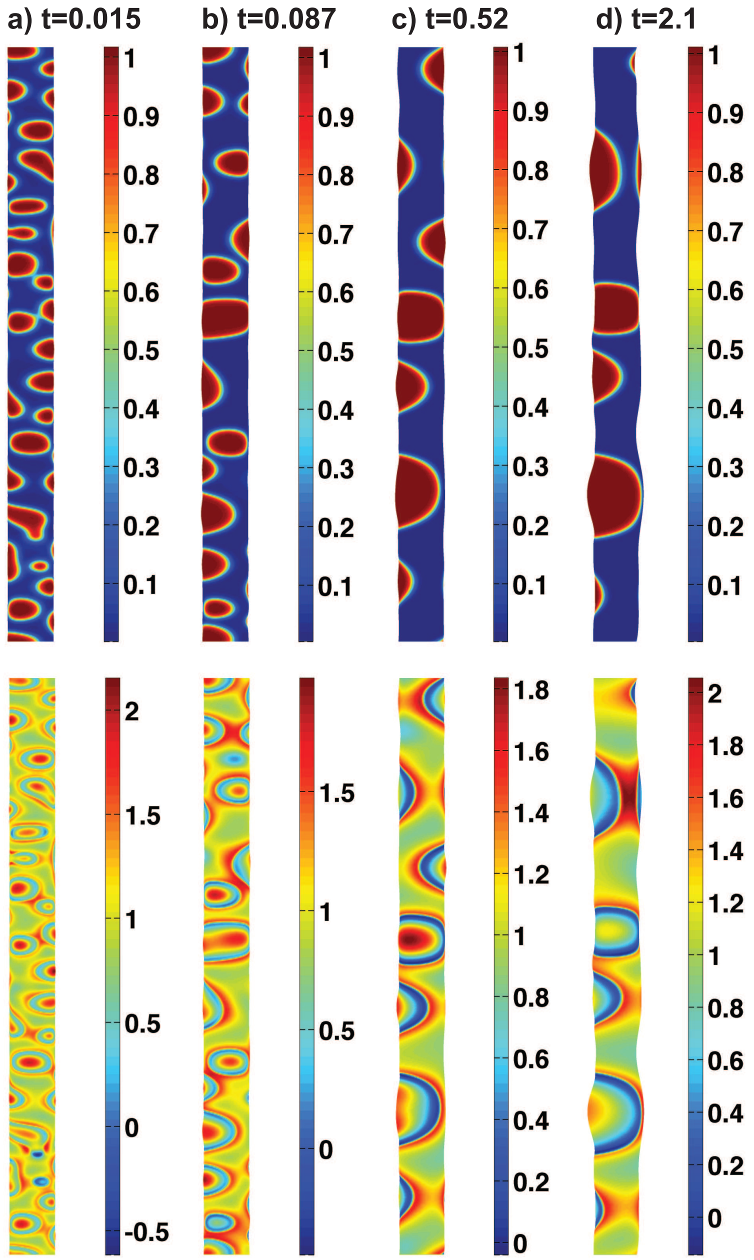
a) t=0.015

b) t=0.087

c) t=0.52

d) t=2.1

Figure 5.7: Snapshots of composition (top row) and curvature trace (bottom row) throughout the evolution of a tubule with $r = 1$, $C_\alpha = 0$, $C_\beta = 2$, and 40% α, at (a) $t = 0.015$, (b) $t = 0.087$, (c) $t = 0.52$, and (d) $t = 2.1$. The α phase forms caplet domains, which are able to adopt their spontaneous curvatures in regions adjacent to interfaces.

of the short-range repulsion of the interfaces due to bending energy, as explained below. This is analogous to the 40% α systems in the nearly planar model with no special perturbations, where a domain needed to connect with itself across the enforced periodic cell in order for stripes to form; here, the periodicity comes from the tubule's continuous geometry in the θ direction.

The short-range repulsion between interfaces, which prevents the formation of a ring from a caplet domain, even when the caplet domain is large enough to span the tubule, can be understood as follows. Since the α phase domains prefer to have a lower curvature than the overall curvature of the tubule, the bending energy can be reduced if the radius of the tubule increases, which decreases the curvature in the θ direction. However, the internal pressure penalizes the tubule for adopting a larger radius over long distances in the z direction. Therefore, the local regions of larger radius are adjacent to regions with smaller radius, creating a high curvature in the z direction that increases the curvature trace. Consequently, only a region near the interface of the caplet domain attains C_α. This is similar to observations made in vesicle systems discussed in Chapter IV. On the other side of the interface in the β phase, this low-curvature ring is compensated for with a high-positive curvature region near the interface, as this is preferred by the β phase. As two interfaces of the caplet come together, the curvature of the outer β phase (being pinched between the interfaces) must undergo unfavorable deformation, resulting in a barrier to the caplet forming a ring around the tubule. Thus, the channel of the β phase persists, taking a width that allows it to more easily adopt C_β.

It should be noted that both the 40% α and 50% α cases presented here ceased to run shortly after the final time presented in Figs. 5.6 and 5.7, which could have resulted from the extreme curvature adopted by small domains and/or could be related to the Plateau-Rayleigh instability discussed in the previous section. The spontaneous curvatures used in these two-phase systems, particularly in the system with

50% α, were hypothesized to have a stabilizing effect resulting from their symmetry; however, deformations too extreme to be resolved still occurred. Since both systems ceased to run at approximately the same time, this could suggest that the Plateau-Rayleigh instability contributed to destabilizing the tubules, although it is difficult to draw this conclusion based on only two simulations and more simulations with different random initializations should to be performed to determine the statistical behavior of these systems.

5.4 Conclusions

In this chapter, we presented a preliminary study of the morphological evolution of model tubules. In particular, we focused on how the Plateau-Rayleigh-like pearling instability in membrane tubules could be stabilized or enhanced by the bending energy. For a perturbed single-phase tubule with a spontaneous curvature favoring an unperturbed state, the bending energy was found to stabilize the tubule and smooth the perturbation. Additionally, the control case with no bending energy had only surface tension governing its evolution and was found to be unstable with respect to the perturbation, indicating that the instability observed here was indeed driven by surface tension as it is for the Plateau-Rayleigh instability.

For two-phase tubules with mismatched spontaneous curvatures, we find the following: (i) ring morphologies are preferred for equal mixtures, while caplet morphologies are preferred for nonequal mixtures; (ii) the 50% mixture that leads to ring morphologies (analogous to stripes in nearly planar simulations) coarsens more quickly than the 40% mixture that leads to caplet morphologies; (iii) the rings must generally be formed during the initial stage of phase separation since they are unlikely to form from caplets at later times due to repulsion between interfaces; (iv) the bending energy driving deformations in the tubule destabilizes the interfaces of ring domains, preventing multiple rings from becoming metastable; (v) spontaneous curvatures are best satisfied near domain interfaces; and (vi) the spontaneous curvatures taking values differing from the overall tubule surface curvature with equal magnitude but opposite sign were not sufficient to stabilize the tubule against extreme deformations, which could potentially have been related to the Plateau-Rayleigh instability, although further studies will need to be done to conclude this.

To evaluate these observations experimentally, membrane tubules with nonzero spontaneous curvature would need to be produced, which requires the composition of the membrane to be asymmetric. Methods for producing tubules typically involve drawing them from vesicles by means of micropipette aspiration or in transverse fluid flow, subjecting them to external tensile forces that likely would affect the surface tension. Natural tubules would not necessarily be subject to such forces, and therefore creating tubules using a method that does not require the use of external tensile forces would be ideal. One potential approach is the application of the electroformation technique used to produce lipid vesicles (208). This involves applying an AC field across two conductive glass slides that have been coated with hydrated lipid films. After an hour or so, the hydrated lipid films have been disrupted sufficiently to form vesicles that are attached to the surface of the slide via a lipid tubule. These tubules are not under tension in static conditions. A microscopy technique such as confocal laser scanning microscopy would likely need to be used for visualization of the tubules, since the vesicles would be a large source of background fluorescence. With three-dimensional reconstruction from two-dimensional confocal images, the morphologies and distribution of phases could be evaluated on a large sample of tubules created using electroformation. Additionally, by flowing fluid through the electroformation chamber, the vesicles would drift in the direction of the flow applying tension to the tubules, and therefore the fluid flow could be used to tune the surface tension of the tubules by placing them under a controlled amount of flow, if desired. While we do not have a precise estimate for the tubule diameter, our preliminary experiments

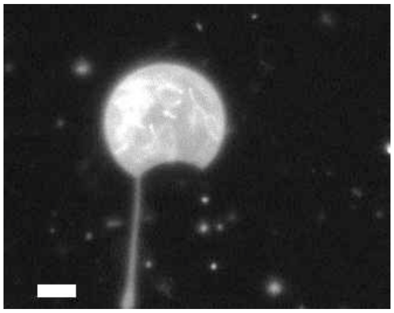

Figure 5.8: An epifluorescence image of a tubule attached to a phase-separated electroformed vesicle that has been harvested (*i.e.* it is no longer tethered to the conductive slide). The scale bar is 10 microns. The image was obtained using an inverted microscope (Nikon Eclipse TE2000-U) at 20x magnification.

using a magnification of 20x (less than the equipment's maximum capability) have shown that tubules formed in this manner may be sufficiently resolved optically, as shown in Fig. 5.8.

CHAPTER VI

Planar Bilayer Membrane Model

6.1 Introduction

As discussed in Chapter I, theoretical and experimental studies have reported that the phase behavior of one leaflet of a lipid bilayer can influence the behavior of the opposing leaflet (84–86). Using asymmetric planar lipid bilayer membranes composed of simple mixtures to mimic the inner and outer leaflets of a cell plasma membrane, is was observed in Ref. 87 that phase separation can be induced in the inner leaflet (or can be suppressed in the outer leaflet), depending on the strength of the tendencies of the leaflets to phase separate (or to remain homogeneous). It has also been observed that in model membranes where both leaflets phase separate, the domains in the two leaflets interact and tend to align laterally (65, 88), as shown in Fig. 6.1. New phases can also arise from the interleaflet interactions, where intermediate phases form near phase boundaries where domains in opposing leaflets cannot perfectly align because they are present in different fractions (87).

This chapter presents a model for planar lipid bilayers, similar to the model presented in Chapter III, but with an important extension. All of the other models presented in this work have considered the two leaflets of the bilayer membrane together as a single entity, with the membrane properties essentially averaged across the entire bilayer so that the membrane is represented as a two-dimensional sheet.

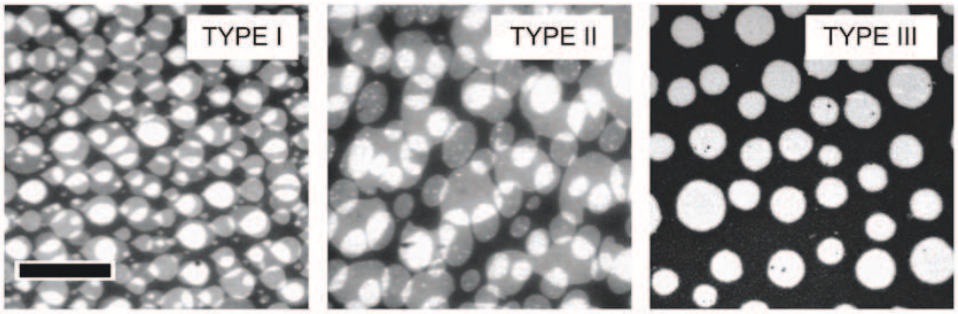

Figure 6.1: A fluorescent micrograph of a supported asymmetric planar bilayer membrane, composed of a 1:1:1 ternary lipid mixture of stearoyloleoylphosphatidylcholine (SOPC), sphingomyelin, and cholesterol, reproduced from Ref. 88. The two leaflets of the bilayer have phase separated to form liquid-ordered and liquid-disordered phases, and the fluorescent dye used in both leaflets is known to partition into the liquid-disordered phase. In the TYPE I case, the bilayer is directly in contact with the solid support, and in the TYPE II and III cases a polymer spacer is used to separate the bilayer from the solid support, with a longer polymer chain used for TYPE III compared with TYPE II. It was found that the mobility in the TYPE I and II bilayers was hindered by the solid support, therefore preventing the phase-separated domains from aligning across the leaflets, creating three fluorescence levels where liquid-disordered domains are present in both, one, or neither leaflet. However, in the TYPE III case, the mobility in the bilayer is unaffected by the solid support, and the domains are observed to precisely register across leaflets, with only two fluorescence levels observed. The scale bar represents 30 μm.

By specifying nonzero spontaneous curvatures, we assumed that the membrane was either a monolayer or an asymmetric bilayer. However, in this chapter we present a planar bilayer model where each leaflet of the membrane is accounted for, and a new term is introduced into the free energy to represent mechanisms that determine how the lipids in the two leaflets communicate and interact across the bilayer. Rather than assigning a separate spontaneous curvature to each monolayer, we compute the composition-dependent spontaneous curvature of the bilayer as a whole based on a simple geometrical model. The leaflets have different compositions, but we specify that both leaflets adopt the same shape profile since they together form a bilayer (*i.e.*, the two leaflets cannot adopt different shapes since they must compose a single, cohesive bilayer structure).

We simulate the evolution of the composition and the shape of asymmetric membranes, governed by a competition between the line-tension, bending, and surface-tension energies, as well as an energy dictating the coupling between the two leaflets of the bilayer. The interleaflet coupling energy represents mechanisms that determine where phases prefer to be situated with respect to the opposing leaflet phases. These mechanisms include the hydrophobic effect, where particular lipid ordering or packing is entropically favored to make a cohesive bilayer (for example, a difference in tailgroup length as in Refs. 124 and 209), as well as hypothesized mechanisms for interleaflet "communication" such as cholesterol flip-flop. Since we are particularly interested in the effects of nonzero spontaneous curvature, we specify that the lipids in the two leaflets interact with each other across the bilayer such that lipid arrangements leading to nonzero spontaneous curvatures are energetically favored over those leading to zero spontaneous curvature.

6.2 Methods: Extending the Planar Membrane Model to Treat Individual Bilayer Leaflets

6.2.1 Bilayer Components in the Phase-Field Model

In this bilayer model each of the two leaftlets are treated individually using two scaled composition variables, ϕ_1 and ϕ_2. Each leaflet is modeled as a ternary system (representing, for example, a saturated lipid, an unsaturated lipid, and cholesterol), with a pseudobinary representation across the phase transformation path of the ternary phase diagram. We model leaflet 1 to be composed of species A and B, while leaflet 2 is composed of species E and F. The α and β phases exist in leaflet 1, rich in components A and B, respectively; the γ and δ phases exist in leaflet 2, rich in components E and F, respectively. A schematic illustration of the shapes of species in the two leaflets is given in Fig. 6.2a. The phase fields in the two leaflets, ϕ_1 and ϕ_2, are related to the concentrations of components A and E by

$$\phi_1 = \frac{c^A - c^A_\beta}{c^A_\alpha - c^A_\beta}, \;\; \phi_2 = \frac{c^E - c^E_\delta}{c^E_\gamma - c^E_\delta}, \tag{6.1}$$

where c^A_α specifies the concentration of species A in the α phase. This defintion dictates that $\phi_1 = 1$ in the α phase and $\phi_1 = 0$ in the β phase, while $\phi_2 = 1$ in the γ phase and $\phi_2 = 0$ in the δ phase. We choose the equilibrium concentrations to be $c^A_\alpha = c^E_\gamma = 0.8$ and $c^A_\beta = c^E_\delta = 0.2$ to approximate the compositions of the liquid-ordered and liquid-disordered phases in ternary membrane systems below their miscibility transition temperature (210).

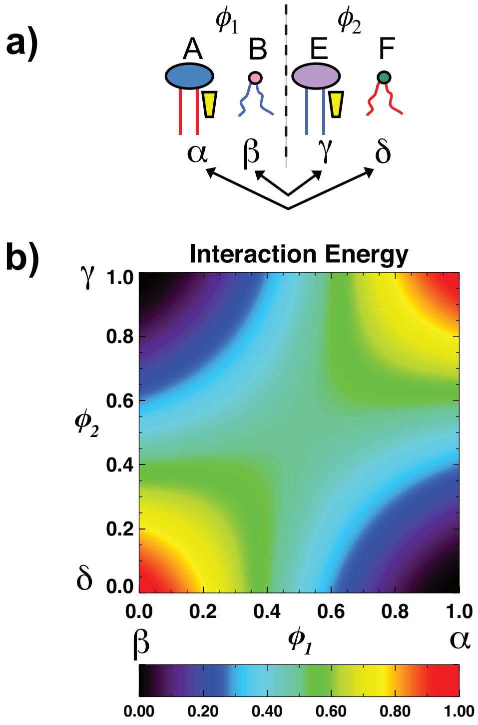

Figure 6.2: (a) Schematics of the molecules composing the two leaflets and the phases that they tend to partition into. The α and γ phases are rich in components A and E, respectively, and the third component that is not explicitly tracked in our pseudobinary model. This third component is illustrated to represent cholesterol, since it largely partitions with saturated lipids (A and E). The tailgroup colors and the arrows indicate which components prefer to interact. (b) The contour plot of H_3, the interleaflet interaction energy, with respect to the compositional phase fields ϕ_1 and ϕ_2. The locations of the minima and maxima determine which phases (represented by the phase-field values) have preferred and non-preferred interactions.

6.2.2 Free Energy

The total free energy in the model is defined by a sum of four terms:

$$F = \int H dA = \int (H_0 + H_1 + H_2 + H_3) dA. \tag{6.2}$$

The first energy density H_0 is the same expression as presented for H_0 in Eq. 3.2, but now describes the thermodynamics of the mixture in each leaflet $p = 1, 2$:

$$H_0 = \sum_{p=1}^{2} \left(\frac{w}{4} \phi_p^2 (1 - \phi_p)^2 + \frac{\zeta^2}{2} \nabla^i \phi_p \nabla_i \phi_p \right). \tag{6.3}$$

As in Chapter III, w defines the barrier height in the double-well free energy and ζ sets the energetic penalty for composition gradients. We use the standard notation of subindices and superindices for contravariant and covariant vectors, respectively, as well as the repeated index summation convention as shown in the notation of the gradient term. These indices identify generalized coordinates that parametrize the surface; refer to Appendix A for detailed expressions for differential operators.

The second energy density is a modified Helfrich Hamiltonian (178) describing the mechanical properties of the membrane, coupling compositions and the membrane shape:

$$H_1 = \frac{\Lambda}{2} (K - C(\phi_1, \phi_2))^2. \tag{6.4}$$

In this expression, Λ is the membrane bending rigidity, K is the trace of the curvature tensor and is equal to twice the mean curvature, and $C(\phi_1, \phi_2)$ is the spontaneous curvature defined as a function of the two compositions in the leaflets, as discussed in the next section.

The third contribution to the energy density controls the total area of the membrane, and is given by a surface tension, just as in Chapter III:

$$H_2 = \sigma. \tag{6.5}$$

Lastly, the fourth term in the free energy, H_3, models the coupling between bilayer leaflets and is a function of the two leaflet compositions, scaled with the coupling strength, χ:

$$H_3 = \frac{\chi}{2}\big((\phi_1 + \phi_2 - 1)^2 + ((\phi_1 - \phi_2)^2 - 1)^2\big) \tag{6.6}$$

A contour plot of H_3 in (ϕ_1, ϕ_2) space is presented in Fig. 6.2b, where the locations of valleys determine which phases prefer to align across the two leaflets of the bilayer. As schematically indicated by the arrows in Fig. 6.2a, the phases that prefer to colocate across the leaflets as defined by H_3 are rich in species with different headgroup sizes, which produces nonzero spontaneous curvatures. The magnitude of χ determines how strong the coupling between leaflets is, with larger values imposing greater energetic penalties for non-preferred interactions across the leaflets.

6.2.3 Relating Composition to Spontaneous Curvature

The spontaneous curvature appearing in the free energy contribution H_1 is defined as a function of the compositions in each leaflet. Since the spontaneous curvature is a property stemming from the shapes of the lipid molecules in the two leaflets, we introduce an intermediate variable in each leaflet: the effective headgroup diameter of the lipid species, denoted as D. This variable is taken to be a function of the local composition, and relates the spontaneous curvature to composition through the following geometrical model.

For simplicity, it is assumed that components A and E are similar to each other in geometry, as are B and F (but different from A and E) as illustrated in Fig. 6.2a. In leaflet 1 at equilibrium, the α phase is rich in species A, while the β phase is rich in species B. Similarly, in leaflet 2 at equilibrium, the γ phase is rich in species E, while the δ phase is rich in species F. The effective headgroup diameter in the α and γ phases is denoted as $d_{\alpha,\gamma}$ and similarly in the β and δ phases as $d_{\beta,\delta}$, with $d_{\alpha,\gamma} > d_{\beta,\delta}$. The function $D_p(\phi_p)$ for each leaflet, $p = 1$ or 2, is defined to smoothly interpolate between its local maximum at $D_p(\phi_p = 1) = d_{\alpha,\gamma}$ and local minimum at $D_p(\phi_p = 0) = d_{\beta,\delta}$ using an interpolation function of the form $f(x) = a(x^2(3 - 2x)) + b$ that ensures that the interpolated value slowly approaches $f(x = 0)$ and $f(x = 1)$ (where the derivative vanishes) and rapidly changes away from these values. Specifically,

$$D_p(\phi_p) = (d_{\alpha,\gamma} - d_{\beta,\delta})(\phi_p^2(3 - 2\phi_p)) + d_{\beta,\delta}. \tag{6.7}$$

We note that in some simulations, the minimum and maximum values of the composition variables ϕ_1 and ϕ_2 reach values outside of $[0, 1]$ by as much as ± 0.25, corresponding to concentrations of c^A, $c^E = 0.05$ and 0.95. This produces an error in the function $D_p(\phi_p)$ of up to 5%, and therefore test simulations were performed for cases with extreme values of ϕ_p where both ϕ_1 and ϕ_2 were truncated at $[0, 1]$ for spontaneous curvature calculations. These tests produced results nearly identical in terms of dynamic and equilibrium phase morphologies to the results presented.

Finally, the spontaneous curvature function, $C(\phi_1, \phi_2)$, can be defined as a function of D in each leaflet, $C(D_1(\phi_1), D_2(\phi_2))$. Using a simple geometric argument based on similar triangles, as illustrated in Fig. 6.3, C is related to the headgroup diameter and the bilayer thickness L by

$$C(D) = \frac{2}{L}\frac{D_1 - D_2}{D_1 + D_2}. \tag{6.8}$$

To examine the particular effects of nonzero spontaneous curvature, the interaction energy H_3 is set such that the α phase prefers to interact with δ and the β phase prefers γ, as indicated by the arrows in Fig. 6.2a. When α is aligned with δ, we define

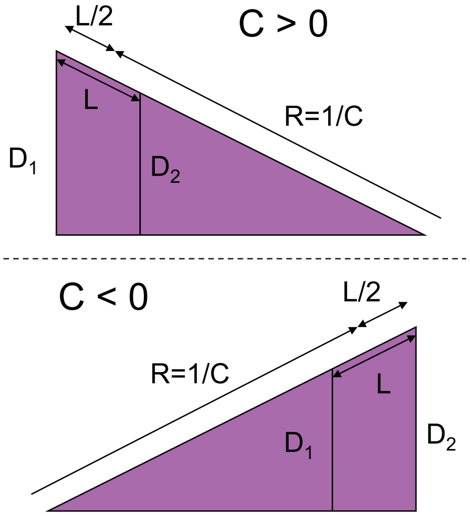

Figure 6.3: Illustration of the simple geometric argument based on similar triangles used to relate headgroup diameters in the two leaflets D_i, $i = 1, 2$, with spontaneous curvature C. L is the bilayer thickness, and R is the radius of curvature equal to the inverse of the spontaneous curvature. Positive curvatures are produced when $D_1 > D_2$, and negative curvatures are produced when $D_2 > D_1$.

that $C = 1$; when β is aligned with γ, we define that $C = -1$. If α is aligned with γ or if β is aligned with δ, the bilayer is symmetric with respect to molecular shapes, and these configurations are therefore assigned to have $C = 0$. These configurations are illustrated in Fig. 6.4. Spontaneous curvature values of $C = 1$ and $C = -1$ represent curvatures of 20 nm^{-1} and -20 nm^{-1}, respectively, with a bilayer thickness of $L = 3.6$ nm (211, 212). The headgroup diameters $d_{\alpha,\gamma}$ and $d_{\beta,\delta}$ are representative of a generic system with mismatched lipid headgroup sizes, rather than tuned to a specific system of lipids.

6.2.4 Compositional Dynamics

The two leaflets of the membrane are assumed to maintain a constant separation distance even during deformations, and therefore the membrane possesses only a single shape adopted by the two leaflets together. Thus, the shape dynamics scheme

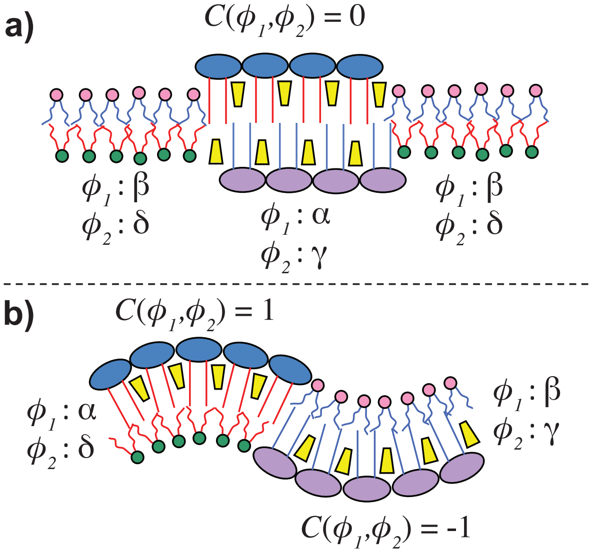

Figure 6.4: Bilayer configurations and their spontaneous curvatures. The interaction energy H_3 specifies that the configuration shown in (a) with zero spontaneous curvature is higher in energy than that in (b) with nonzero spontaneous curvature. The schematics illustrate how, as a result of the different lengths of the tailgroups in the phases, hydrophobic forces could favor the configurations in (b) over (a) since the bilayer is more cohesive.

described for the nearly planar model in Chapter III is directly applied in this model. Similar to the dynamics in Chapter III, we use a Cahn-Hilliard-type expression for the dynamics for the composition of each leaflet denoted by $p = 1, 2$, where $\mu_p = \delta F/\delta\phi_p$ is the chemical potential for the dimensionless composition, ϕ_p, of leaflet p. The dynamics is described by an evolution equation,

$$\begin{aligned}
\frac{\partial \phi_p}{\partial t} &= M\nabla^2\mu_p, && (6.9)\\
\mu_1 &= \frac{w}{2}\phi_1(1-\phi_1)(1-2\phi_1) - \zeta^2\nabla^2\phi_1 + \Lambda\frac{\delta C}{\delta\phi_1}(C(\phi_1,\phi_2)-K) && (6.10)\\
&\quad +\chi\big(\phi_1+\phi_2-1+2((\phi_1-\phi_2)^2-1)(\phi_1-\phi_2)\big), &&\\
\mu_2 &= \frac{w}{2}\phi_2(1-\phi_2)(1-2\phi_2) - \zeta^2\nabla^2\phi_2 + \Lambda\frac{\delta C}{\delta\phi_2}(C(\phi_1,\phi_2)-K) && (6.11)\\
&\quad +\chi\big(\phi_1+\phi_2-1-2((\phi_1-\phi_2)^2-1)(\phi_1-\phi_2)\big), &&
\end{aligned}$$

where

$$\begin{aligned}
\frac{\delta C}{\delta\phi_1} &= \frac{2}{L}\frac{dD_1}{d\phi_1}\left(\frac{1}{D_1+D_2} - D_1(D_1+D_2)\right), && (6.12)\\
\frac{\delta C}{\delta\phi_2} &= \frac{2}{L}\frac{dD_2}{d\phi_2}\left(\frac{1}{D_1+D_2} - D_2(D_1+D_2)\right). && (6.13)
\end{aligned}$$

Note that D_1 and D_2 are functions of ϕ_1 and ϕ_2, respectively.

6.3 Results

By scaling arguments, when the coupling constant χ is set to a value of 1, the magnitude of the coupling energy in Eq. (6.6) is comparable to the magnitude of the bending energy in Eq. (6.4). Simulations were performed for χ = 1, 10, and 20. To illustrate the effect of interleaflet interactions on the morphologies of bilayer systems, we have constructed phase diagrams that map equilibrium morphological phases for three different values of the coupling strength χ, presented in Fig. 6.5. Each phase diagram is plotted in composition space, with the percentage of the α phase in leaflet 1 along the x-axis and the percentage of the γ phase in leaflet 2 along the y-axis, both in intervals of 10%. Simulations were performed at compositions along and below the diagonal running from $(\%\alpha, \%\gamma) = (0, 0)$ to $(100, 100)$, which we will refer to as the minor diagonal. The line running from $(\%\alpha, \%\gamma) = (0, 100)$ to $(100, 0)$ will be referred to as the major diagonal. Since the system is symmetric about the minor diagonal, the simulation results are reflected onto the region above the minor diagonal, and these patches are indicated with a dot pattern over the color. The term "overall composition" will be used throughout this discussion, and is defined as the total fraction of the entire bilayer occupied by the pair of preferentially interacting phases, α and δ. For example, a system composed of 20% α (80% β) and 60% γ (40% δ) has an "overall composition" of $(20\% + 40\%)/2 = 30\%$. A system with an "overall composition" of 50% is termed an "overall equal" mixture, while a system with an "overall composition" of 0% or 100% is termed an "overall pure" mixture.

Most of the square patches in the phase diagrams represent a single simulation result, and each of these simulations was initialized using the same random seed referred to as the standard random seed. The color of each patch is determined by the result from the simulation using the standard random seed. However, for certain compositions, four simulations were performed, each initialized with a different random seed. These patches are additionally marked with a number indicating how many of those four simulations produced the same result as the one initialized with the standard random seed. For example, a dark blue patch with a number '3' indicates that the standard random seed simulation equilibrated to caplets in both leaflets, and three of four of the simulations initialized with different random seeds also equilibrated to caplets in both leaflets. If a number less than four is on a patch colored to indicate caplets (dark blue), the other morphology observed was stripes, and if a number less than four is on a patch colored to indicate stripes (red), the other morphology

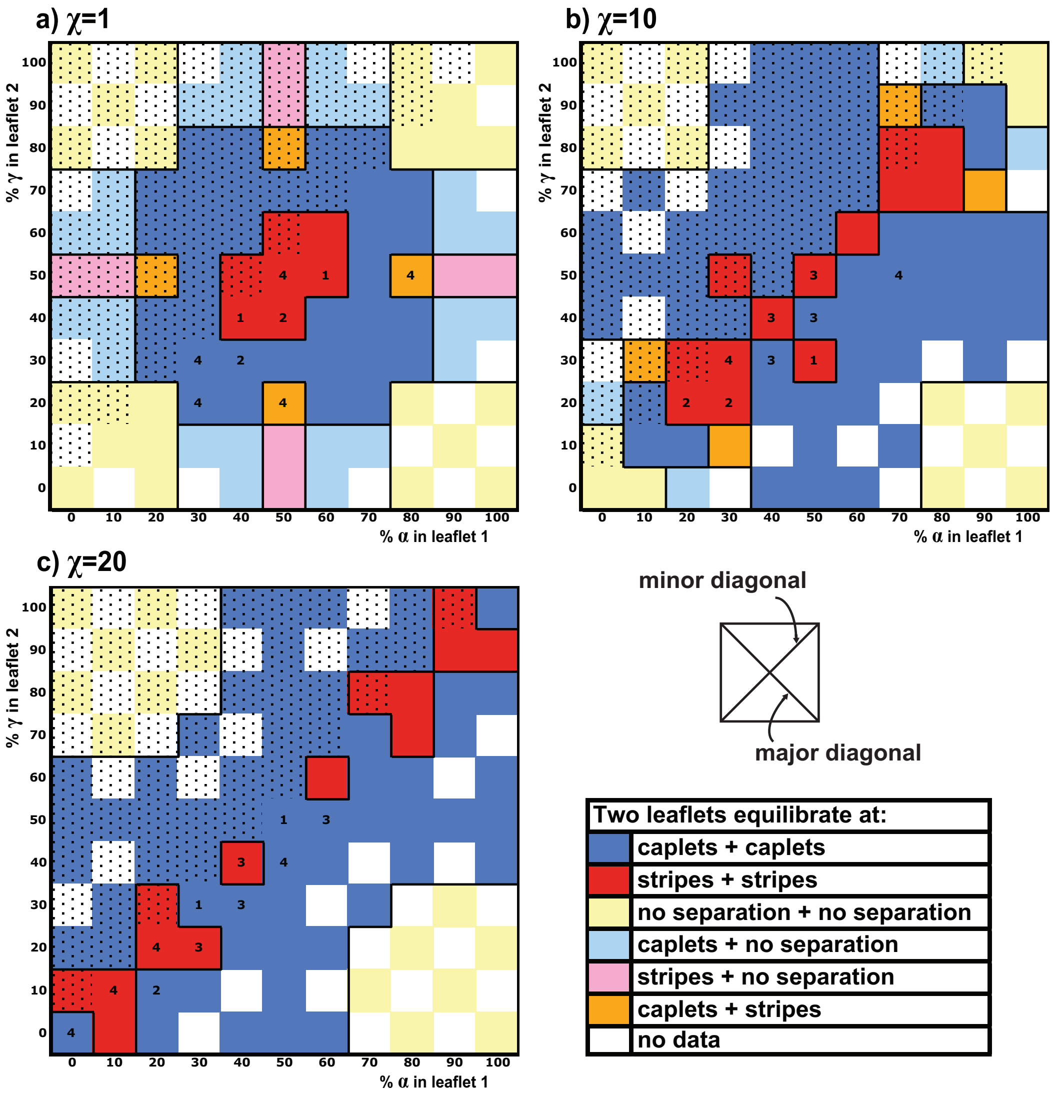

Figure 6.5: Morphological phase diagrams for bilayer systems at three different interleaflet coupling strengths (weakest to strongest): (a) $\chi = 1$, (b) $\chi = 10$, and (c) $\chi = 20$. Each colored square patch along and below the minor diagonal represents a simulation result; simulation results are copied to the top half (patches shown with a dot pattern). In the legend, "no separation" means the leaflet did not phase separate. The numbers indicate concentrations where four simulations using different random initializations were run; the number indicates how many of these four simulations equilibrated in the morphology represented by the color of the patch (either caplets or stripes in both leaflets).

observed was caplets.

The phase diagrams in Fig. 6.5 are generally symmetric about the major diagonal as well as the minor diagonal, although this is not as clear on the $\chi = 10$ diagram in Fig. 6.5b. This is because in the region in the center of the diagram, extending out along the minor diagonal, equilibrium morphologies were found to be sensitive to initial conditions, where different random seeds in the initialization would lead to different equilibria, some of which are local, not global, equilibria. In each of these simulations, either caplets or stripes were observed in equilibrium. Where a patch shows a '4', that set of concentrations was not sensitive to initial conditions and the color is representative of the observed single morphology. On the other hand, where a patch shows a '3', three out of four different seeds produced the same (dominant) morphology as the one observed with the standard seed. A patch showing a '1' is similar, with three out of four seeds producing the same result, with the standard seed producing a different result. The patch at $\chi = 10$ and $(\%\alpha, \%\gamma) = (50, 30)$ is marked with a '1', which is the only patch that breaks the symmetry across the major diagonal. Therefore, in a representation showing the dominant morphologies, the diagrams would all appear symmetric about both diagonals. Other patches that show a '1' run along the minor diagonal in the $\chi = 20$ case, where stripes was the dominant morphology almost the entire length of the diagonal (excluding the corner patches).

Similarities across the different coupling strengths, as observed from the diagrams in Fig. 6.5, include (i) the diagrams are generally symmetric about the major diagonal as well as the minor diagonal, (ii) the stripe morphology is favored when the compositions of both leaflets are near equal mixtures ($(\%\alpha, \%\gamma) \approx (50, 50)$), and (iii) no phase separation occurs when the bilayer is an "overall (nearly) pure" mixture. These results are expected based on thermodynamic considerations.

However, there are also numerous differences in the results at the different coupling strengths. First, we find that stronger coupling tends to favor the stripe morphology along the length of the minor diagonal, rather than just in the center of composition space. For systems where phases have equal but oppositely signed spontaneous curvatures, in the absence of interleaflet coupling, roughly equal mixtures tend to form a stripe morphology while mixtures far from 50% tend to form a caplet morphology (179). An important characteristic of the systems along the minor diagonal is that they are "overall equal" mixtures. With strong coupling, the "overall composition" has a greater effect, and an "overall equal" mixture system behaves like a simple two-phase equal mixture system where the phases have mismatched spontaneous curvatures and a stripe morphology is favored.

The tendencies of "overall equal" mixtures (or nearly "overall equal" mixtures) to form stripes can be further understood by the detailed observation of the dynamics of the morphological evolution. When the coupling constant is larger and thus phases with preferred interactions have a stronger driving force to coincide, there are two main consequences. The first is that stronger coupling drives the system to phase separate more quickly, with sharper (yet resolved) interfaces, as well as more precisely aligned domains. These can be observed by comparing the series of snapshots presented in Figs. 6.6 and 6.7. The second consequence of stronger coupling is that the bulk phase values of ϕ_1 and ϕ_2 shift to accommodate the stronger driving force. Since the average values of ϕ_1 and ϕ_2 remain fixed to conserve mass, the shift in bulk phase compositions is balanced by changes in the fractions of the phases. For example, consider a system with stronger coupling ($\chi = 20$) initialized with 80% α phase ($\phi_{1,avg} = 0.8$ and 20% β) and 70% γ phase ($\phi_{2,avg} = 0.7$ and 30% δ). Since the α and δ phases are present in significantly different amounts yet have a strong driving force to align, the bulk phase value for α and γ shifts in both leaflets from $\phi_{1,2} = 1$ to $\phi_{1,2} = 1.19$, forming α' and γ' phases, and for β and δ this value shifts in both leaflets from $\phi_{1,2} = 0$ to $\phi_{1,2} = 0.25$, forming β' and δ' phases. To conserve mass and maintain the average composition values of $\phi_{1,avg} = 0.8$ and $\phi_{2,avg} = 0.7$, the relative amounts of the phases shift toward 0.5. We observe in equilibrium the α' phase present at 58.5% (defined with $\phi_1 = 1.19$) and the δ' phase present at 41.5% (defined with $\phi_2 = 0.25$). These altered phase fraction values are then close enough to equal mixtures that stripes are observed in equilibrium, even though the initial phase fractions were far from equal mixtures. This observation of shifting equilibrium phase compositions is similar to the phenomenon observed in asymmetric bilayers in Ref. 87, where distinct new phases appear in a phase-separated leaflet that would not be present if the opposing leaflet were absent (*i.e.*, in a monolayer system). Our simulation results provide evidence that such observations can be explained by the contribution of interleaflet interactions to the thermodynamics of the bilayer system.

Second, we find that stronger coupling favors phase separation for composition sets at the extremes of the minor diagonal, where the systems are "overall equal" mixtures but the individual leaflets are nearly pure mixtures. With weaker coupling, the "overall composition" has a smaller effect than the individual leaflet compositions. Since there is less tendency toward spontaneous phase separation (spinodal decomposition) for nearly pure mixtures in general, the composition sets at the extremes of the minor diagonal are only driven to phase separate with strong interleaflet coupling. This can be contrasted to regions at the extremes of the major diagonal, where phase separation is not observed at any coupling strength, since the "overall composition" and individual leaflet compositions are both nearly pure mixtures.

Lastly, we observe that stronger coupling drives both leaflets of the bilayer to adopt the same phase morphologies, as the $\chi = 20$ diagram in Fig. 6.5c is composed entirely of such states, whereas the $\chi = 1$ diagram in Fig. 6.5a shows roughly one-quarter of the composition space exhibiting phase morphologies where the two leaflets differ. Figure 6.8 presents a series of snapshots for one of the cases with $\chi = 1$, where, in equilibrium, one leaflet has adopted a caplet phase morphology while the other has

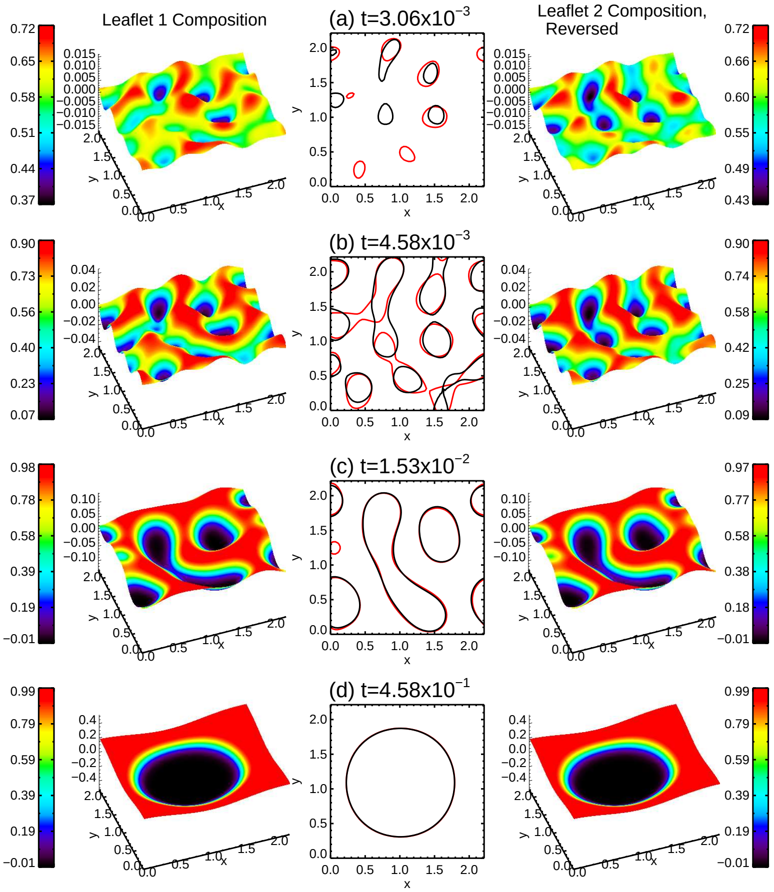

Figure 6.6: Surface morphologies colored to represent the composition of a bilayer system with $\chi = 1$ and $(\%\alpha, \%\gamma) = (60, 40)$. The far left and right columns represent leaflet 1 (ϕ_1) and leaflet 2 (plotted as $1 - \phi_2$), respectively, while the center column displays contours at the phase boundaries in both leaflets to better visualize domain alignment. From top to bottom, (a) $t = 3.06 \times 10^{-3}$, (b) $t = 4.58 \times 10^{-3}$, (c) $t = 1.53 \times 10^{-2}$, and (d) $t = 4.58 \times 10^{-1}$. At early times, domains align across leaflets only roughly, but by the time equilibrium is reached they are aligned nearly precisely. This is in contrast to the system with relatively stronger coupling in Fig. 6.7.

adopted a stripe morphology (Fig. 6.8d). The resulting shape of the membrane in Fig. 6.8d is neither a caplet nor ripple, but rather a combination of the two.

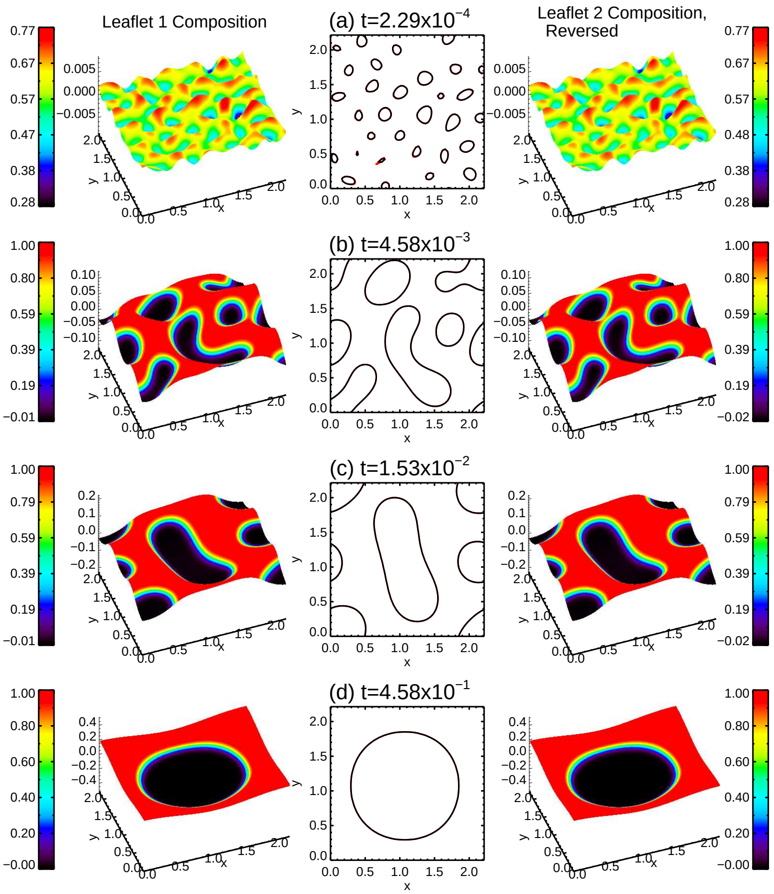

Figure 6.7: Similar to Fig. 6.6, but for a bilayer system with $\chi = 20$ and $(\%\alpha, \%\gamma) = (60, 40)$, from top to bottom, (a) $t = 2.29 \times 10^{-4}$, (b) $t = 4.58 \times 10^{-3}$, (c) $t = 1.53 \times 10^{-2}$, and (d) $t = 4.58 \times 10^{-1}$. Even at early times, domains align across leaflets quite precisely as a result of the strong coupling between leaflets. This is in contrast to the system with relatively weak coupling in Fig. 6.6. Note that the earliest time shown here in part (a) is significantly earlier than the earliest time in Fig. 6.6a, to further emphasize that the stronger coupling not only induces phase separation more quickly, but also aligns interfaces very quickly.

6.4 Discussion and Conclusions

We have presented a phase-field model for lipid bilayer membranes that couples the compositions of the two leaflets with the deformation of the membrane. We specifically examined the effects of interleaflet interactions in systems where nonzero spontaneous curvatures are energetically favorable, investigating the interplay between the

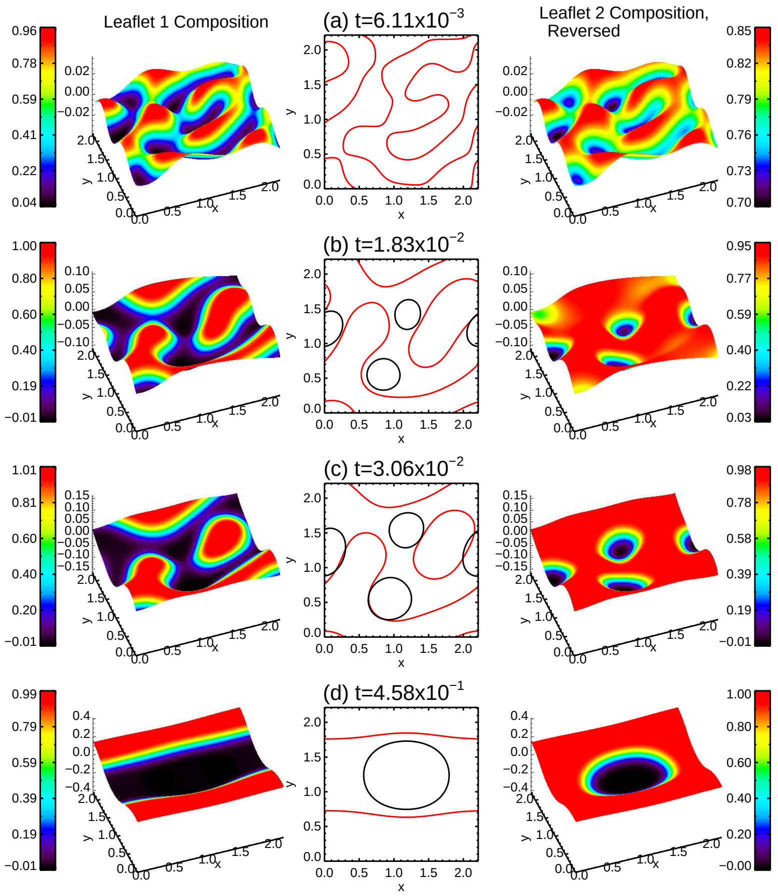

Figure 6.8: Similar to Fig. 6.6, but for a bilayer system with $\chi = 1$ and $(\%\alpha, \%\gamma) = (50, 20)$, from top to bottom, (a) $t = 6.11 \times 10^{-3}$, (b) $t = 1.83 \times 10^{-2}$, (c) $t = 3.06 \times 10^{-2}$, and (d) $t = 4.58 \times 10^{-1}$. This case represents one of the cases where the two leaflets adopt different morphologies in equilibrium, even though they must have the same height profile. The center plot in part (a) does not display any black interfaces since at that time leaflet 2 has not yet fully phase separated to have the interfacial value of 0.5.

compositions of each leaflet and the shape of the membrane. By mapping and contrasting phase diagrams as the interleaflet coupling strength increases, we have found that the dynamics of phase separation and equilibrium morphologies increasingly depend on a key parameter: an "overall composition," defined as the total fraction of the bilayer occupied by two phases that prefer to interact across the leaflets. We have found aspects of these bilayer systems that are robust and sensitive with respect to the strength of the coupling. Characteristics that are robust with varying coupling strength include (i) no spontaneous phase separation occurs in systems that are "overall (nearly) pure" mixtures, and (ii) the stripe morphology is favored when both leaflets are composed of (nearly) equal mixtures. On the other hand, when comparing systems with weak coupling to those with stronger coupling we find that as the interleaflet coupling strength increases (i) the compositions of the bulk phases and their relative amounts are increasingly altered to accommodate preferred phase alignment across leaflets, demonstrating that the strongly coupled leaflets of the bilayer form a system that appears completely different from a system with the same composition but two uncoupled monolayers; (ii) the stripe morphology is increasingly preferred; (iii) the phases with preferred interleaflet interactions align faster and more precisely; (iv) phase separation occurs more quickly; and (v) the two leaflets are more likely to adopt the same phase morphology in equilibrium. These observations indicate that as the degree of interleaflet coupling varies, membrane phase and morphological behavior vary also.

These findings could be investigated experimentally using asymmetric planar lipid bilayers composed of lipids selected for particular geometric properties, such that they would resemble the lipid schematics in Fig. 6.2a. Geometric properties have been reported for various lipid species, including spontaneous curvatures, as well as how membrane curvature can be tailored with particular lipid compositions (7, 64, 213–215). The lipids would also need to be selected such that they would interact across the leaflets to provide a coupling energy landscape similar to that in Fig. 6.2b, which could be accomplished with lipids of varying headgroup size and tailgroup length. The strength of the coupling could perhaps be varied by changing the length of the tailgroups, which would alter the degree of interdigitation and likely the strength of the interleaflet coupling.

CHAPTER VII

Conclusions and Future Work

7.1 Conclusions, Implications, and Potential Applications

In this work, we have investigated phase separation in multicomponent lipid membranes using a computational model with various background geometries. In this model, composition is coupled with the mechanical properties of the lipid phases, and the membrane is allowed to deform. The evolution of the composition and shape are governed by a competition between different energetic contributions from the line tension between phases, bending energy from the mechanical properties of those phases, and surface tension from the hydrophobic forces driving the lipids to form a continuous membrane. These are implemented in three different overall geometries: a planar geometry to model nearly planar portions of membranes (Chapter III), a spherical geometry to model vesicles (Chapter IV), and a cylindrical geometry to model tubules (Chapter V). Additionally, the nearly planar model was extended to include interleaflet interactions, treating both leaflets of the lipid bilayer separately with an additional energetic contribution to model the coupling of the leaflets (Chapter VI).

The overall aim of this work was to develop an understanding of the thermodynamics and kinetics involved in phase-separating lipid membrane systems. More specifically, we investigated how the lipid composition can affect the morphology of the membrane and vice versa, and found that these two attributes are intimately related. We observed that membrane shapes are correlated with phase morphologies; for example, bulges are induced by caplet phase morphologies in all three membrane geometries investigated, and ripples are induced by stripe phase morphologies in planar and cylindrical geometries. Different membrane morphologies were observed at different interleaflet coupling strengths. This was attributed to the shift in phase compositions induced by the coupling energy, the degree of which depends on the coupling strength. This in turn changed the effective area fraction of the phases and altered the shape of the membrane. With stronger coupling, a stripe phase morphology and ripples in the shape resulted, instead of caplet morphologies that formed without such a strong coupling. We also observed the shape of the membrane affecting the locations different phases preferred to occupy and their morphologies relative to each other. In the planar geometry, a rigid patterned surface was able to induce a stripe phase morphology to form in a system with parameters that, on a non-patterned surface, did not produce stripes. In the spherical and cylindrical models, domains bulging away from the membrane surface were in some systems prevented from coalescing (as well as self-coalescence to form rings in the cylindrical model), with coarsening proceeding through diffusion only and therefore occurring on much longer time scales than when domains did not bulge. In vesicle systems that either evolved to or were initialized with elongated shapes, configurations with enhanced stability having more than one domain of a phase were observed, where the system was able to reduce its bending energy at the expense of line-tension energy, which would otherwise drive the system to form a single domain of each phase.

With the findings that membrane composition and shape are interrelated to such a degree, it is important that they both be examined and considered when proposing models to explain observed phenomena when studying the behavior of multicomponent lipid membranes. The location, organization, and function of many membrane proteins have been linked to the local lipid environment, which interacts with the protein via hydrophobic and mechanical forces. Not only do these findings have implications for studying cell biology, but also in areas of biotechnology. This relationship between membrane phases and shapes could be exploited for use in biosensors, where detection of a substance of interest could cause a change in the behavior of lipid phases, which could then cause the membrane to change shape as the indication. The finding that the arrangement of lipid phases can be directed using patterned surfaces could be of use for functionalized surfaces, where different molecules can be attached to the lipids, which can be rearranged as the system mixes and phase separates at different temperatures, for example. Using vesicles for targeted drug delivery could also take advantage of the findings here, where the morphology of vesicles could be tuned by forming them from a lipid mixture that phase separates and deforms the vesicle in a particular way, making its uptake in different cells variable.

While some of the findings reported in this work have been produced in experiments to varying degrees, many have not. Various properties of some lipid molecules such as cross-sectional area and packing preferences have been reported in the literature. Therefore, in theory lipid compositions could be selected to produce phases that have specified properties such as bending rigidity and spontaneous curvature, and established microscopy methods can be used to observe their static and dynamic behavior. However, there are some barriers to performing such experiments currently. First, spontaneous curvature has been measured for some lipids, but it is generally not established for lipid mixtures. Furthermore, even if spontaneous curvatures could be established for some particular mixtures, a theoretical relationship needs to be elucidated so that the mechanical properties of the phases formed in a mixture could be determined from the relative amounts and spontaneous curvature and packing preference of individual lipids. It has been observed in experiments that different membrane morphologies can be achieved by utilizing different lipid mixtures, but the results were more qualitative than quantitative. Second, the majority of experiments performed to investigate the behavior of lipid phases are done using symmetric bilayers, while natural membranes are asymmetric. The spontaneous curvature and interleaflet interactions studied here require asymmetric bilayers, introducing numerous effects present in natural membranes but absent from the model membranes studied in many investigations in the past. Methods are well established for the synthesis of asymmetric planar bilayers, but are less established for producing vesicles and tubules with asymmetric composition.

In summary, this work has contributed to the knowledge of the biophysics of multicomponent lipid membranes, the ubiquitous cellular structures that interact closely with the protein machinery of the cell, and have great potential for application in numerous biotechnology settings.

7.2 Future Work

Future work can be divided into two categories: performing further investigations using the models as presented, and implementing extensions to the models to better represent the physics governing lipid membranes. Since the liquid-ordered phase has been found to be more rigid than that liquid-disordered phase, more extensive investigations into systems with different bending rigidities should be performed using each of the models presented. In the nearly planar (bilayer) model in particular, different and more complexly patterned surfaces should be modeled, similar to the fixed ripple substrate presented in this work, in order to further investigate the possibilities of lipid phase self-assembly. In the vesicle model, the effects of internal pressure should be investigated, to model osmotic effects that are often included in experimental work. The tubule model is the most recently developed model presented, and many future studies could be performed, including linear stability analysis accounting for the effects of spontaneous curvature, further work investigating different combinations of bending rigidities and spontaneous curvatures in their relation to the stabilization of the pearling instability, and varying the radius of the tubule in space and/or time to mimic the pulling of membrane tethers in micropipette aspiration experiments in order to see how domains rearrange in response.

There are numerous aspects of membrane systems that contribute to the compositional and shape dynamics that could be incorporated into the model in future iterations. These include implementing the bilayer method into the spherical and cylindrical geometry models in order to treat interleaflet interactions in vesicle and tubule systems, respectively. Additional effects stemming from the difference in the areas of the inner and outer leaflet would need to be included also, which can contribute to spontaneous curvature in tubules and small vesicles. Hydrodynamic flows would be an important aspect in any of the geometries studied, where effects of the solvent are included, which can affect the dynamics. Experimental work has found that diffusion coefficients are significantly different in the liquid-ordered and liquid-disordered phases, and the constant mobility that has been used in this work so far could be modified to have a compositional dependence to better reflect this observation. Finally, interleaflet flip-flop of lipids that affects the local and overall compositions of the leaflets has been hypothesized as a mechanism that prevents coarsening in plasma membranes, and could be implemented in the bilayer model.

APPENDICES

APPENDIX A

Geometric Invariants and Difference Operators in the Monge Gauge

As shown in Figs. 3.2 and 4.2, the we use the Monge gauge to describe a surface one-to-one from a reference surface, being a plane, sphere, or cylinder for the nearly planar, vesicle, and tubule models, respectively. All geometric invariants, vectors, tensors, and differential operators can be explicitly written as functions and operators acting in the reference surface, and their expressions in a form general enough to apply to any of the three geometries considered in this work are presented in this appendix, similarly to the presentation for the nearly planar case in our work in Ref. 177.

We define a number of objects that reflect the geometric properties of the surface. These objects are vectors and tensors based on the two-dimensional space tangent to the surface. Vector quantities appear in bold face, vector components are written within square brackets, and unit vectors are denoted with hats. Tensors and vectors within the surface are identified by their explicit indices. For example, the metric tensor, g_{ij}, is a rank-two tensor in the tangent space, and each of its indices takes only the values 1 and 2. Note that we use mixed objects, such as the basis pair $\mathbf{e}_i = [\mathbf{e}_1, \mathbf{e}_2]$. Each entry is a vector in three-dimensional space, but the pair behaves as a vector within the surface and consists of two vectors, and as such, is identified by

Table A.1: Summary of the basic geometrical setup for each of the three models presented in the body of this work.

Model	Coordinate System	Reference Geometry	Indices 1, 2	3D Position Vector	Unit Vectors in Reference Surface
Nearly planar	Cartesian	plane	x, y	$\mathbf{x} = [u_1, u_2, h(u_1, u_2)]$ $= [u_x, u_y, h(u_x, u_y)]$	$\hat{\mathbf{w}}_1 = \hat{\mathbf{w}}_x = \partial\mathbf{x}/\partial x$, $\hat{\mathbf{w}}_2 = \hat{\mathbf{w}}_y = \partial\mathbf{x}/\partial y$
Vesicle	spherical	sphere	θ, ξ	$\mathbf{r} = [u_1, u_2, r(u_1, u_2)]$ $= [u_\theta, u_\xi, r(u_\theta, u_\xi)]$	$\hat{\mathbf{w}}_1 = \hat{\mathbf{w}}_\theta = (\partial\mathbf{r}/\partial\theta)/r$, $\hat{\mathbf{w}}_2 =$ $\hat{\mathbf{w}}_\xi = (\partial\mathbf{r}/\partial\xi)/(r\cos\theta)$
Tubule	cylindrical	cylinder	θ, z	$\mathbf{r} = [u_1, u_2, r(u_1, u_2)]$ $= [u_\theta, u_z, r(u_\theta, u_z)]$	$\hat{\mathbf{w}}_1 = \hat{\mathbf{w}}_\theta = (\partial\mathbf{r}/\partial\theta)/r$, $\hat{\mathbf{w}}_2 = \hat{\mathbf{w}}_z = \partial\mathbf{r}/\partial z$

its index i. Table A.1 summarizes the basic geometric properties of the three different system configurations studied, along with more precise definitions of the index i for each context. The expressions for the basis pairs for the three geometries studied are presented within the chapters they are used in.

The magnitudes and inner products of the vectors $\mathbf{e}_i$ form the metric tensor $g_{ij} = \mathbf{e}_i \cdot \mathbf{e}_j$. Its components are

$$g_{ij} = \begin{pmatrix} \mathbf{e}_1\cdot\mathbf{e}_1 & \mathbf{e}_1\cdot\mathbf{e}_2 \\ \mathbf{e}_2\cdot\mathbf{e}_1 & \mathbf{e}_2\cdot\mathbf{e}_2 \end{pmatrix}. \tag{A.1}$$

The determinant of the metric tensor is denoted by g, and is equal to the square of the surface metric factor.

The matrix inverse g^{ij} of the metric tensor g_{ij} is used to raise indices of vectors and tensors in the standard manner. Its components are

$$g^{ij} = \frac{1}{g}\begin{pmatrix} \mathbf{e}_2\cdot\mathbf{e}_2 & -\mathbf{e}_1\cdot\mathbf{e}_2 \\ -\mathbf{e}_2\cdot\mathbf{e}_1 & \mathbf{e}_1\cdot\mathbf{e}_1 \end{pmatrix}. \tag{A.2}$$

The unit vector normal to the surface $\hat{\mathbf{n}}$ is obtained by the normalized cross product:

$$\hat{\mathbf{n}} = \frac{\mathbf{e}_1 \times \mathbf{e}_2}{|\mathbf{e}_1 \times \mathbf{e}_2|}. \tag{A.3}$$

The curvature tensor K_{ij} is defined as the projection along the normal $\hat{\mathbf{n}}$ of the derivative of the vector $\mathbf{e}_j$ in the i direction:

$$K_{ij} = -\begin{pmatrix} \hat{\mathbf{n}}\cdot\partial_1\mathbf{e}_1 & \hat{\mathbf{n}}\cdot\partial_1\mathbf{e}_2 \\ \hat{\mathbf{n}}\cdot\partial_2\mathbf{e}_1 & \hat{\mathbf{n}}\cdot\partial_2\mathbf{e}_2 \end{pmatrix}. \tag{A.4}$$

We obtain the two invariants of this tensor, its covariant trace and determinant. The curvature trace, equal to twice the mean curvature, is given by

$$K = g^{ij}K_{ij} = g^{11}K_{11} + g^{12}K_{12} + g^{21}K_{21} + g^{22}K_{22}. \tag{A.5}$$

The determinant of the tensor gives the scalar curvature R, and the Gaussian curvature G, as

$$G = R/2 = K^2 - K^{ij}K_{ij} = K^2 - K^{11}K_{11} + K^{12}K_{12} + K^{21}K_{21} + K^{22}K_{22}. \tag{A.6}$$

We use several differential operators. A basic quantity is the gradient $\nabla_i f$ of a scalar function f. Its components are

$$\nabla_i f = [\partial_1 f, \partial_2 f]. \tag{A.7}$$

Note that this vector is attached to the surface and is specified by just two components. Energy terms of free energy functionals typically involve the magnitude of this vector, $\nabla^i f \nabla_i f = g^{ij}\nabla_i f \nabla_j f$. We obtain

$$\nabla^i f \nabla_i f = g^{11}(\partial_1 f)^2 + g^{12}(\partial_1 f)(\partial_2 f) + g^{21}(\partial_2 f)(\partial_1 f) + g^{22}(\partial_2 f)^2. \tag{A.8}$$

To calculate the contraction of the gradient with the curvature tensor, $K^{ij}\nabla_i f \nabla_j f$, we first state the covariant curvature. Due to the symmetry of our metric tensor under transposition, the components of the contravariant curvature can be calculated through a multiple matrix multiplication:

$$K^{ij} = \begin{pmatrix} g^{11} & g^{12} \\ g^{21} & g^{22} \end{pmatrix} \begin{pmatrix} K_{11} & K_{12} \\ K_{21} & K_{22} \end{pmatrix} \begin{pmatrix} g^{11} & g^{12} \\ g^{21} & g^{22} \end{pmatrix}. \tag{A.9}$$

In turn, the desired contraction is

$$K^{ij}\nabla_i f \nabla_j f = \begin{pmatrix} \partial_1 f & \partial_2 f \end{pmatrix} \begin{pmatrix} K^{11} & K^{12} \\ K^{21} & K^{22} \end{pmatrix} \begin{pmatrix} \partial_1 f \\ \partial_2 f \end{pmatrix}. \tag{A.10}$$

To obtain directional derivatives, it is necessary to use information about the derivatives of the vectors defining the local frame on the surface. This information is contained in the Christoffel symbols, $\Gamma^a_{bc} = g^{ad}\mathbf{e}_d \cdot \partial_b \mathbf{e}_c$. We can present the components of the symbols as the entries of two matrices, one for each value of the upper index:

$$\begin{aligned}
\Gamma^1_{bc} &= \begin{pmatrix} (\Gamma^1)_{11} & (\Gamma^1)_{12} \\ (\Gamma^1)_{21} & (\Gamma^1)_{22} \end{pmatrix} && \text{(A.11)} \\
&= \begin{pmatrix} g^{11}\mathbf{e}_1 \cdot \partial_1 \mathbf{e}_1 + g^{12}\mathbf{e}_2 \cdot \partial_1 \mathbf{e}_1 & g^{11}\mathbf{e}_1 \cdot \partial_1 \mathbf{e}_2 + g^{12}\mathbf{e}_2 \cdot \partial_1 \mathbf{e}_2 \\ g^{11}\mathbf{e}_1 \cdot \partial_2 \mathbf{e}_1 + g^{12}\mathbf{e}_2 \cdot \partial_2 \mathbf{e}_1 & g^{11}\mathbf{e}_1 \cdot \partial_2 \mathbf{e}_2 + g^{12}\mathbf{e}_2 \cdot \partial_2 \mathbf{e}_2 \end{pmatrix}, && \text{(A.12)} \\
\Gamma^2_{bc} &= \begin{pmatrix} (\Gamma^2)_{11} & (\Gamma^2)_{12} \\ (\Gamma^2)_{21} & (\Gamma^2)_{22} \end{pmatrix} && \text{(A.13)} \\
&= \begin{pmatrix} g^{21}\mathbf{e}_1 \cdot \partial_1 \mathbf{e}_1 + g^{22}\mathbf{e}_2 \cdot \partial_1 \mathbf{e}_1 & g^{21}\mathbf{e}_1 \cdot \partial_1 \mathbf{e}_2 + g^{22}\mathbf{e}_2 \cdot \partial_1 \mathbf{e}_2 \\ g^{21}\mathbf{e}_1 \cdot \partial_2 \mathbf{e}_1 + g^{22}\mathbf{e}_2 \cdot \partial_2 \mathbf{e}_1 & g^{21}\mathbf{e}_1 \cdot \partial_2 \mathbf{e}_2 + g^{22}\mathbf{e}_2 \cdot \partial_2 \mathbf{e}_2 \end{pmatrix}. && \text{(A.14)}
\end{aligned}$$

The gradient of a vector is then defined as $\nabla_i v_j = \partial_i v_j - \Gamma_{ij}^k v_k$. Using this result, the Laplacian of a scalar, defined as $\nabla^2 f = \nabla^i \nabla_i f = g^{ij} \nabla_i \nabla_j f$, is given by

$$\begin{aligned} \nabla^2 f &= g^{11}\partial_{11} f + 2g^{12}\partial_{12} f + g^{22}\partial_{22} f \\ &\quad -(g^{11}\Gamma_{11}^1 + 2g^{12}\Gamma_{12}^1 + g^{22}\Gamma_{22}^1)\partial_1 f \\ &\quad -(g^{11}\Gamma_{11}^2 + 2g^{12}\Gamma_{12}^2 + g^{22}\Gamma_{22}^2)\partial_2 f, \end{aligned} \tag{A.15}$$

where we have again used the symmetry of the metric tensor.

BIBLIOGRAPHY

BIBLIOGRAPHY

[1] Gennis, R., 1989. Biomembranes Molecular Structure and Function. Springer-Verlag, New York.

[2] Nelson, D., and M. Cox, 2005. Lehninger Principles of Biochemistry. W. H. Freeman and Company, New York, 4th edition.

[3] Singer, S. J., and G. L. Nicolson, 1972. The Fluid Mosaic Model of the Structure of Cell Membranes. *Science* 175:720–731.

[4] Eggeling, C., C. Ringemann, R. Medda, G. Schwarzmann, K. Sandhoff, S. Polyakova, V. N. Belov, B. Hein, C. von Middendorff, A. Schoenle, and S. W. Hell, 2009. Direct observation of the nanoscale dynamics of membrane lipids in a living cell. *Nature* 457:1159–U121.

[5] Veatch, S. L., and S. L. Keller, 2003. Separation of liquid phases in giant vesicles of ternary mixtures of phospholipids and cholesterol. *Biophys. J.* 85:3074–3083.

[6] Veatch, S. L., and S. L. Keller, 2005. Seeing spots: Complex phase behavior in simple membranes. *BBA-Mol. Cell Res.* 1746:172–185.

[7] Bacia, K., P. Schwille, and T. Kurzchalia, 2005. Sterol structure determines the separation of phases and the curvature of the liquid-ordered phase in model membranes. *Proc. Natl. Acad. Sci. USA* 102:3272–3277.

[8] Baumgart, T., S. T. Hess, and W. W. Webb, 2003. Imaging coexisting fluid domains in biomembrane models coupling curvature and line tension. *Nature* 425:821–824.

[9] Pike, L. J., 2006. Rafts defined: a report on the Keystone Symposium on Lipid Rafts and Cell Function. *J. Lipid Res.* 47:1597–1598.

[10] Simons, K., and E. Ikonen, 1997. Functional rafts in cell membranes. *Nature* 387:569–572.

[11] Sengupta, P., B. Baird, and D. Holowka, 2007. Lipid rafts, fluid/fluid phase separation, and their relevance to plasma membrane structure and function. *Semin. Cell Dev. Biol.* 18:583–590.

[12] Ahmed, S. N., D. A. Brown, and E. London, 1997. On the origin of sphingolipid/cholesterol-rich detergent-insoluble cell membranes: Physiological concentrations of cholesterol and sphingolipid induce formation of a detergent-insoluble, liquid-ordered lipid phase in model membranes. *Biochemistry* 36:10944–10953.

[13] Silvius, J. R., D. del Giudice, and M. Lafleur, 1996. Cholesterol at different bilayer concentrations can promote or antagonize lateral segregation of phospholipids of differing acyl chain length. *Biochemistry* 35:15198–15208.

[14] Brown, D. A., and E. London, 2000. Structure and function of sphingolipid- and cholesterol-rich membrane rafts. *J. Biol. Chem.* 275:17221–17224.

[15] Edidin, M., 2003. The state of lipid rafts: From model membranes to cells. *Annu. Rev. Bioph. Biom.* 32:257–283.

[16] van Meer, G., D. R. Voelker, and G. W. Feigenson, 2008. Membrane lipids: where they are and how they behave. *Nat. Rev. Mol. Cell Bio.* 9:112–124.

[17] Brown, D. A., and J. K. Rose, 1992. Sorting of GPI-Anchored Proteins to Glycolipid-Enriched Membrane Subdomains During Transport to the Apical Cell-Surface. *Cell* 68:533–544.

[18] Parton, R. G., and K. Simons, 1995. Digging Into Caveolae. *Science* 269:1398–1399.

[19] Brown, D. A., and E. London, 1998. Structure and origin of ordered lipid domains in biological membranes. *J. Membrane Biol.* 164:103–114.

[20] Martens, J. R., R. Navarro-Polanco, E. A. Coppock, A. Nishiyama, L. Parshley, T. D. Grobaski, and M. M. Tamkun, 2000. Differential targeting of shaker-like potassium channels to lipid rafts. *J. Biol. Chem.* 275:7443–7446.

[21] Sheets, E. D., D. Holowka, and B. Baird, 1999. Critical role for cholesterol in Lyn-mediated tyrosine phosphorylation of FcϵRI and their association with detergent-resistant membranes. *J. Cell Biol.* 145:877–887.

[22] Keller, P., and K. Simons, 1998. Cholesterol is required for surface transport of influenza virus hemagglutinin. *J. Cell Biol.* 140:1357–1367.

[23] Sheets, E. D., G. M. Lee, R. Simson, and K. Jacobson, 1997. Transient confinement of a glycosylphosphatidylinositol-anchored protein in the plasma membrane. *Biochem.* 36:12449–12458.

[24] Schutz, G. J., G. Kada, V. P. Pastushenko, and H. Schindler, 2000. Properties of lipid microdomains in a muscle cell membrane visualized by single molecule microscopy. *EMBO J.* 19:892–901.

[25] Dietrich, C., B. Yang, T. Fujiwara, A. Kusumi, and K. Jacobson, 2002. Relationship of lipid rafts to transient confinement zones detected by single particle tracking. *Biophys. J.* 82:274–284.

[26] Lommerse, P. H. M., G. A. Blab, L. Cognet, G. S. Harms, B. E. Snaar-Jagalska, H. P. Spaink, and T. Schmidt, 2004. Single-molecule imaging of the H-Ras membrane-anchor reveals domains in the cytoplasmic lealet of the cell membrane. *Biophys. J.* 86:609–616.

[27] Lommerse, P. H. M., H. P. Spaink, and T. Schmidt, 2004. In vivo plasma membrane organization: results of biophysical approaches. *BBA-Biomembranes* 1664:119–131.

[28] Pierce, S. K., 2002. Lipid rafts and B-cell activation. *Nat. Rev. Immunol.* 2:96–105.

[29] Holowka, D., J. A. Gosse, A. T. Hammond, X. M. Han, P. Sengupta, N. L. Smith, A. Wagenknecht-Wiesner, M. Wu, R. M. Young, and B. Baird, 2005. Lipid segregation and IgE receptor signaling: A decade of progress. *BBA-Mol. Cell Res.* 1746:252–259.

[30] Kabouridis, P. S., 2006. Lipid rafts in T cell receptor signalling (Review). *Mol. Membr. Biol.* 23:49–57.

[31] Parton, R. G., 2003. Caveolae - from ultrastructure to molecular mechanisms. *Nat. Rev. Mol. Cell Bio.* 4:162–167.

[32] Parton, R. G., M. Hanzal-Bayer, and J. F. Hancock, 2006. Biogenesis of caveolae: a structural model for caveolin-induced domain formation. *J. Cell Sci.* 119:787–796.

[33] Smart, E. J., G. A. Graf, M. A. McNiven, W. C. Sessa, J. A. Engelman, P. E. Scherer, T. Okamoto, and M. P. Lisanti, 1999. Caveolins, liquid-ordered domains, and signal transduction. *Mol. Cell. Biol.* 19:7289–7304.

[34] Green, J. M., A. Zhelesnyak, J. Chung, F. P. Lindberg, M. Sarfati, W. A. Frazier, and E. J. Brown, 1999. Role of cholesterol in formation and function of a signaling complex involving αvβ3, integrin-associated protein (CD47), and heterotrimeric G proteins. *J. Cell Biol.* 146:673–682.

[35] Krauss, K., and P. Altevogt, 1999. Integrin leukocyte function-associated antigen-1-mediated cell binding can be activated by clustering of membrane rafts. *J. Biol. Chem.* 274:36921–36927.

[36] Poveda, J. A., A. M. Fernandez, J. A. Encinar, and J. M. Gonzalez-Ros, 2008. Protein-promoted membrane domains. *BBA-Biomembranes* 1778:1583–1590.

[37] Zhang, W. G., R. P. Trible, and L. E. Samelson, 1998. LAT palmitoylation: Its essential role in membrane microdomain targeting and tyrosine phosphorylation during T cell activation. *Immunity* 9:239–246.

[38] Fivaz, M., L. Abrami, and F. G. van der Goot, 1999. Landing on lipid rafts. *Trends Cell Biol.* 9:212–213.

[39] Epand, R. M., 2008. Proteins and cholesterol-rich domains. *BBA-Biomembranes* 1778:1576–1582.

[40] Chiantia, S., J. Ries, N. Kahya, and P. Schwille, 2006. Combined AFM and two-focus SFCS study of raft-exhibiting model membranes. *ChemPhysChem* 7:2409–2418.

[41] Rozovsky, S., Y. Kaizuka, and J. T. Groves, 2005. Formation and spatio-temporal evolution of periodic structures in lipid bilayers. *J. Am. Chem. Soc.* 127:36–37.

[42] Baumgart, T., A. T. Hammond, P. Sengupta, S. T. Hess, D. A. Holowka, B. A. Baird, and W. W. Webb, 2007. Large-scale fluid/fluid phase separation of proteins and lipids in giant plasma membrane vesicles. *Proc. Natl. Acad. Sci. USA* 104:3165–3170.

[43] Binnig, G., C. F. Quate, and C. Gerber, 1986. Atomic Force Microscope. *Phys. Rev. Lett.* 56:930–933.

[44] Elson, E. L., and D. Magde, 1974. Fluorescence Correlation Spectroscopy. I. Conceptual Basis and Theory. *Biopolymers* 13:1–27.

[45] Magde, D., E. L. Elson, and W. W. Webb, 1974. Fluorescence Correlation Spectroscopy. II. Experimental Realization. *Biopolymers* 13:29–61.

[46] Johnston, L. J., 2007. Nanoscale imaging of domains in supported lipid membranes. *Langmuir* 23:5886–5895.

[47] Rinia, H. A., M. M. E. Snel, J. P. J. M. van der Eerden, and B. de Kruijff, 2001. Visualizing detergent resistant domains in model membranes with atomic force microscopy. *FEBS Lett.* 501:92–96.

[48] Korlach, J., P. Schwille, W. W. Webb, and G. W. Feigenson, 1999. Characterization of lipid bilayer phases by confocal microscopy and fluorescence correlation spectroscopy. *Proc. Natl. Acad. Sci. USA* 96:8461–8466.

[49] Bacia, K., D. Scherfeld, N. Kahya, and P. Schwille, 2004. Fluorescence correlation spectroscopy relates rafts in model and native membranes. *Biophys. J.* 87:1034–1043.

[50] Korlach, J., T. Baumgart, W. W. Webb, and G. W. Feigenson, 2005. Detection of motional heterogeneities in lipid bilayer membranes by dual probe fluorescence correlation spectroscopy. *BBA-Biomembranes* 1668:158–163.

[51] Kahya, N., D. Scherfeld, K. Bacia, and P. Schwille, 2004. Lipid domain formation and dynamics in giant unilamellar vesicles explored by fluorescence correlation spectroscopy. *J. Struct. Biol.* 147:77–89.

[52] Garcia-Saez, A. J., S. Chiantia, and P. Schwille, 2007. Effect of line tension on the lateral organization of lipid membranes. *J. Biol. Chem.* 282.

[53] Jacobson, K., O. G. Mouritsen, and R. G. W. Anderson, 2007. Lipid rafts: at a crossroad between cell biology and physics. *Nat. Cell Biol.* 9:7–14.

[54] Lillemeier, B. F., J. R. Pfeiffer, Z. Surviladze, B. S. Wilson, and M. M. Davis, 2006. Plasma membrane-associated proteins are clustered into islands attached to the cytoskeleton. *Proc. Natl. Acad. Sci. USA* 103:18992–18997.

[55] Lenne, P.-F., L. Wawrezinieck, F. Conchonaud, O. Wurtz, A. Boned, X.-J. Guo, H. Rigneault, H.-T. He, and D. Marguet, 2006. Dynamic molecular confinement in the plasma membrane by microdomains and the cytoskeleton meshwork. *EMBO J.* 25:3245–3256.

[56] Karve, S., G. B. Kempegowda, and S. Sofou, 2008. Heterogeneous domains and membrane permeability in phosphatidylcholine - Phosphatidic acid rigid vesicles as a function of pH and lipid chain mismatch. *Langmuir* 24:5679–5688.

[57] Hillery, A. M., 1997. Supramolecular lipidic drug delivery systems: from laboratory to clinic a review of the recently introduced commercial liposomal and lipid-based formulations of amphotericin B. *Adv. Drug Deliver. Rev.* 24:345–363.

[58] Cevc, G., 2004. Lipid vesicles and other colloids as drug carriers on the skin. *Adv. Drug Deliver. Rev.* 56:675–711.

[59] de Planque, M. R. R., G. P. Mendes, M. Zagnoni, M. E. Sandison, K. H. Fisher, R. M. Berry, A. Watts, and H. Morgan, 2006. Controlled delivery of membrane proteins to artificial lipid bilayers by nystatin-ergosterol modulated vesicle fusion. *IEE P-Nanobiotechnol* 153:21–30.

[60] Dimova, R., K. A. Riske, S. Aranda, N. Bezlyepkina, R. L. Knorr, and R. Lipowsky, 2007. Giant vesicles in electric fields. *Soft Matter* 3:817–827.

[61] Karlsson, M., K. Sott, A. S. Cans, A. Karlsson, R. Karlsson, and O. Orwar, 2001. Micropipet-assisted formation of microscopic networks of unilamellar lipid bilayer nanotubes and containers. *Langmuir* 17:6754–6758.

[62] Loew, M., R. Springer, S. Scolari, F. Altenbrunn, O. Seitz, J. Liebscher, D. Huster, A. Herrmann, and A. Arbuzova, 2010. Lipid domain specific recruitment of lipophilic nucleic acids: A key for switchable functionalization of membranes. *J. Am. Chem. Soc.* 132:16066–16072.

[63] Mukherjee, S., and F. R. Maxfield, 2004. Membrane domains. *Annu. Rev. Cell Dev. Bi.* 20:839–866.

[64] Haque, M. E., and B. R. Lentz, 2004. Roles of curvature and hydrophobic interstice energy in fusion: Studies of lipid perturbant effects. *Biochemistry* 43:3507–3517.

[65] Wan, C., V. Kiessling, and L. K. Tamm, 2008. Coupling of cholesterol-rich lipid phases in asymmetric bilayers. *Biochemistry* 47:2190–2198.

[66] Kiessling, V., C. Wan, and L. K. Tamm, 2009. Domain coupling in asymmetric lipid bilayers. *BBA-Biomembranes* 1788:64–71.

[67] Murphy, D. J., 1982. The Importance Of Non-Planar Bilayer Regions In Photosynthetic Membranes And Their Stabilization By Galactolipids. *FEBS Lett.* 150:19–26.

[68] Murphy, D. J., and I. E. Woodrow, 1983. The Lateral Segregation Model. A New Paradigm for the Dynamic Role of Acyl Lipids in the Molecular Organization of Photosynthetic Membranes. *In* W. Thomson, J. Mudd, and M. Gibbs, editors, Biosynthesis and Function of Plant Lipids. Waverly Press, Maryland, Proceedings of the Sixth Annual Symposim in Botany, 104–125.

[69] Lipowsky, R., 1992. Budding of membranes induced by intramembrane domains. *J. Phys. II* 2:1825–1840.

[70] Sorre, B., A. Callan-Jones, J.-B. Manneville, P. Nassoy, J.-F. Joanny, J. Prost, B. Goud, and P. Bassereau, 2009. Curvature-driven lipid sorting needs proximity to a demixing point and is aided by proteins. *Proc. Natl. Acad. Sci. USA* 106:5622–5626.

[71] Parthasarathy, R., C.-H. Yu, and J. T. Groves, 2006. Curvature-modulated phase separation in lipid bilayer membranes. *Langmuir* 22:5095–5099.

[72] Gerlach, H., V. Laumann, S. Martens, C. F. W. Becker, R. S. Goody, and M. Geyer, 2010. HIV-1 Nef membrane association depends on charge, curvature, composition and sequence. *Nat. Chem. Biol.* 6:46–53.

[73] Mouritsen, O. G., and M. Bloom, 1984. Mattress Model of Lipid-Protein Interactions in Membranes. *Biophys. J.* 46:141–153.

[74] Killian, J. A., 1998. Hydrophobic mismatch between proteins and lipids in membranes. *BBA-Rev. Biomembranes* 1376:401–416.

[75] Wenk, M. R., and P. De Camilli, 2004. Protein-lipid interactions and phosphoinositide metabolism in membrane traffic: Insights from vesicle recycling in nerve terminals. *Proc. Natl. Acad. Sci. USA* 101:8262–8269.

[76] Ford, M. G. J., I. G. Mills, B. J. Peter, Y. Vallis, G. J. K. Praefcke, P. R. Evans, and H. T. McMahon, 2002. Curvature of clathrin-coated pits driven by epsin. *Nature* 419:361–366.

[77] Bhatia, V. K., K. L. Madsen, P.-Y. Bolinger, A. Kunding, P. Hedegard, U. Gether, and D. Stamou, 2009. Amphipathic motifs in BAR domains are essential for membrane curvature sensing. *EMBO J.* 28:3303–3314.

[78] Peter, B. J., H. M. Kent, I. G. Mills, Y. Vallis, P. J. G. Butler, P. R. Evans, and H. T. McMahon, 2004. BAR domains as sensors of membrane curvature: The amphiphysin BAR structure. *Science* 303:495–499.

[79] Drin, G., and B. Antonny, 2010. Amphipathic helices and membrane curvature. *FEBS Lett.* 584:1840–1847.

[80] Hatzakis, N. S., V. K. Bhatia, J. Larsen, K. L. Madsen, P.-Y. Bolinger, A. H. Kunding, J. Castillo, U. Gether, P. Hedegard, and D. Stamou, 2009. How curved membranes recruit amphipathic helices and protein anchoring motifs. *Nat. Chem. Biol.* 5:835–841.

[81] Lemmon, M. A., 2008. Membrane recognition by phospholipid-binding domains. *Nat. Rev. Mol. Cell Bio.* 9:99–111.

[82] McMahon, H. T., and J. L. Gallop, 2005. Membrane curvature and mechanisms of dynamic cell membrane remodelling. *Nature* 438:590–596.

[83] Bhatia, V. K., N. S. Hatzakis, and D. Stamou, 2010. A unifying mechanism accounts for sensing of membrane curvature by BAR domains, amphipathic helices and membrane-anchored proteins. *Semin. Cell Dev. Biol.* 21:381–390.

[84] Putzel, G. G., and M. Schick, 2008. Phase behavior of a model bilayer membrane with coupled leaves. *Biophys. J.* 94:869–877.

[85] Allender, D. W., and M. Schick, 2006. Phase separation in bilayer lipid membranes: Effects on the inner leaf due to coupling to the outer leaf. *Biophys. J.* 91:2928–2935.

[86] Wagner, A. J., S. Loew, and S. May, 2007. Influence of monolayer-monolayer coupling on the phase behavior of a fluid lipid bilayer. *Biophys. J.* 93:4268–4277.

[87] Collins, M. D., and S. L. Keller, 2008. Tuning lipid mixtures to induce or suppress domain formation across leaflets of unsupported asymmetric bilayers. *Proc. Natl. Acad. Sci. USA* 105:124–128.

[88] Garg, S., J. Ruehe, K. Luedtke, R. Jordan, and C. A. Naumann, 2007. Domain registration in raft-mimicking lipid mixtures studied using polymer-tethered lipid bilayers. *Biophys. J.* 92:1263–1270.

[89] Rodgers, W., B. Crise, and J. K. Rose, 1994. Signals Determining Protein-Tyrosine Kinase And Glycosyl-Phosphatidylinositol-Anchored Protein Targeting To A Glycolipid-Enriched Membrane-Fraction. *Mol. Cell. Biol.* 14:5384–5391.

[90] Baird, B., E. D. Sheets, and D. Holowka, 1999. How does the plasma membrane participate in cellular signaling by receptors for immunoglobulin E? *Biophys. Chem.* 82:109–119.

[91] van Meer, G., 2002. Cell biology - The different hues of lipid rafts. *Science* 296:855–857.

[92] Subczynski, W. K., and A. Kusumi, 2003. Dynamics of raft molecules in the cell and artificial membranes: approaches by pulse EPR spin labeling and single molecule optical microscopy. *BBA-Biomembranes* 1610:231–243.

[93] Kusumi, A., I. Koyama-Honda, and K. Suzuki, 2004. Molecular dynamics and interactions for creation of stimulation-induced stabilized rafts from small unstable steady-state rafts. *Traffic* 5:213–230.

[94] Quinn, P. J., and C. Wolf, 2009. Hydrocarbon chains dominate coupling and phase coexistence in bilayers of natural phosphatidylcholines and sphingomyelins. *BBA-Biomembranes* 1788:1126–1137.

[95] Collins, M. D., 2008. Interleaflet coupling mechanisms in bilayers of lipids and cholesterol. *Biophys. J.* 94:L32–L34.

[96] May, S., 2009. Trans-monolayer coupling of fluid domains in lipid bilayers. *Soft Matter* 5:3148–3156.

[97] Marrink, S. J., A. H. de Vries, and D. P. Tieleman, 2009. Lipids on the move: Simulations of membrane pores, domains, stalks and curves. *BBA-Biomembranes* 1788:149–168.

[98] Brooks, B., R. Bruccoleri, D. Olafson, D. States, S. Swaminathan, and M. Karplus, 1983. CHARMM: A Program for Macromolecular Energy, Minimization, and Dynamics Calculations. *J. Comput. Chem.* 4:187–217.

[99] MacKerel Jr., A. D., C. L. Brooks III, L. Nilsson, B. Roux, Y. Won, and M. Karplus, 1998. CHARMM: The Energy Function and Its Parameterization with an Overview of the Program, volume 1 of *The Encyclopedia of Computational Chemistry.* John Wiley & Sons: Chichester.

[100] Berendsen, H. J. C., D. Vanderspoel, and R. Vandrunen, 1995. GROMACS - A Message-Passing Parallel Molecular-Dynamics Implementation. *Comput. Phys. Commun.* 91:43–56.

[101] Lindahl, E., B. Hess, and D. van der Spoel, 2001. GROMACS 3.0: a package for molecular simulation and trajectory analysis. *J. Mol. Model.* 7:306–317.

[102] Phillips, J. C., R. Braun, W. Wang, J. Gumbart, E. Tajkhorshid, E. Villa, C. Chipot, R. D. Skeel, L. Kalé, and K. Schulten, 2005. Scalable molecular dynamics with NAMD. *J. Comput. Chem.* 26:1781–1802.

[103] Plimpton, S., 1995. Fast Parallel Algorithms for Short-Range Molecular Dynamics. *J. Comp. Phys.* 117:1–19.

[104] Muller, M., K. Katsov, and M. Schick, 2006. Biological and synthetic membranes: What can be learned from a coarse-grained description? *Phys. Rep.* 434:113–176.

[105] Devireddy, R. V., 2010. Statistical thermodynamics of biomembranes. *Cryobiology* 60:80–90.

[106] Chiu, S. W., S. Vasudevan, E. Jakobsson, R. J. Mashl, and H. L. Scott, 2003. Structure of sphingomyelin bilayers: A simulation study. *Biophys. J.* 85:3624–3635.

[107] Rog, T., and M. Pasenkiewicz-Gierula, 2006. Cholesterol-sphingomyelin interactions: A molecular dynamics simulation study. *Biophys. J.* 91:3756–3767.

[108] Rog, T., K. Murzyn, R. Gurbiel, Y. Takaoka, A. Kusumi, and M. Pasenkiewicz-Gierula, 2004. Effects of phospholipid unsaturation on the bilayer nonpolar region: a molecular simulation study. *J. Lipid Res.* 45:326–336.

[109] Niemela, P., M. T. Hyvonen, and I. Vattulainen, 2004. Structure and dynamics of sphingomyelin bilayer: Insight gained through systematic comparison to phosphatidylcholine. *Biophys. J.* 87:2976–2989.

[110] Zhang, Z., L. Lu, and M. L. Berkowitz, 2008. Energetics of cholesterol transfer between lipid bilayers. *J. Phys. Chem. B* 112:3807–3811.

[111] Zhang, Z., S. Y. Bhide, and M. L. Berkowitz, 2007. Molecular dynamics simulations of bilayers containing mixtures of sphingomyelin with cholesterol and phosphatidylcholine with cholesterol. *J. Phys. Chem. B* 111:12888–12897.

[112] Tu, K. C., M. L. Klein, and D. J. Tobias, 1998. Constant-pressure molecular dynamics investigation of cholesterol effects in a dipalmitoylphosphatidylcholine bilayer. *Biophys. J.* 75:2147–2156.

[113] Hofsass, C., E. Lindahl, and O. Edholm, 2003. Molecular dynamics simulations of phospholipid bilayers with cholesterol. *Biophys. J.* 84:2192–2206.

[114] Pandit, S. A., E. Jakobsson, and H. L. Scott, 2004. Simulation of the early stages of nano-domain formation in mixed bilayers of sphingomyelin, cholesterol, and dioleylphosphatidylcholine. *Biophys. J.* 87:3312–3322.

[115] Niemela, P. S., S. Ollila, M. T. Hyvonen, M. Karttunen, and I. Vattulainen, 2007. Assessing the nature of lipid raft membranes. *PLoS Comput. Biol.* 3:304–312.

[116] Venturoli, M., M. M. Sperotto, M. Kranenburg, and B. Smit, 2006. Mesoscopic models of biological membranes. *Phys. Rep.* 437:1–54.

[117] Pandit, S. A., and H. L. Scott, 2009. Multiscale simulations of heterogeneous model membranes. *BBA-Biomembranes* 1788:136–148.

[118] Orsi, M., D. Y. Haubertin, W. E. Sanderson, and J. W. Essex, 2008. A quantitative coarse-grain model for lipid bilayers. *J. Phys. Chem. B* 112:802–815.

[119] den Otter, W. K., and W. J. Briels, 2003. The bending rigidity of an amphiphilic bilayer from equilibrium and nonequilibrium molecular dynamics. *J. Chem. Phys.* 118:4712–4720.

[120] Imparato, A., J. C. Shillcock, and R. Lipowsky, 2005. Shape fluctuations and elastic properties of two-component bilayer membranes. *Europhys. Lett.* 69:650–656.

[121] Faller, R., and S. J. Marrink, 2004. Simulation of domain formation in DLPC-DSPC mixed bilayers. *Langmuir* 20:7686–7693.

[122] Goetz, R., and R. Lipowsky, 1998. Computer simulations of bilayer membranes: Self-assembly and interfacial tension. *J. Chem. Phys.* 108:7397–7409.

[123] Izvekov, S., and G. A. Voth, 2006. Multiscale coarse-graining of mixed phospholipid/cholesterol bilayers. *J. Chem. Theory Comput.* 2:637–648.

[124] Stevens, M. J., 2005. Complementary matching in domain formation within lipid bilayers. *J. Am. Chem. Soc.* 127:15330–15331.

[125] Zheng, C., P. Liu, J. Li, and Y.-W. Zhang, 2010. Phase Diagrams for Multi-Component Membrane Vesicles: A Coarse-Grained Modeling Study. *Langmuir* 26:12659–12666.

[126] Shillcock, J. C., and R. Lipowsky, 2002. Equilibrium structure and lateral stress distribution of amphiphilic bilayers from dissipative particle dynamics simulations. *J. Chem. Phys.* 117:5048–5061.

[127] Yang, K., X. Shao, and Y.-Q. Ma, 2009. Shape deformation and fission route of the lipid domain in a multicomponent vesicle. *Phys. Rev. E* 79:051924.

[128] Laradji, M., and P. B. S. Kumar, 2006. Anomalously slow domain growth in fluid membranes with asymmetric transbilayer lipid distribution. *Phys. Rev. E* 73:040901.

[129] Brannigan, G., P. F. Philips, and F. L. H. Brown, 2005. Flexible lipid bilayers in implicit solvent. *Phys. Rev. E* 72:011915.

[130] Brannigan, G., and F. L. H. Brown, 2004. Solvent-free simulations of fluid membrane bilayers. *J. Chem. Phys.* 120:1059–1071.

[131] Lipowsky, R., 2002. Domains and rafts in membranes - Hidden dimensions of selforganization. *J. Biol. Phys.* 28:195–210.

[132] Murtola, T., E. Falck, M. Karttunen, and I. Vattulainen, 2007. Coarse-grained model for phospholipid/cholesterol bilayer employing inverse Monte Carlo with thermodynamic constraints. *J. Chem. Phys.* 126:075101.

[133] Kumar, P. B. S., and M. Rao, 1998. Shape instabilities in the dynamics of a two-component fluid membrane. *Phys. Rev. Lett.* 80:2489–2492.

[134] Collins, S., M. Stamatakis, and D. G. Vlachos, 2010. Adaptive coarse-grained Monte Carlo simulation of reaction and diffusion dynamics in heterogeneous plasma membranes. *BMC Bioinformatics* 11:218.

[135] Wallace, E. J., N. M. Hooper, and P. D. Olmsted, 2005. The kinetics of phase separation in asymmetric membranes. *Biophys. J.* 88:4072–4083.

[136] Sohn, J. S., Y.-H. Tseng, S. Li, A. Voigt, and J. S. Lowengrub, 2010. Dynamics of multicomponent vesicles in a viscous fluid. *J. Comput. Phys.* 229:119–144.

[137] Ayton, G. S., J. L. McWhirter, P. McMurtry, and G. A. Voth, 2005. Coupling field theory with continuum mechanics: A simulation of domain formation in giant unilamellar vesicles. *Biophys. J.* 88:3855–3869.

[138] Wang, X., and Q. Du, 2008. Modelling and simulations of multi-component lipid membranes and open membranes via diffuse interface approaches. *J. Math. Biol.* 56:347–371.

[139] Sample, C., and A. A. Golovin, 2007. Nonlinear dynamics of a double bilipid membrane. *Phys. Rev. E* 76:031925.

[140] Khelashvili, G., D. Harries, and H. Weinstein, 2009. Modeling Membrane Deformations and Lipid Demixing upon Protein-Membrane Interaction: The BAR Dimer Adsorption. *Biophys. J.* 97:1626–1635.

[141] Du, Q., C. Liu, and X. Q. Wang, 2004. A phase field approach in the numerical study of the elastic bending energy for vesicle membranes. *J. Comput. Phys.* 198:450–468.

[142] Du, Q., C. Liu, and X. Q. Wang, 2005. Simulating the deformation of vesicle membranes under elastic bending energy in three dimensions. *J. Comput.Phys.* 212:757–777.

[143] Taniguchi, T., 1996. Shape deformation and phase separation dynamics of two-component vesicles. *Phys. Rev. Lett.* 76:4444–4447.

[144] Fan, J., M. Sammalkorpi, and M. Haataja, 2008. Domain formation in the plasma membrane: Roles of nonequilibrium lipid transport and membrane proteins. *Phys. Rev. Lett.* 100:178102.

[145] Fan, J., M. Sammalkorpi, and M. Haataja, 2010. Influence of nonequilibrium lipid transport, membrane compartmentalization, and membrane proteins on the lateral organization of the plasma membrane. *Phys. Rev. E* 81:011908.

[146] Ayton, G. S., S. Izvekov, W. G. Noid, and G. A. Voth, 2008. Multiscale simulation of membranes and membrane proteins: Connecting molecular interactions to mesoscopic behavior. *In* Computational Modeling of Membrane Bilayers, Academic Press, volume 60 of *Curr. Top. Membr.*, 181–225.

[147] Emmerich, H., 2003. The Diffuse Interface Approach in Materials Science. Springer, Berlin.

[148] Provatas, N., and K. Elder, 2010. Phase-Field Methods in Materials Science and Engineering. Wiley-VCH.

[149] Ginzberg, V. L., and L. D. Landau, 1950. To the Theory of Superconductivity. *Zh. Eksp. Teor. Fiz.* 20:1064.

[150] Cahn, J. W., and J. E. Hilliard, 1958. Free Energy of a Nonuniform System. I. Interfacial Free Energy. *J. Chem. Phys.* 28:258–267.

[151] Cahn, J. W., 1961. On Spinodal Decomposition. *Acta Metall. Mater.* 9:795–801.

[152] Allen, S. M., and J. W. Cahn, 1979. Microscopic Theory For Antiphase Boundary Motion And Its Application To Antiphase Domain Coarsening. *Acta Metall. Mater.* 27:1085–1095.

[153] Cahn, J. W., 1979. Interfacial Segregation. ASM, Metals Park, OH, 3–23.

[154] Karma, A., 2001. Phase-field formulation for quantitative modeling of alloy solidification. *Phys. Rev. Lett.* 87:115701.

[155] Seol, D. J., S. Y. Hu, Y. L. Li, J. Shen, K. H. Oh, and L. Q. Chen, 2003. Computer simulation of spinodal decomposition in constrained fims. *Acta Mater.* 51:5173–5185.

[156] Lewis, D., T. Pusztai, L. Granasy, J. Warren, and W. Boettinger, 2004. Phase-field models for eutectic solidification. *J. Mater.* 56:34–39.

[157] Kim, S. G., W. T. Kim, T. Suzuki, and M. Ode, 2004. Phase-field modeling of eutectic solidification. *J. Cryst. Growth* 261:135–158.

[158] Warren, J. A., R. Kobayashi, A. E. Lobovsky, and W. C. Carter, 2003. Extending phase field models of solidification to polycrystalline materials. *Acta Mater.* 51:6035–6058.

[159] Suwa, Y., Y. Saito, and H. Onodera, 2007. Three-dimensional phase field simulation of the effect of anisotropy in grain-boundary mobility on growth kinetics and morphology of grain structure. *Comp. Mater. Sci.* 40:40–50.

[160] Fan, D. N., S. P. Chen, L. Q. Chen, and P. W. Voorhees, 2002. Phase-field simulation of 2-D Ostwald ripening in the high volume fraction regime. *Acta Mater.* 50:1895–1907.

[161] Cha, P. R., D. H. Yeon, and S. H. Chung, 2005. Phase-field study for the splitting mechanism of coherent misfitting precipitates in anisotropic elastic media. *Scripta Mater.* 52:1241–1245.

[162] Zhu, J. Z., T. Wang, A. J. Ardell, S. H. Zhou, Z. K. Liu, and L. Q. Chen, 2004. Three-dimensional phase-field simulations of coarsening kinetics of gamma' particles in binary Ni-Al alloys. *Acta Mater.* 52:2837–2845.

[163] Choudhury, S., Y. L. Li, C. E. Krill, and L. Q. Chen, 2005. Phase-field simulation of polarization switching and domain evolution in ferroelectric polycrystals. *Acta Mater.* 53:5313–5321.

[164] Wu, K., J. E. Morral, and Y. Wang, 2001. A phase field study of microstructural changes due to the Kirkendall effect in two-phase diffusion couples. *Acta Mater.* 49:3401–3408.

[165] Lu, W., and Z. Suo, 2001. Dynamics of nanoscale pattern formation of an epitaxial monolayer. *J. Mech. Phys. Solids* 49:1937–1950.

[166] Wang, Y. U., Y. M. Jin, A. M. Cuitino, and A. G. Khachaturyan, 2001. Nanoscale phase field microelasticity theory of dislocations: Model and 3D simulations. *Acta Mater.* 49:1847–1857.

[167] Karma, A., D. A. Kessler, and H. Levine, 2001. Phase-field model of mode III dynamic fracture. *Phys. Rev. Lett.* 87:045501.

[168] Chen, L. Q., 2002. Phase-field models for microstructure evolution. *Annu. Rev. Mater. Res.* 32:113–140.

[169] Koyama, T., 2008. Phase-field modeling of microstructure evolutions in magnetic materials. *Sci. Technol. Adv. Mat.* 9:013006.

[170] Stottrup, B. L., S. L. Veatch, and S. L. Keller, 2004. Nonequilibrium behavior in supported lipid membranes containing cholesterol. *Biophys. J.* 86:2942–2950.

[171] Diaz, A. J., F. Albertorio, S. Daniel, and P. S. Cremer, 2008. Double cushions preserve transmembrane protein mobility in supported bilayer systems. *Langmuir* 24:6820–6826.

[172] Merzlyakov, M., E. Li, I. Gitsov, and K. Hristova, 2006. Surface-supported bilayers with transmembrane proteins: Role of the polymer cushion revisited. *Langmuir* 22:10145–10151.

[173] Leidy, C., T. Kaasgaard, J. H. Crowe, O. G. Mouritsen, and K. Jorgensen, 2002. Ripples and the formation of anisotropic lipid domains: Imaging two-component double bilayers by atomic force microscopy. *Biophys. J.* 83:2625–2633.

[174] Montal, M., and P. Mueller, 1972. Formation of bimolecular membranes from lipid monolayers and a study of their electrical properties. *Proc. Natl. Acad. Sci. USA* 69:3561–3566.

[175] Mirzabekov, T. A., A. Y. Silberstein, and B. L. Kagan, 1999. Use of Planar Lipid Bilayer Membranes for Rapid Screening of Membrane Active Compounds. *Method. Enzymol.* 294:661–674.

[176] Majd, S., E. C. Yusko, A. D. MacBriar, J. Yang, and M. Mayer, 2009. Gramicidin Pores Report the Activity of Membrane-Active Enzymes. *J. Am. Chem. Soc.* 131:16119–16126.

[177] Funkhouser, C. M., F. J. Solis, and K. Thornton, 2007. Coupled composition-deformation phase-field method for multicomponent lipid membranes. *Phys. Rev. E* 76:011912.

[178] Helfrich, W., 1973. Elastic properties of lipid bilayers - theory and possible experiments. *Z. Naturforsch. C* 28:693–703.

[179] Goždž, W. T., and G. Gompper, 2001. Shape transformations of two-component membranes under weak tension. *Europhys. Lett.* 55:587–593.

[180] Harden, J. L., F. C. MacKintosh, and P. D. Olmsted, 2005. Budding and domain shape transformations in mixed lipid films and bilayer membranes. *Phys. Rev. E* 72:011903.

[181] Capovilla, R., J. Guven, and J. A. Santiago, 2003. Deformations of the geometry of lipid vesicles. *J. Phys. A-Math. Gen.* 36:6281–6295.

[182] Wang, S. L., R. F. Sekerka, A. A. Wheeler, B. T. Murray, S. R. Coriell, R. J. Braun, and G. B. McFadden, 1993. Thermodynamically-consistent phase-field models for solidification. *Physica D* 69:189–200.

[183] Johnson, W. C., 2001. Spinodal decomposition in a small radially stressed sphere. *Acta Mater.* 49:3463–3474.

[184] McFadden, G. B., and A. A. Wheeler, 2002. On the Gibbs adsorption equation and diffuse interface models. *Proc. R. Soc. London, Ser. A* 458:1129–1149.

[185] Slutsker, J., K. Thornton, A. L. Roytburd, J. A. Warren, and G. B. McFadden, 2006. Phase field modeling of solidification under stress. *Phys. Rev. B* 74:014103.

[186] Boettinger, W. J., J. A. Warren, C. Beckermann, and A. Karma, 2002. Phase-field simulation of solidification. *Annu. Rev. Mater. Res.* 32:163–194.

[187] Thornton, K., J. Ågren, and P. W. Voorhees, 2003. Modelling the evolution of phase boundaries in solids at the meso- and nano-scales. *Acta Mater.* 51:5675–5710.

[188] Cai, W., and T. C. Lubensky, 1994. Covariant Hydrodynamics of Fluid Membranes. *Phys. Rev. Lett.* 73:1186–1189.

[189] Solis, F. J., C. M. Funkhouser, and K. Thornton, 2008. Conditions for overall planarity in membranes: Applications to multicomponent membranes with lamellar morphology. *Europhys. Lett.* 82:38001.

[190] Yoon, T. Y., C. Jeong, S. W. Lee, J. H. Kim, M. C. Choi, S. J. Kim, M. W. Kim, and S. D. Lee, 2006. Topographic control of lipid-raft reconstitution in model membranes. *Nat. Mater.* 5:281–285.

[191] Veatch, S. L., P. Cicuta, P. Sengupta, A. Honerkamp-Smith, D. Holowka, and B. Baird, 2008. Critical fluctuations in plasma membrane vesicles. *ACS Chem. Biol.* 3:287–293.

[192] Funkhouser, C. M., F. J. Solis, and K. Thornton, 2010. Dynamics of two-phase lipid vesicles: effects of mechanical properties on morphology evolution. *Soft Matter* 6:3462–3466.

[193] Kageyama, A., and T. Sato, 2004. "Yin-Yang grid": An overset grid in spherical geometry. *Geochem. Geophy. Geosy.* 5:Q09005.

[194] Shen, S., E. Kendall, A. Oliver, V. Ngassam, D. Hu, and A. N. Parikh, 2011. Liposil-supported lipid bilayers as a hybrid platform for drug delivery. *Soft Matter* 7:1001–1005.

[195] Kaur, C. D., M. Nahar, and N. K. Jain, 2008. Lymphatic targeting of zidovudine using surface-engineered liposomes. *J. Drug Target.* 16:798–805.

[196] Rustom, A., R. Saffrich, I. Markovic, P. Walther, and H. H. Gerdes, 2004. Nanotubular highways for intercellular organelle transport. *Science* 303:1007–1010.

[197] Simpson, J. C., T. Nilsson, and R. Pepperkok, 2006. Biogenesis of tubular ER-to-Golgi transport intermediates. *Mol. Biol. Cell* 17:723–737.

[198] Hu, J., Y. Shibata, C. Voss, T. Shemesh, Z. Li, M. Coughlin, M. M. Kozlov, T. A. Rapoport, and W. A. Prinz, 2008. Membrane proteins of the endoplasmic reticulum induce high-curvature tubules. *Science* 319:1247–1250.

[199] Tian, A., B. R. Capraro, C. Esposito, and T. Baumgart, 2009. Bending Stiffness Depends on Curvature of Ternary Lipid Mixture Tubular Membranes. *Biophys. J.* 97:1636–1646.

[200] Yuan, J., S. M. Hira, G. F. Strouse, and L. S. Hirst, 2008. Lipid bilayer discs and banded tubules: Photoinduced lipid sorting in ternary mixtures. *J. Am. Chem. Soc.* 130:2067–2072.

[201] Lin, Y.-C., K.-S. Huang, J.-T. Chiang, C.-H. Yang, and T.-H. Lai, 2006. Manipulating self-assembled phospholipid microtubes using microfluidic technology. *Sensor. Actuat. B-Chem.* 117:464–471.

[202] Li, L., X. Y. Liang, M. Y. Lin, F. Qiu, and Y. L. Yang, 2005. Budding dynamics of multicomponent tubular vesicles. *J. Am. Chem. Soc.* 127:17996–17997.

[203] Yanagisawa, M., M. Imai, and T. Taniguchi, 2008. Shape deformation of ternary vesicles coupled with phase separation. *Phys. Rev. Lett.* 100:148102.

[204] Yu, Y., and S. Granick, 2009. Pearling of Lipid Vesicles Induced by Nanoparticles. *J. Am. Chem. Soc.* 131:14158–14159.

[205] Tian, A., and T. Baumgart, 2009. Sorting of Lipids and Proteins in Membrane Curvature Gradients. *Biophys. J.* 96:2676–2688.

[206] Plateau, J., 1873. Statique Expérimentale et Théorique des Liquides Soumis aux Seules Forces Moléculaires. Gauthier Villars, Paris.

[207] Rayleigh, L., 1899. Scientific Papers, volume 1. Cambridge: At the University Press.

[208] Angelova, M. I., S. Soleau, P. Meleard, J. F. Faucon, and P. Bothorel, 1992. Preparation of Giant Vesicles by External AC Electric-Fields - Kinetics and Applications. *In* Helm, C and Losche, M and Mohwald, H, editor, Trends in Colloid and Interface Science VI. volume 89 of *Progress in Colloid and Polymer Science*, 127–131.

[209] Zhang, J. B., B. W. Jing, and S. L. Regen, 2005. Transbilayer complementarity of phospholipids. Proof of principle. *Langmuir* 21:8983–8986.

[210] Veatch, S. L., K. Gawrisch, and S. L. Keller, 2006. Closed-loop miscibility gap and quantitative tie-lines in ternary membranes containing diphytanoyl PC. *Biophys. J.* 90:4428–4436.

[211] Wilkins, M. H. F., A. E. Blaurock, and D. M. Engelman, 1971. Bilayer structure in membranes. *Nature-New Biol.* 230:72–76.

[212] Tristram-Nagle, S., and J. F. Nagle, 2004. Lipid bilayers: thermodynamics, structure, fluctuations, and interactions. *Chem. Phys. Lipids* 127:3–14.

[213] Zimmerberg, J., and M. M. Kozlov, 2006. How proteins produce cellular membrane curvature. *Nat. Rev. Mol. Cell Biol.* 7:9–19.

[214] Kooijman, E. E., V. Chupin, N. L. Fuller, M. M. Kozlov, B. de Kruijff, K. N. J. Burger, and P. R. Rand, 2005. Spontaneous curvature of phosphatidic acid and lysophosphatidic acid. *Biochem.* 44:2097–2102.

[215] Fuller, N., and R. P. Rand, 2001. The influence of lysolipids on the spontaneous curvature and bending elasticity of phospholipid membranes. *Biophys. J.* 81:243–254.